Search For Clustering Of Strange Quarks In Relativistic Heavy Ion Collisions At The LHC

by
Surya Prakash Pathak

A dissertation submitted to the Department of Physics,

College of Natural Sciences and Mathematics

in partial fulfillment of the requirements for the degree of

Doctor of Philosophy
in Physics

Chair of Committee: Rene Bellwied

Committee Member: Lawrence Pinsky

Committee Member: Claudia Ratti

Committee Member: John Harris Miller

Committee Member: Paul Mann

University of Houston
May 2021

DEDICATION/EPIGRAPH

To my mother, Bimala

ACKNOWLEDGMENTS

First and foremost, I would like to thank my mother for always providing me the unwavering support. I am grateful for her presence in my life and her constant encouragement to pursue my goals. I dedicate this thesis to her. Secondly, my life partner, Liza, whose support and trust towards me helped me gain some confidence in my work.

Looking back to my journey as a Ph.D. student, I feel that to contribute some time of your life searching for the unknown and this being your day-to-day work is the most privileged thing one could get. There were some challenges, both in terms of work and personal life. I am incredibly grateful to my advisor, Dr. Rene Bellwied, who gave me the opportunity to do this Ph.D. He has also been a great support and a mentor throughout. His valuable advice helped me grow as a researcher as well as a person. I am forever grateful to him. I would also like to thank my thesis committee members Dr. John Miller, Dr. Claudia Ratti, Dr. Lawrence Pinsky, Dr. Paul Mann for their helpful comments and encouragement throughout this journey. To Naomi Haynes, also for her supporting and encouraging words.

I would also like to thank the members of the High Energy Physics group of Houston. To Dr. Anthony Timmins, whose valuable coding advice saved me some time. To Ejiro Naomi Umaka, who technically introduced me to root coding and later became a wonderful and cheerful friend. To Nalinda Kulathunga, Fabian Ng, who became great support during my initial days. To Corey Myers, who became a great office mate (will never forget his chocolates). To Fernando Antionio Flor, who became a great companion during my stay in Geneva for three months. To Jihye Song, for small valuable advice for the analysis.

I would also like to thank Nirbhay Behera, whom I met during the middle of my Ph.D. I was able to learn some valuable analysis steps and codes from him.

I am very thankful to my roommate Manish Khanal, for being a good friend and understanding when I needed some space for my work.

Lastly, I would like to thank all my family, friends, and everyone else who have supported me and encouraged me with their kind words. I am sincerely thankful to everyone who has been part of my journey in any way possible.

ABSTRACT

Heavy ion collisions at the LHC provide a tool to study the phase transition from hadronic matter to a deconfined phase of quarks and gluons. We investigated whether flavor hierarchy in the QCD transition crossover region could lead to clustering of strangeness. The idea was supported by the enhanced production of strange carrying hadrons in heavy-ion collisions. Kaons are the lightest meson that carry the strange quark and thus they represent around 80% of the total strangeness in the system. We search for clusters of strange quarks in heavy-ion collisions, taking kaons as a proxy, by studying the azimuthal distribution of particles on an event-by-event basis. To find the signatures of clustering, we defined two different observables, probability of event clustering $P(E)$ and Pull distributions. The shape of these distributions is expected to carry the possible clustering signature. We measured the higher moments of these distributions and compared them with the baselines, which have no clustering. These baselines are achieved either through simple statistical considerations of Poissonian particle production, leading to Gaussian signatures, or through analysis of a realistic MC event generator, HIJING, that does not carry any mechanism of generated particle cluster or even flavor hierarchy in the particle freeze-out. We find no explicit evidence for azimuthal strangeness, but the detailed analysis allows us to set more stringent thresholds on the clustering probability. A sensitivity study shows that the higher moments (skewness and kurtosis) are more prone to show a signal. At this time, with the presently available dataset and the resulting statistical and systematic uncertainties on the higher moment measurements, we can state that the strangeness clustering probability in central heavy ion collisions at LHC energies is less than 20%.

TABLE OF CONTENTS

LIST OF TABLES

LIST OF FIGURES

Chapter 1

Introduction

A few microseconds after the Big Bang nearly 14 billion years ago, researchers theorize, the universe transitioned from a hot, dense soup called quark-gluon plasma to hadron gas. These particles make up the universe we know today, but only account for 5% of the matter needed to understand all measured cosmic signals. The remaining 95% is the matter we do not see, known as dark matter [1] [2].

The accelerator program started at the Lawrence Berkeley National Laboratory, Berkeley, where nuclei were first accelerated to relativistic speeds successfully in 1954 [3]. It was then followed by the fixed target experiments such as Alternating Gradient Synchroton (AGS) at Brookhaven National Laboratory (BNL) and Super Proton Synchrotron (SPS) at CERN. Then followed the collider experiments, the Relativistic Heavy Ion Collider (RHIC) at Brookhaven National Laboratory (BNL), which started operation in 2000 and the Large Hadron Collider (LHC) at CERN, which is collecting data since 2010. The main goal of heavy ion collisions has been to understand Quantum Chromodynamics (QCD) under extreme temperature and baryon densities. An essential characteristic of relativistic heavy-ion collisions is the large amount of energy deposited in a tiny space region for a brief period. The nucleons inside the nucleus are made up of elementary particles, quarks and gluons.

These quarks and gluons are confined within hadrons at ordinary temperatures, but they form a deconfined state of matter where quarks and gluons are strongly coupled at high temperatures and densities. This state, known as Quark Gluon Plasma (QGP), can be created in interactions of relativistic heavy-ions at colliders such as the Large Hadron Collider (LHC) [4].

1.1 The Standard Model of Particle Physics

The Standard model is a theory of particle physics describing the elementary particles of matter, quarks and leptons, and their universal behavior, conveyed by three fundamental forces: electromagnetic, strong, and weak [5].

The model lists six quarks and six leptons. Quarks are divided into six flavors (one for each quark type): up (u), down (d), strange (s), charm (c), bottom (b), and top (t). On the other hand, the three lepton flavors consist of a given lepton and a corresponding neutrino: electron (e), muon (μ), and tau (τ).

The fundamental forces act via an exchange of force carriers referred to as gauge bosons. The electromagnetic (EM) force is carried by γ photons exchanged between electrically charged particles. The weak force is mediated by $W^{\pm}$ and Z bosons accountable for nuclear decays due to the ability of change of flavor of both quarks and leptons. Finally, the strong interaction which is moderated by gluons (g), carrying a colour charge, binds the quarks within composite particles, known as hadrons. Lastly, there is a Higgs boson (H), which is responsible for giving the mass (inertia) to all massive particles by its interaction with a scalar Higgs field permeating the entire Universe. An overview of the elementary particles of the standard model is provided in Fig. 1.1, including some of their characteristic qualities such as mass, charge, and spin.

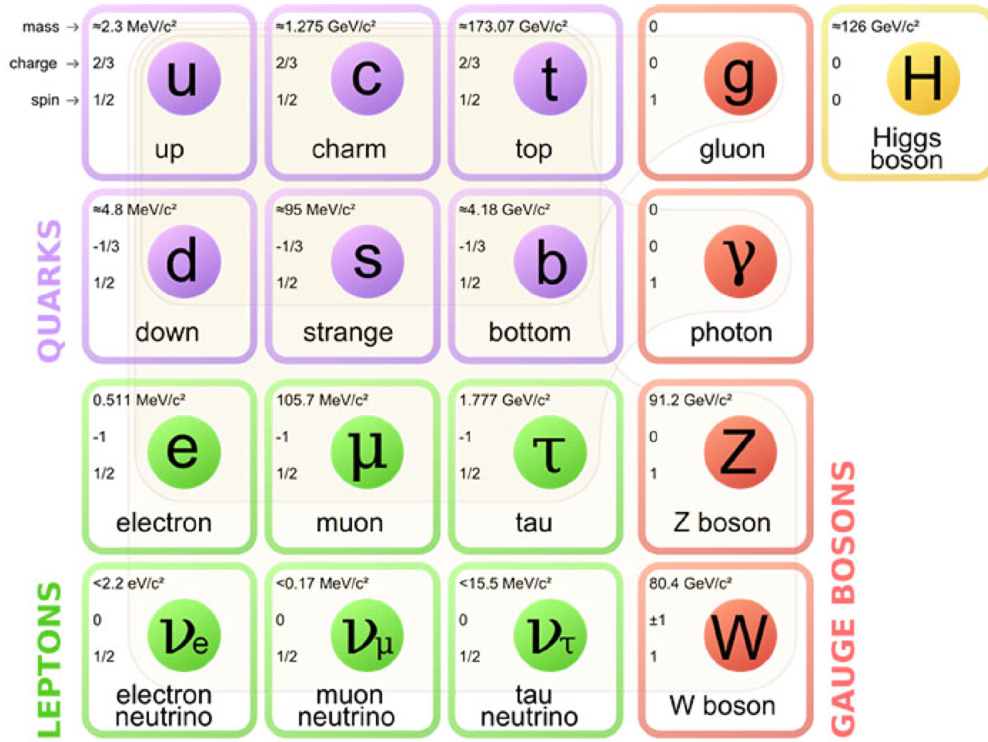

Figure 1.1: The elementary particles in the standard model of particle physics [5].

1.2 Quantum Chromodynamics

Quantum Chromodynamics (QCD) is the theory of the strong interaction between quarks and gluons. Quarks and gluons are the fundamental particles that make up composite hadrons such as protons, neutrons, kaons and pions, etc. It is based on non-abelian $SU(3)$ gauge theory with quarks in the fundamental and gluons in the adjoint representation of the gauge group. The QCD analog of electric charge is a property called color. Gluons are the force carrier of the theory, just as photons are for the electromagnetic force in Quantum Electrodynamics. The six flavors of quarks are fermions with spin 1/2. Three quarks come together in a color neutral state to form baryons, while a quark and an anti-quark together form a colorless meson. Baryons and mesons are together called hadrons. All visible matter around us is made of hadrons. There are eight massless, flavorless, colored gluons with spin

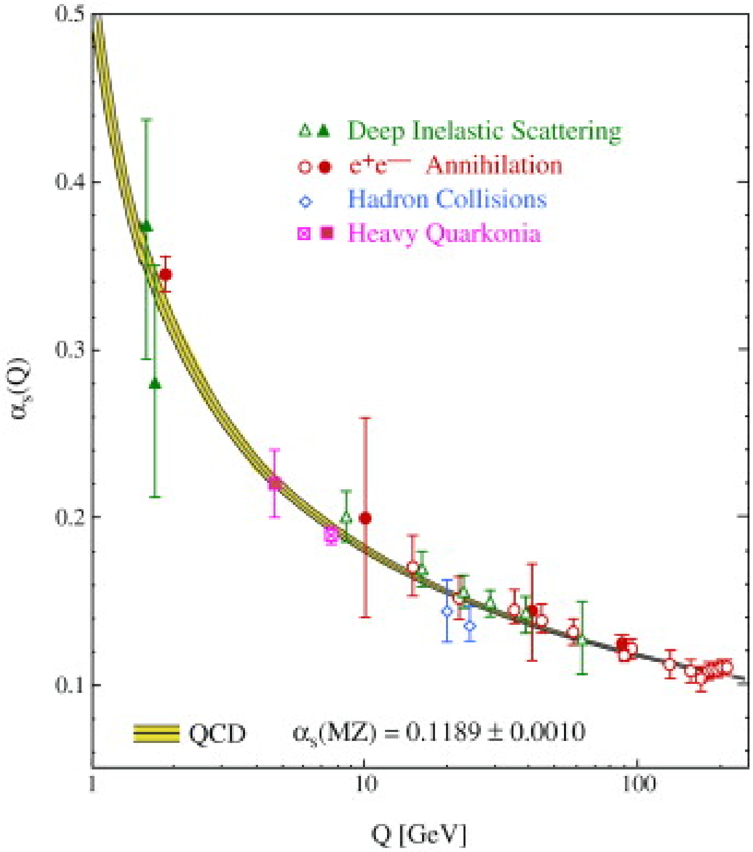

Figure 1.2: Summary of measurements of $\alpha_S(Q)$ as a function of respective scale of momentum transfer Q. Open and filled symbols are from NLO and NNLO QCD calculations, respectively. The curves are obtained from QCD predictions for the combined world average value of $\alpha_S(M_{Z^0})$ [6].

1, which act as force carriers of QCD. QCD is characterized by its two key features, namely, confinement and asymptotic freedom. The coupling constant reflects the interaction strength among various constituents. For QCD interactions, the coupling constant, α_S, is given by

$$\alpha_S = \frac{12\pi}{(11n - 2f)\ln\left(|Q^2|/\Lambda^2\right)}, \tag{1.1}$$

where n is the number of colors, f is the number of flavors, Q^2 is the amount of momentum transferred and Λ is the scale parameter with a value in the range of 100 MeV to 500 MeV. Fig. 1.2 shows the value of α_S as extracted from different experiments and its comparison with results from perturbative QCD(pQCD) [6].

Experimentally, a single quark described by a color triplet state has never been isolated. Their absence suggests that the interaction between quarks and gluons is very strong on large distance scales. This is what is meant by confinement. The idea was pioneered by Ken Wilson [7], within the backdrop of the bag model, which is an effective picture of hadronic structure [8] [9]. In the other extreme, the effective strength of the interaction between quarks and gluons on short distance scales becomes arbitrarily small. This is known as asymptotic freedom and was discovered by David Gross, Frank Wilczek and David Politzer in 1973 [10] [11] [12].

1.3 Quark Gluon Plasma

Based on the nature of strong interactions, in 1974, T.D. Lee proposed the creation of nuclear matter at very high energies, containing asymptotically free quarks and gluons [13]. This deconfined state of nuclear matter is called Quark Gluon Plasma (QGP). It is believed to have existed a few microsecond after the Big Bang [14]. The QGP is defined as a thermally equilibrated state of matter in which quarks and gluons are deconfined from hadrons.

Lattice QCD aims to calculate QCD quantities non-perturbatively and from first principle using lattice gauge techniques on a discretized space-time grid. These calculations predict a phase transition from confined hadronic matter to a deconfined phase of quarks and gluons around a critical temperature (T_c) of 154 MeV [15] and an energy density (ϵ) of 1 GeV/fm^3 [16]. Fig. 1.3 shows the diagram of temperature versus baryon density of the QCD phase structure. The active number of degrees of freedom, indicated by ϵ/T^4, increases rapidly, thereby indicating the formation of a new state of matter (as shown in Fig. 1.4 [16]).

The study of the QGP within the perspective of the QCD phase diagram gives an insight into the thermal properties of strongly interacting matter. The QCD phase diagram, as

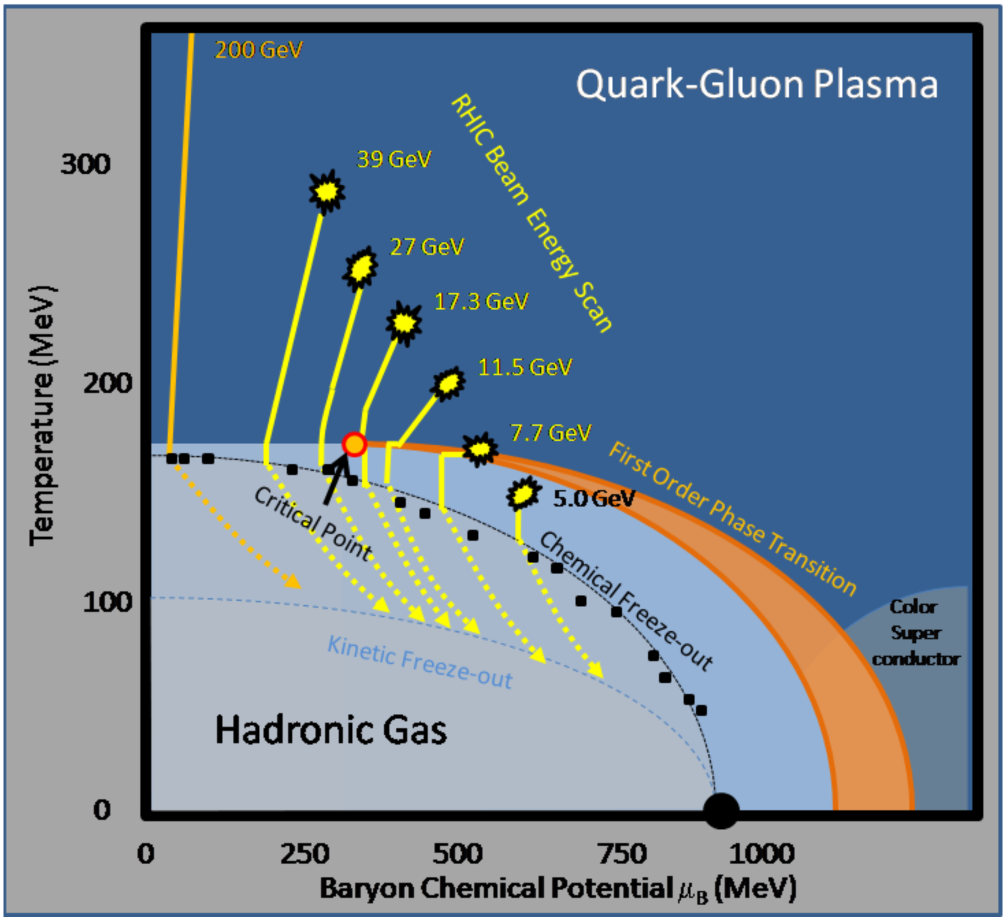

Figure 1.3: A sketch of the QCD phase diagram.

shown in Fig. 1.3, is spanned by baryon chemical potential (μ_B) and temperature (T) [17]. It has several distinct features. Some of them are: (a) high temperature high density phase of deconfined quarks and gluons (QGP), (b) low temperature low density phase of hadrons, (c) nature of quark-hadron transition, and (d) end point of the first order phase transition line, called the critical point (CP). Lattice QCD predicts the phase transition from QGP to hadron gas phase for small baryon chemical potential to be a cross-over transition [18]. Theoretical calculations predict this transition to be a first-order phase transition for large baryon chemical potential that ends in a critical point [19].

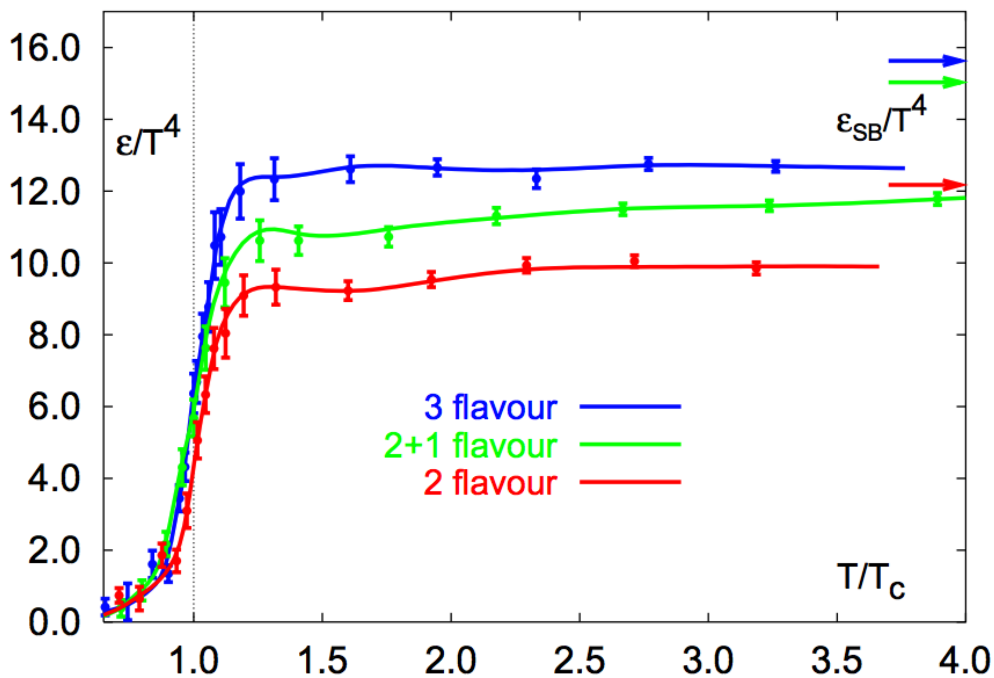

Figure 1.4: The energy density, normalized by temperature, in QCD with different number of degrees of freedom as a function of temperature [16].

1.4 Relativistic Heavy-ion Collisions

The field of relativistic heavy-ion collisions is a fascinating inter-disciplinary area of research at the interface of particle physics and high-energy nuclear physics [20]. It overlaps with thermal field theory, relativistic fluid dynamics, kinetic or transport theory, quantum collision theory, and standard statistical mechanics and thermodynamics.

Results from relativistic heavy-ion collider experiments support the existence of the QGP. Some signatures of the creation of QGP are: enhanced production of strange hadrons in heavy ion collisions [21], J/ψ suppression [22], strong suppression of high energy jets and heavy quarks [23], and large azimuthal asymmetry in the particle yields or elliptic flow, v_2 [24].

1.5 Evolution of Heavy-ion Collision

The space-time evolution of heavy-ion collisions is schematically shown in Fig. 1.5 [25]. The various forms of QCD matter formed during the evolution are discussed below.

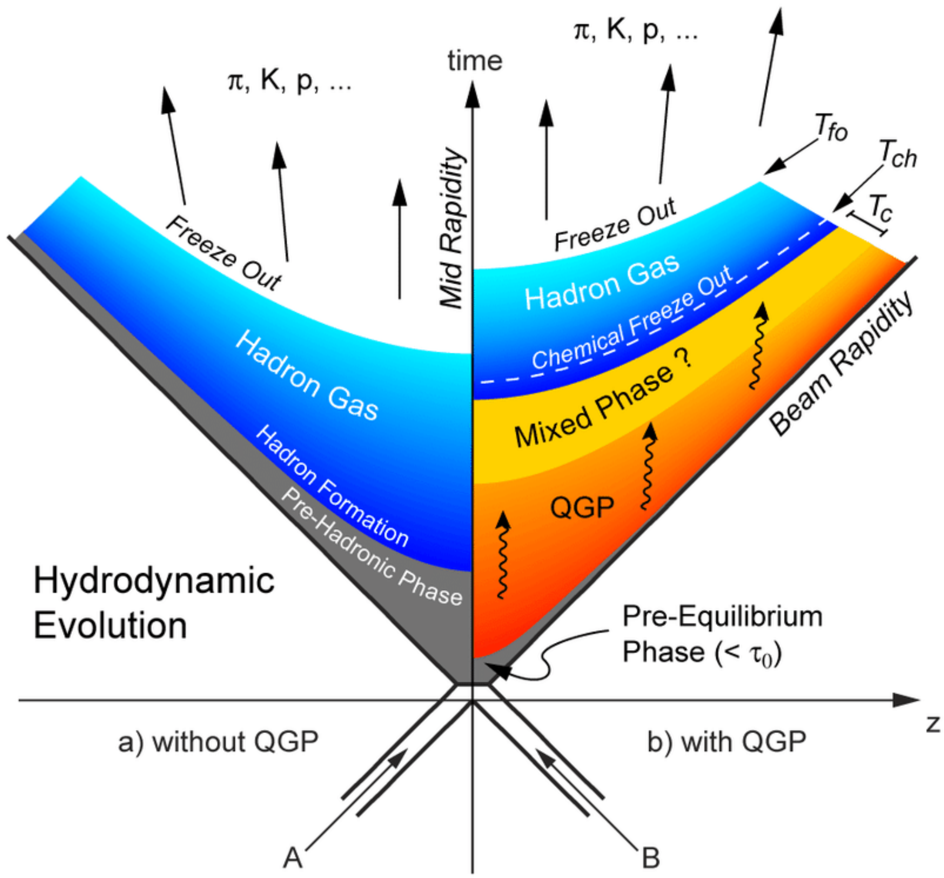

Figure 1.5: Space-time evolution of relativistic heavy ion collisions with (right side) and without (left side) QGP formation.

Before the collisions, the nuclei are accelerated to nearly the speed of light in opposite directions. Due to Lorentz-contraction, they look like thin disks in the centre-of-mass frame, which are contracted along the longitudinal direction by a factor of ~ 100 compared with the radial extent in the transverse plane [26].

At $z = 0$ and $\tau = 0$, the two incoming nuclei collide with each other and the space-time evolution has two possible scenarios: (a) if the energy density and temperature created in the collisions do not attain the critical value necessary for the formation of QGP, the system will behave as a hadronic gas only (left side of Fig. 1.5) and (b) when the initial energy density and/or temperature is very high, quarks and gluons might liberate and produce a deconfined QGP. In this scenario, hard particles, i.e., particles with very high momentum, such as hadronic jets, dileptons pairs, heavy quarks, direct photons, etc. are produced via hard processes, where the interactions involve large momentum ($Q \geq 10$ GeV) transfer. The semi-hard processes corresponding to the momentum transfer of $Q \sim 1$ GeV, start to develop at a time $\tau \sim 0.2\ fm/c$, where the bulk of the partonic constituents are liberated by collisions. At this stage, most of the multiplicity in the final stage is generated via various processes, such as fragmentation of the initial state gluons which undergo a complex evolution. If the produced partons do not interact with each other or the interactions are negligible, they would evolve independently and separate rapidly without an equilibrium state, which is analogous to the situation of low multiplicity pp events at LHC. However, data for the Pb-Pb collisions and high multiplicity pp collisions exhibit collective phenomena which indicate that the partons liberated in the collisions interact strongly. Due to these interactions, the partonic matter rapidly approaches towards thermal equilibrium with relatively short thermalisation time of the order of 1 fm/c. This equilibrated state is known as Quark Gluon Plasma (QGP) state, which is well established by the theoretical lattice QCD calculations. The partonic matter, thus produced, gradually expands and cools down, and eventually at the critical temperature, $T_c = (150 - 170)$ MeV, the colored partons get confined again within colorless hadrons [27]. This hadronization occurs in Pb-Pb collision at the LHC at time, $\tau \sim 10\ fm/c$.

If the phase transition from partonic to hadronic state is of the first order, a mixed phase is expected comprising of quarks and gluons together with the hadrons. Eventually, the hadronic system continues to expand and reach the chemical freeze-out temperature, T_{ch}, where the inelastic collisions among hadrons cease and the relative abundances do not change any more for the hadron species. As the system continues to expand, at time $\tau \sim 20\ fm/c$, thermal freeze-out occurs at temperature, T_{fo}, where the system size becomes smaller as compared to the mean free path of hadrons. At this stage, the elastic scattering between hadrons cease and the particles stream out of the system freely.

1.6 Hadronization Model and its Freeze-out Parameters

Statistical hadronization models are useful in predicting hadron production in ultra-relativistic nucleus-nucleus collisions. The first successful use of a statistical hadronization model was achieved in 1994 using data from Si+Au collisions obtained at Brookhaven AGS facility [28]. Nucleus-nucleus collisions are highly dynamical events. Five distinct stages can be identified through the evolution of the collision, namely: (i) initial collision, (ii) thermalization, (iii) expansion and cooling, (iv) chemical freeze-out, and (v) kinetic freeze-out. A schematic of these stages is shown in Fig. 1.6, where the vertical lines show a demarcation of the different stages.

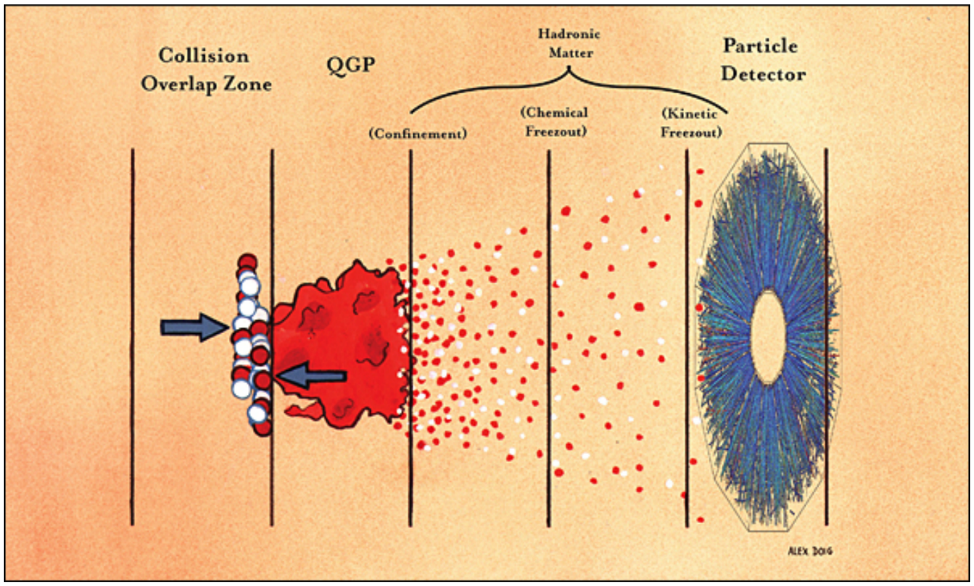

Figure 1.6: State of matter during the evolution of the collision process.

At the initial stage, the fireball is formed. At thermalization, equilibrium is established, while at chemical freeze-out (possible hadronization), inelastic collisions cease, which implies the hadron yields and distribution over species are frozen. At kinetic freeze-out, elastic collisions cease, implying spectra and correlations are frozen. The statistical or thermal hadronization model describes the chemical freeze-out of the collision, which is assumed to be driven by rapid changes in energy and entropy density near the phase boundary [29]. The fireball created in the collision is assumed to be in chemical equilibrium when rapid changes in density near the phase boundary lead to an almost simultaneous freeze-out of all hadrons at the chemical freeze-out temperature, T, and chemical freeze-out baryon chemical potential, μ_B. T and μ_B are the so called freeze-out parameters. The extracted parameters (T and μ_B) as functions of centre of mass energy in the thermal model show that μ_B drops monotonically with increasing collision energy, and T initially increases but levels off at centre of mass energies per collision nucleon pair of 20 GeV and at a temperature of around 160 MeV (as shown in Fig. 1.7 [30]).

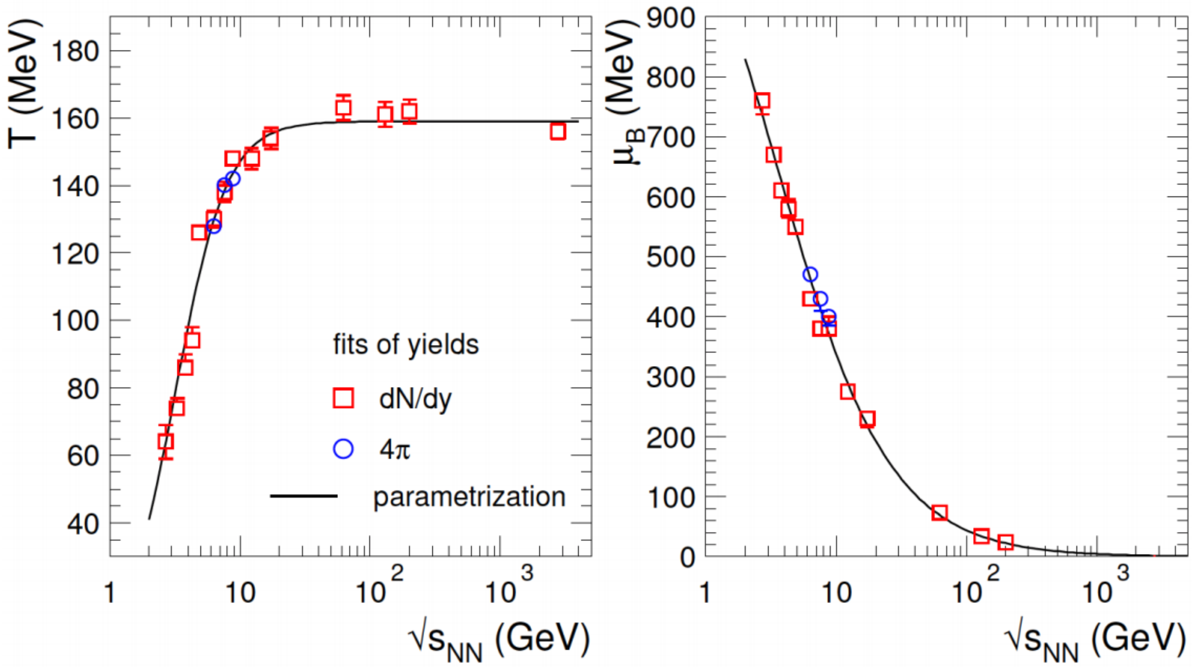

Figure 1.7: Energy dependence of the thermal parameters: T and μ_B. The red square boxes are based on yield measurements. The data are from the mid-rapidity, $y = 0$ (where all the particles are emitted in the transverse direction) [30].

The freeze-out points of Fig. 1.7 can be put together for a phenomenological version of the QCD phase diagram (as shown in Fig. 1.8 [31] [32] [33]).

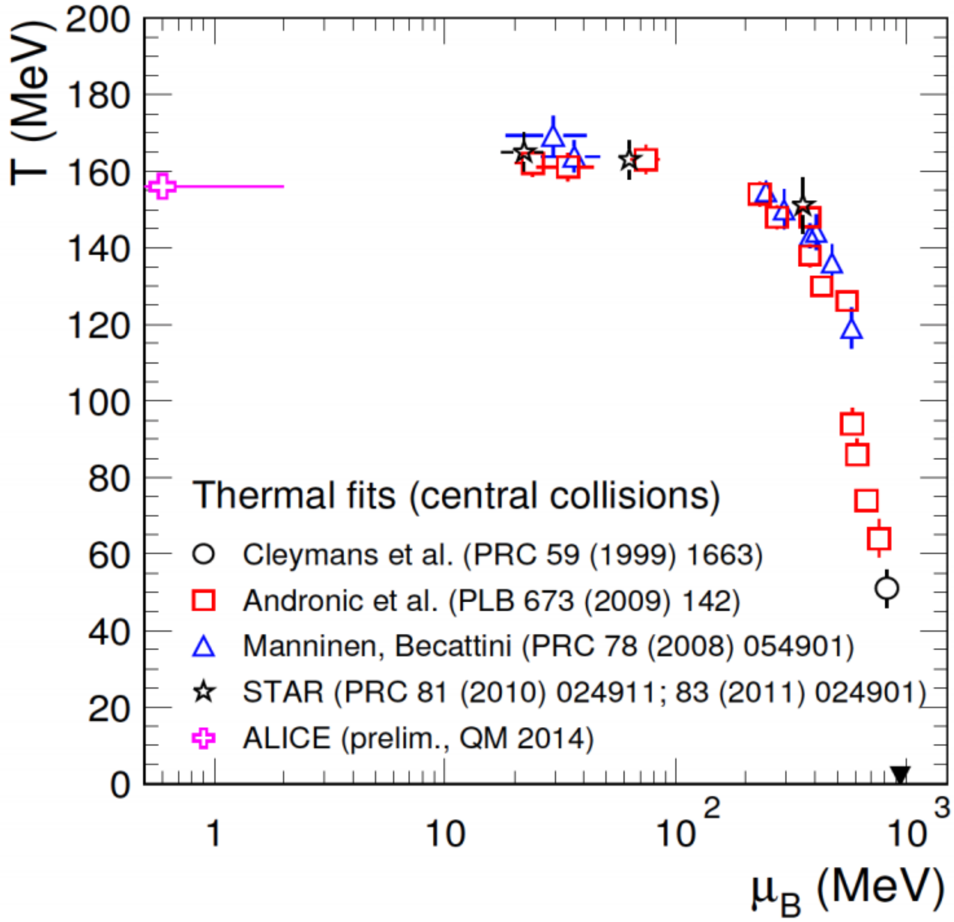

Figure 1.8: Phase diagram of strongly interacting matter assuming chemical freeze-out and hadronization coincide. The points represents the thermal fits of hadron yields at various collision energies [31] [32] [33].

The thermal model fit results show an increase in T with increasing collision energy or equivalently, decreasing μ_B from about 50 MeV to about 160 MeV, where it exhibits a saturation for μ_B at approximately less then 300 MeV. Each thermal model point corresponds to a fit of hadron yields in central Pb-Pb or Au-Au collisions at a given collision energy. The points are from several independent analyses. The success of the thermal model prediction in providing a freeze-out surface supported by QCD theory calculations makes this phenomenological model a very reliable tool in mapping the phase structure of strongly interacting matter.

1.7 Susceptibilities of Conserved Charges

In heavy-ion collisions, conservation laws play an important role in the evolution of the system. The number of baryons, the electric charge and the strangeness quantum numbers are fixed during the entire collision, expansion of plasma and freeze-out. Hence, net-charge (ΔQ), net-baryon number (ΔB), and net-strangeness (ΔS) are regarded as conserved quantum numbers. However, in finite acceptance, these quantities can fluctuate. Fluctuations of conserved quantum numbers are important because they carry information about the freeze-out parameters at the QCD phase transition.

Quantum number fluctuation cannot be measured directly. Therefore, proxies of these quantum number such as, net-charged particles for the net-charge quantum numbers, net protons for the net-baryon quantum number and net-kaons for the net-strangeness quantum number are used. These net-multiplicity distributions can be directly and accurately measured with the help of particle identification techniques used in modern day particle detectors and as a result, fluctuations of conserved quantum numbers can be monitored. The fluctuations of net-particle multiplicity distributions can be related to the theoretically calculated susceptibilities. The susceptibilities in thermodynamics are the derivatives of the pressure with respect to variation in chemical potential and are expressed as,

$$\chi_{lmn}^{BSQ} = \frac{\partial^{l+m+n} p/T^4}{\partial(\mu_B/T)^l \partial(\mu_S/T)^m \partial(\mu_Q/T)^n} \tag{1.2}$$

where, Q, B, and S are charge, baryon number, and strangeness, respectively. l, m, and n are orders of susceptibility. T stands for temperature and μ for chemical potential. Susceptibilities can further be expressed in terms of the partition function as

$$\chi_{lmn}^{BSQ} = \frac{1}{VT^3} \frac{\partial^{l+m+n}(\ln Z)}{\partial(\mu_B/T)^l \partial(\mu_S/T)^m \partial(\mu_Q/T)^n} \tag{1.3}$$

Once the susceptibilities are constructed in theory as a function of temperature and chemical potential, then the extraction of freeze-out parameters can be achieved on the basis of fluctuation measurements. Lattice QCD (LQCD) calculations provide theoretical interpretations of the nature of strong interactions. LQCD puts quarks and gluons on the discrete space-time grid and numerically simulates their interactions. Here susceptibilities can be calculated based on this lattice where gluons live on the lattice links and quarks on the sites. For instance, as explained in [34], at vanishing μ_B, the n^{th} order susceptibility of net-baryon number fluctuations can be calculated as

$$\chi_n^B = \frac{1}{VT^3}\frac{\partial^n \ln Z}{\partial(\mu_B/T)^n}|_{\mu_B=0} \tag{1.4}$$

For small, non-zero values of μ_B, χ_n^B can be approximately calculated by expanding it in a Taylor series as

$$\chi_{n,\mu}^B = \sum_{k=0}^{\infty}\frac{1}{k!}\chi_{k+n}^B(T)(\frac{\mu_B}{T})^k \tag{1.5}$$

Ratios of susceptibilities with appropriate orders are related to the ratios of moments of the measured net-particle multiplicity distributions as

$$\frac{\sigma_B^2}{M_B} = \frac{\chi_{2,\mu}^B}{\chi_{1,\mu}^B},\ S_B\sigma_B = \frac{\chi_{3,\mu}^B}{\chi_{2,\mu}^B},\ \kappa_B\sigma_B^2 = \frac{\chi_{4,\mu}^B}{\chi_{2,\mu}^B} \tag{1.6}$$

Here, M_B, σ_B, and κ_B stands for mean, standard deviation, skewness and kurtosis of net baryon probability distributions, respectively. Consider the Taylor's series expansion of the simplest even-odd ratio, $\frac{\chi^B_{2,\mu}}{\chi^B_{1,\mu}}$

$$\frac{\sigma_B^2}{M_B} = \frac{\chi^B_{2,\mu}}{\chi^B_{1,\mu}} = \frac{T}{\mu_B}\left[\frac{1+\frac{1}{2}\frac{\chi_4^B}{\chi_2^B}(\mu_B/T)^2+...}{1+\frac{1}{6}\frac{\chi_4^B}{\chi_2^B}(\mu_B/T)^2+...}\right] \tag{1.7}$$

A similar relationship holds for the next even-odd ratio, $\frac{\chi^B_{3,\mu}}{\chi^B_{2,\mu}}$. Therefore, to leading order, the above approach can be used to extract the $\frac{T}{\mu_B}$ ratio at the chemical freeze-out at small to vanishing μ_B. The extraction of the freeze-out temperature can be addressed by the even-even ratios of cumulants. For instance, the Taylor's series expansion of $\frac{\chi^B_{4,\mu}}{\chi^B_{2,\mu}}$ at vanishing μ_B gives

$$\kappa_B\sigma_B^2 = \frac{\chi^B_{4,\mu}}{\chi^B_{2,\mu}} = \frac{\chi_4^B(T)}{\chi_2^B(T)}\left[\frac{1+\frac{1}{2}\frac{\chi_6^B}{\chi_4^B}(\mu_B/T)^2+...}{1+\frac{1}{6}\frac{\chi_4^B}{\chi_2^B}(\mu_B/T)^2+...}\right] \tag{1.8}$$

Here, the temperature can be extracted from the explicit temperature dependence of even-even susceptibility ratios to leading order as seen in the above expansion at $\mu_B = 0$.

1.8 Sequential Chemical Freeze-out Temperature

The evolution of heavy-ion collisions is characterized by several steps involving the phase transition from quark gluon plasma to hadron gas. The chemical freeze-out is the moment at which inelastic collisions between particles cease.

Theoretical calculations on the chemical freeze-out conditions (T, μ_B) in the context of different quark masses have been done using the Hadron Resonance Gas(HRG) models [35] [36]. While lattice QCD results study the flavor-dependence of the hadronization parameters. Fig. 1.9 (left) shows a lattice QCD calculations of χ_2^u and χ_2^S where u and s stands for *up* quarks and *strange* quarks, respectively. Both quantities show a rapid rise in a certain

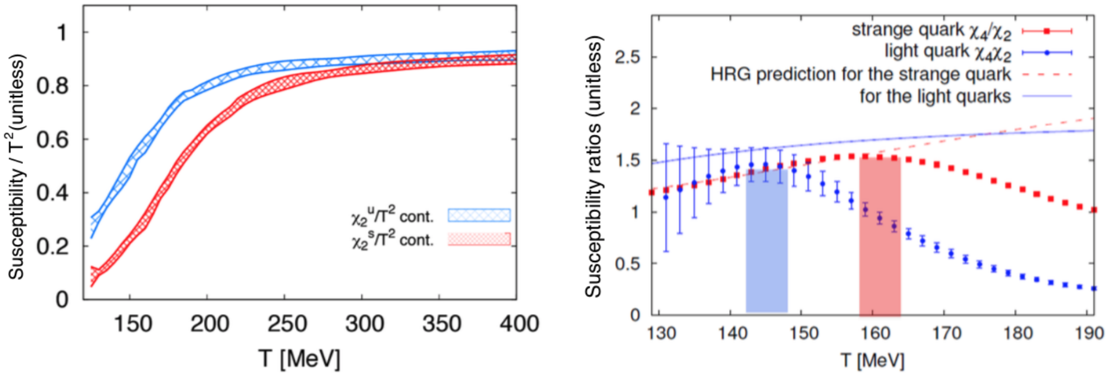

Figure 1.9: (left): Continuum extrapolated lattice QCD results for χ_2^u and χ_2^S, (right): Continuum extrapolated lattice QCD results for χ_4/χ_2 for light and strange quarks in comparison to HRG model calculations [35] [36].

temperature range, and reach approximately 90% of the ideal gas value at large temperature. The temperature around which the susceptibilities rise is approximately 15 - 20 MeV larger for strange quarks than for the light quarks. In addition, the light quark susceptibility shows the steeper rise with temperature, compared to the strange quark one. Fig. 1.9 (right), shows a comparison of χ_4/χ_2 calculated for light and strange quarks using lattice QCD results and HRG results. The main difference between these two calculations is that only lattice calculations include the quark gluon plasma phase. Therefore, the temperature at which the lattice curves deviates from HRG possibly points to the deconfinement temperature and this temperature for light quarks is less than it is for strange quarks.

The prediction of sequential hadronization is also addressed by employing the grand canonical ensemble (GCE) approach within the framework of The FIST HRG model package [37]. Fig. 1.10 presents the calculations of the chemical freeze-out temperature, T_{ch}, based on particle yields from STAR and ALICE measured at collision energies ranging from $\sqrt{S_{NN}} =$ 11.5 GeV to 5.02 TeV. Based on a splined fit to the thermal fit parameters at all energies, the authors of Ref. [37] calculated a light flavor freeze-out temperature $T_L = 150.2 \pm 2.6$ MeV and a strange flavor freeze-out temperature $T_S = 165 \pm 2.7$ MeV at vanishing μ_B. The

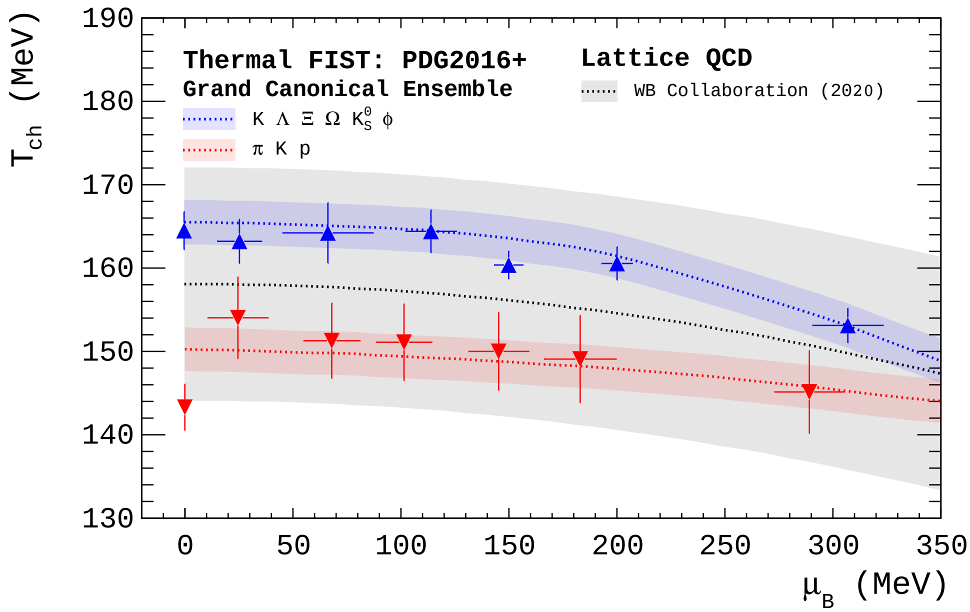

Figure 1.10: Strange (blue) and light (red) GCE fits to STAR and ALICE data measured at collision energies ranging from $\sqrt{S_{NN}}$ = 11.5 GeV to 5.02 TeV (0-10%) via The FIST using the PDG2016+ hadronic spectrum [37].

paper shows evidence for flavor-dependent chemical freeze-out temperatures in the crossover region of the QCD phase diagram.

1.9 Strangeness Enhancement

Being a second generation quark, strange (s) quarks are only present in the original nuclei (before the collision) as sea quarks and in negligible numbers, in comparison to the number of s and $\bar{s}$ inside hadrons after the freeze-out. Therefore, most of the strangeness is produced in the collision. Furthermore, the small mass of these quarks - close to the temperature of the QGP transition - allows for the thermal production of s and $\bar{s}$ pairs through the annihilation of gluon pairs during the QGP phase. The abundant presence of gluonic excitation is also responsible for the fast rate of thermalization. Thus, compared with a Hadron Gas scenario (HG), the QGP formation would lead to an enhancement of multi-strange hadrons with respect to non-strange particle production. Historically, this *strangeness enhancement* was the first proposed signature for the QGP, by Rafelski and Muller in the late 80's [38] [39].

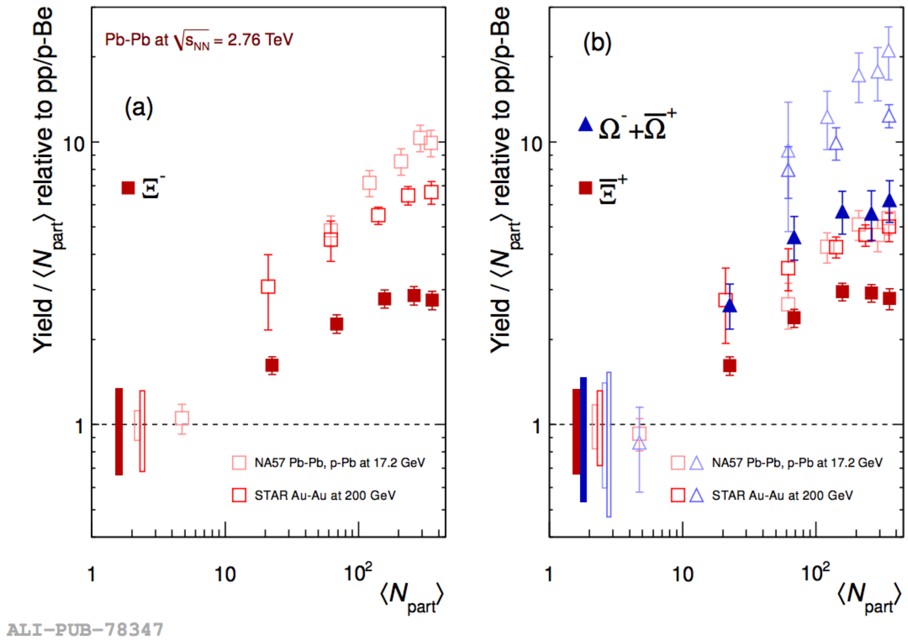

Figure 1.11: Enhancement of multi-strange particles in the mid-rapidity range ($|y| < 0.5$) as a function of the number of nucleon participants in the collision, $< N_{part} >$, observed at the LHC (ALICE with full markers), RHIC and SPS (light hollow markers). Boxes on the dashed lines represent the statistical and systematic uncertainties of the pp/p-Be reference [40].

The enhancement was observed in heavy ion collisions from $\sqrt{s_{NN}}$=17.3 GeV (SPS) to $\sqrt{s_{NN}}$= 200 GeV (RHIC) all the way to $\sqrt{s_{NN}}$=2.76 TeV (LHC). Fig. 1.11 [40] shows the total production rate (yield) of Ξ and Ω at mid-rapidity ($|y| < 0.5$) normalized by the average number of nucleons that interacted in the collision, $< N_{part} >$, relative to pp/p-Be as a function of $< N_{part} >$. The increase of the production rate of strange particles with respect to pp collisions (where no QGP was expected) is clear, with up to 20 more Ω per event for the most central event class analysed by the NA57 experiment.

The increase in relative hyperon production with multiplicity can also be understood as the removal of the canonical suppression. For small systems, exact quantum number

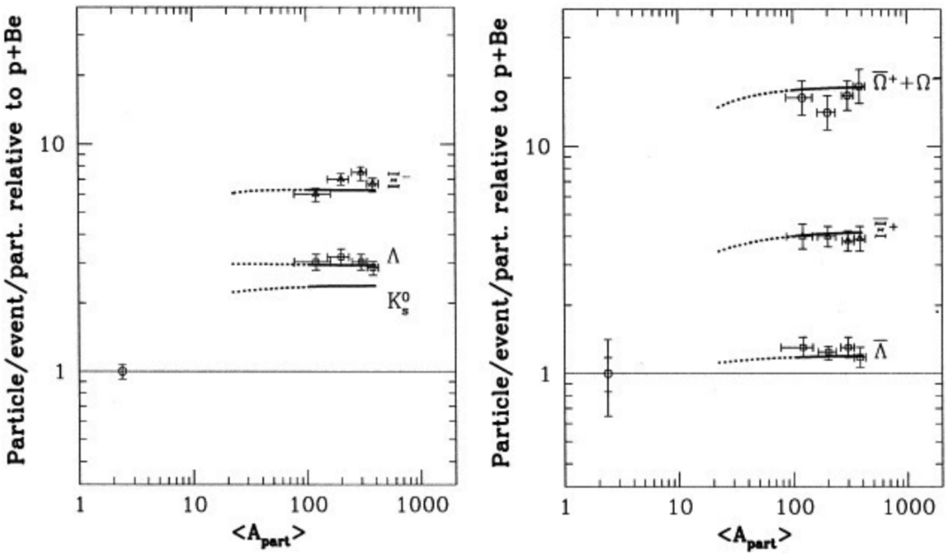

Figure 1.12: Strangeness enhancement calculated in canonical ensemble, with the particle yields/participant for strange baryons and anti baryons as a function of number of participant nucleons, $< A_{part} >$, together with data of Pb-Pb relative to p-Be from WA97 [41].

conservation is required, unlike AA where the larger volume allows for the treatment within the grand-canonical formalism. In this context, the exact conservation of the quantum number is enforced by working in the canonical ensemble for the statistical model. This conservation leads to the reduction of the phase space available for particle production, which reduces the relative strangeness production for smaller systems. The effect of the removal of this suppression as the system size increases can be seen in Fig. 1.12 [41], where predictions of hyperon production in the canonical ensemble are shown. Moreover, we observe the quark content hierarchy, with state of quark configurations of Λ, Ξ, and Ω first being the most affected by the model. The prediction also shows the saturation around $< A_{part} >$, 100, where the enhancement becomes almost constant. Saturation in this context means that the system has become big enough to be treated grand canonically and strange particle production relative to non-strange particle production is constant. For comparison, data from WA97 is also shown (Fig. 1.12).

One of the differences between the predictions of the canonical and grand-canonical approach is related to the ϕ meson production. Being composed of a strange quark and anti-quark pair, this particle has zero net strangeness and charge, therefore should not be subjected to the canonical suppression mechanism. On the other hand, the ϕ meson production should increase with multiplicity in the context of the classic strangeness enhancement mechanism which is due to strange quark/antiquark production through gluon pair annihilation. Besides, being composed of two strange quarks, its enhancement should be similar to the one observed for Ξ. Fig. 1.13 [42] shows the ratios of p, K_s^0, Λ, ϕ, Ξ, and Ω to pions as a function of charge particle multiplicity in various systems at different energies.

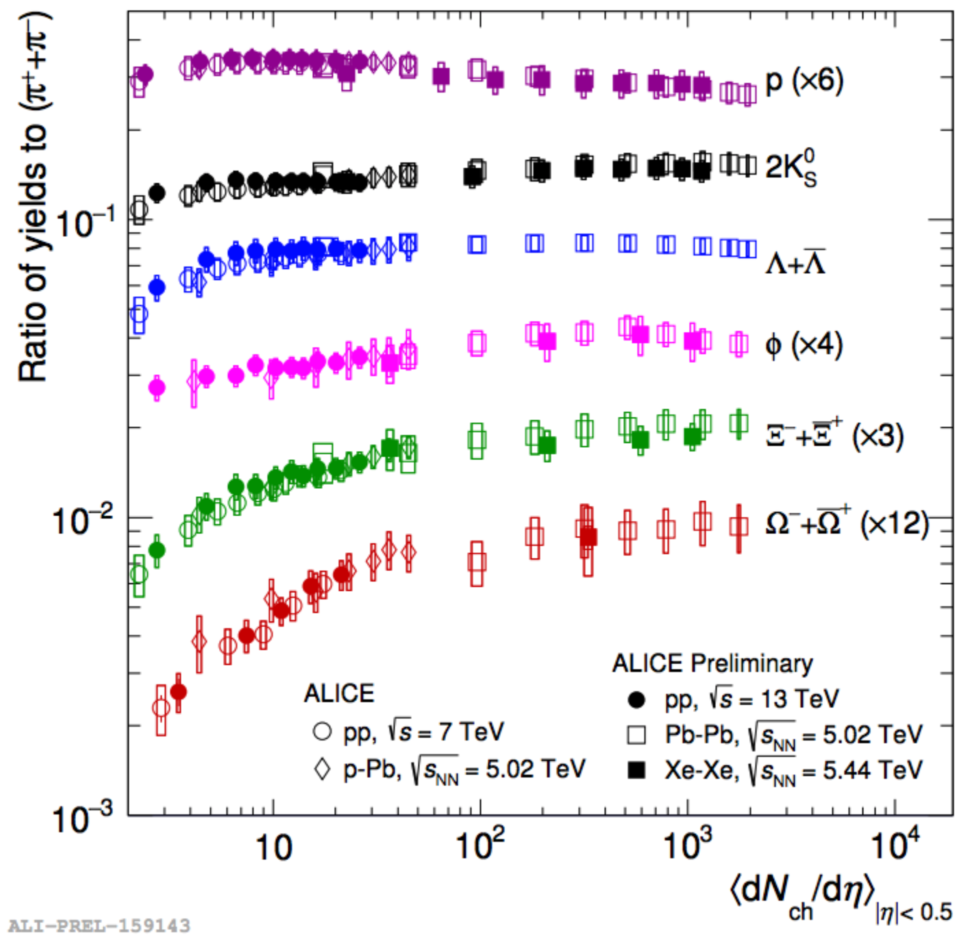

Figure 1.13: p_T-integrated yield ratios to pions ($\pi^{+}+\pi^{-}$) as a function of ($dN_{ch}/d\eta$) measured in $|y| < 0.5$ [42].

A significant enhancement of strange to non-strange hadron production is observed with increasing charge particle multiplicity in pp and p-Pb collisions. The larger the strangeness content of the particle, the stronger the observed enhancement. This effect is due to enhancement and not due to baryon number or mass of hadrons. The net strangeness content of the ϕ meson is 0, while the net strangeness of the Ξ is 2 and Λ is 1. The ϕ meson behaves like a strange baryon and the enhancement is somewhere between the Λ and Ξ enhancement.

On the experimental side, recent ALICE results [43] show that the hyperon to pion ratio as a function of the charged particles at mid-rapidity in the final state has universal behavior across different collision systems and energies, showing a continuous increase from low multiplicity pp collisions, through the intermediate system of p-Pb and reaching a saturation value for central Pb-Pb collisions, as can be seen in Fig. 1.14. Furthermore, we see that the usual string fragmentation model (shown here as the PYTHIA8 curve) alone cannot describe the data well, only after the inclusion of the rope mechanism, present in the DIPSY model, we achieve a good agreement between data and model.

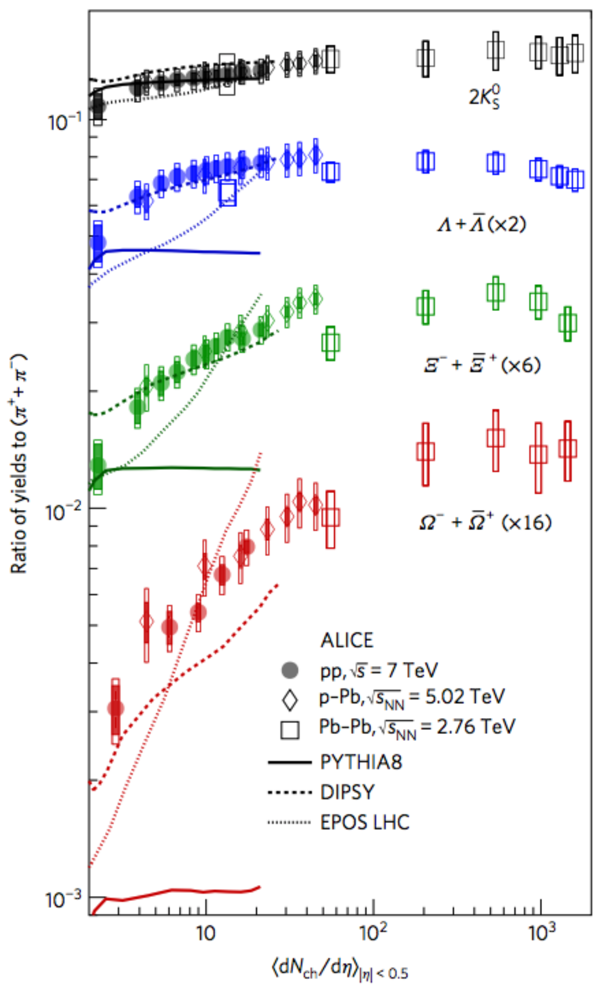

Figure 1.14: p_T-integrated strange particle yield ratios to pions $(\pi^+ + \pi^-)$ as a function of $(dN_{ch}/d\eta)$ measured in $|y| < 0.5$. The empty and dark shaded boxes show the total systematic uncertainty and the contribution uncorrelated across the multiplicity intervals, respectively [43].

1.10 Aim of this Dissertation

My analysis aims to research a probable implication of the two phenomena observed while analyzing the phase transition from QGP to hadron gas.

The first phenomenon, i.e., the sequential freeze-out temperature [37], suggests a flavor dependence in the chemical freeze-out temperature. This likely indicates that strange quarks experience confinement, resulting in the production of strange particles, at slightly higher temperatures. A higher temperature has two consequences, (a) a higher yield and (b) clustering because the baryons carrying light quarks cannot be produced yet.

The second phenomenon, i.e., the strangeness enhancement, revealed an enhanced production of strange hadrons [43]. However, if we observe the visible universe, we know today, most of the matter is made up of light (u, d) quarks. There are assumptions that strange quark matter could exist in the core of neutron stars [44], which could explain the high density of such stars.

Hence, if there is an enhanced production of strange-carrying hadrons at the time of hadronization or at the beginning of the universe, where are they now? They could be inside the core of heavy stars like neutron stars or they could be in a cluster form in some parts of the universe. This motivates us to assume that during hadronization, there is a possibility of the formation of strange quark clusters at some location in phase space. In this analysis, we are searching for clusters of strange-carrying hadrons in azimuthal space. Kaons $(K^{+}+K^{-})$, which are the lightest mesons carrying strange quarks, represent around 80% of the total strangeness in the system. They will therefore serve as a good proxy for the strangeness measurement. We perform an event-by-event analysis of identified kaons in order to search for the cluster of strange quarks in azimuthal space.

Chapter 2

A Large Ion Collider Experiment

In this chapter, the description of the experimental setup is presented. The chapter starts with a brief introduction to the Large Hadron Collider (LHC) in section 2.1. It is followed by the description of the ALICE detector coordinate system in section 2.2. Section 2.3 describes one of the main experiments at CERN: A Large Ion Collider Experiment. It is followed by the detailed description of the two main tracking and particle identification detectors used in this analysis: the Inner Tracking System (ITS) in section 2.4 and Time Projection Chamber (TPC) detector in section 2.5. The chapter is concluded with the description of the VZERO detector (section 2.6) and centrality determination (section 2.7), both being integral parts of the analysis.

2.1 Large Hadron Collider (LHC)

The Large Hadron Collider (LHC) [45] is the world's largest and most powerful accelerator, situated near Geneva, Switzerland, built within the European Organisation for Nuclear Research (CERN) during 1998 to 2008. The LHC consists of a 27 km ring of superconducting magnets with a number of accelerating electric field structures to boost the energy of the particles along the way.

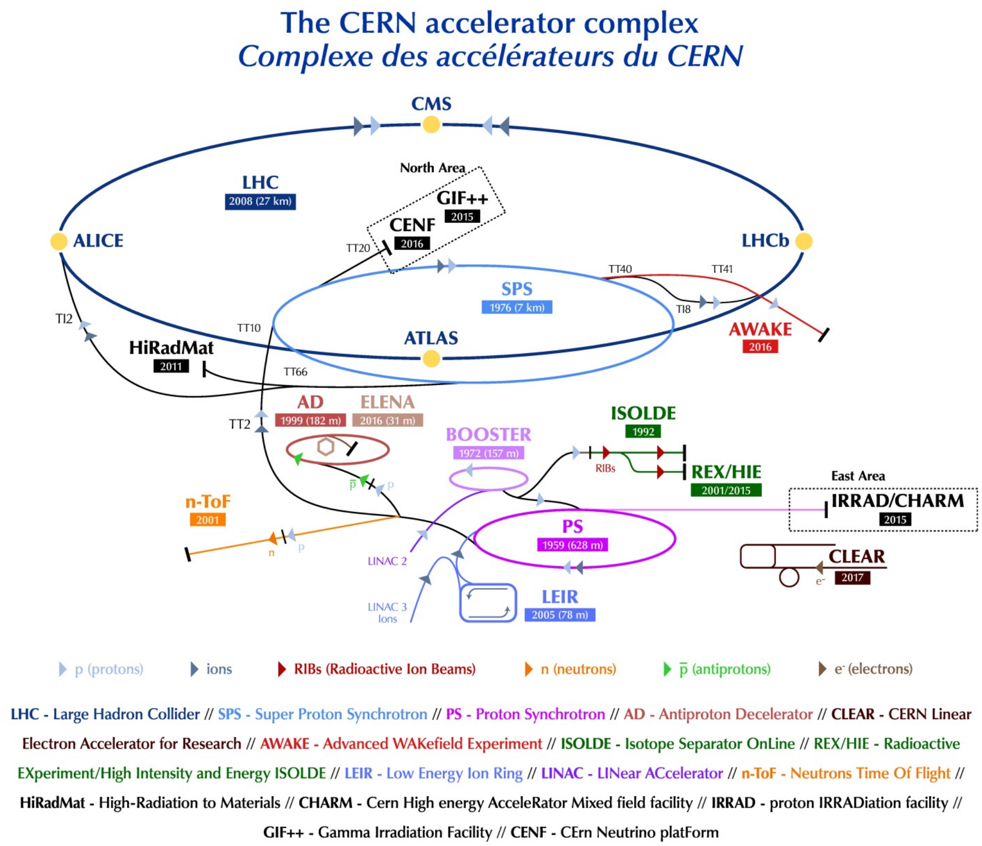

Figure 2.1: CERN's accelerator complex.

As depicted in Fig. 2.1, two beams which travel with relativistic speeds through the accelerators in opposite directions collide at four main interaction points. The four interaction points comprise of four main experiments namely, ATLAS (A Toroidal LHC Apparatus), CMS (Compact Muon Solenoid experiment), LHCb (LHC beauty) and ALICE (A Large Ion Collider Experiment).

CMS and ATLAS are general purpose experiments, built with the same goal and designed mainly for *pp* collisions to detect the Higgs boson and study physics beyond the standard model. The experimental set-ups of each of these experiments are different. The LHCb experiment specializes in investigating the slight difference between matter and antimatter by studying particles containing the b quark.

ALICE is a collider experiment built to study strongly interacting matter, i.e., Quark Gluon Plasma (QGP), formed at very high temperature/energy density by colliding two heavy-ions at relativistic energies. ALICE presently has collected data for different collision systems, namely, p-p, p-Pb, Pb-Pb, and Xe-Xe collisions at various colliding energies.

2.2 ALICE Coordinate System

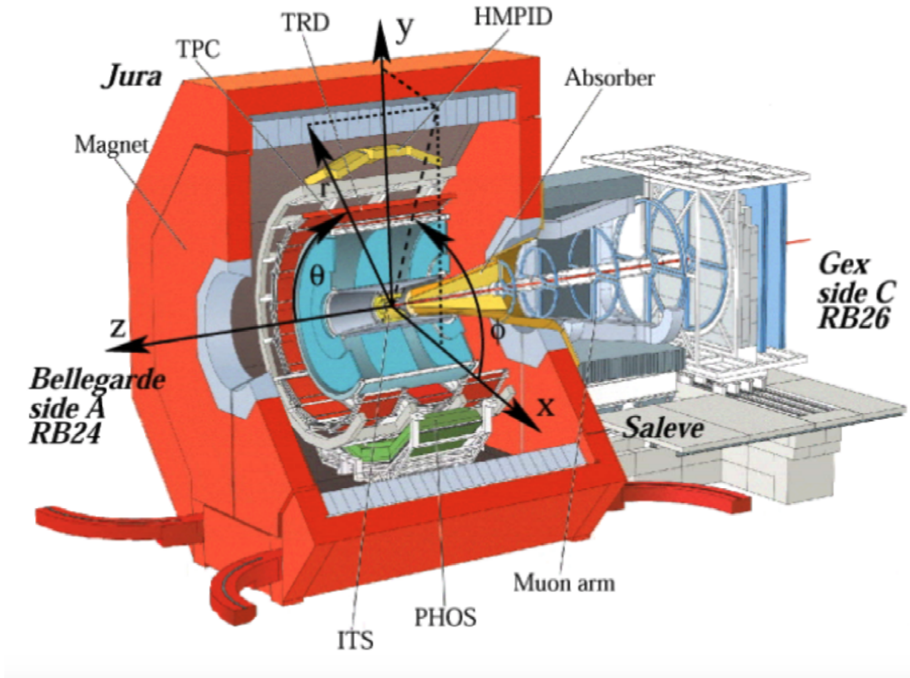

Figure 2.2: The ALICE coordinate system [46].

For a better assessment of the ALICE detectors and data analysis, it is important to understand the ALICE coordinate system. Fig. 2.2 describes the ALICE coordinate system [46]. Taking the beam interaction point as the origin (x,y,z) = (0,0,0), the ALICE coordinate system is described in terms of the right-handed cartesian coordinate system. The coordinate system can be described as follows:

1. z-axis: The z-axis is taken along the beam direction known as longitudinal direction. The positive direction of the z-axis is taken from the origin towards the side A (ATLAS side), whereas the negative z-axis is towards the side C (CMS side).

2. x-axis: The x-axis is transverse to the z-axis, which is aligned to the local horizontal and pointing towards the accelerator centre. From the origin (x,y,z) = (0,0,0) to the accelerator centre is designed as positive x, whereas the negative x is from the point of origin to the outward direction.

3. y-axis: It is pointing upward and perpendicular to the x-axis. From the point of origin to the upward direction is designated as positive y, whereas the negative y is from the point of origin to the downward direction.

4. Azimuthal angle (ϕ): It is measured with respect to the x-axis in counter clockwise direction. The azimuthal angle bears a special place in this dissertation. We are searching for clusters of strange-carrying hadrons along the azimuthal bins.

5. Polar angle (θ): It is measured from the z-axis to the x-y plane. The polar angle is associated with the pseudorapidity, η, defined as,

$$\eta = -\ln[\tan(\frac{\theta}{2})] \tag{2.1}$$

2.3 A Large Ion Collider Experiment (ALICE)

ALICE (A Large Ion Collider Experiment) [47] is a detector dedicated to heavy-ion physics at the Large Hadron Collider (LHC). It is designed to study the physics of strongly interacting matter at extreme energy densities and extreme temperature. It allows a comprehensive study of hadrons, muons, electrons and photons produced in heavy-ion collisions. The collaboration counts more than 1000 scientists from over 100 physics institutes in 30 countries.

The current set-up of the ALICE detector [47], containing 18 sub-detectors, is shown

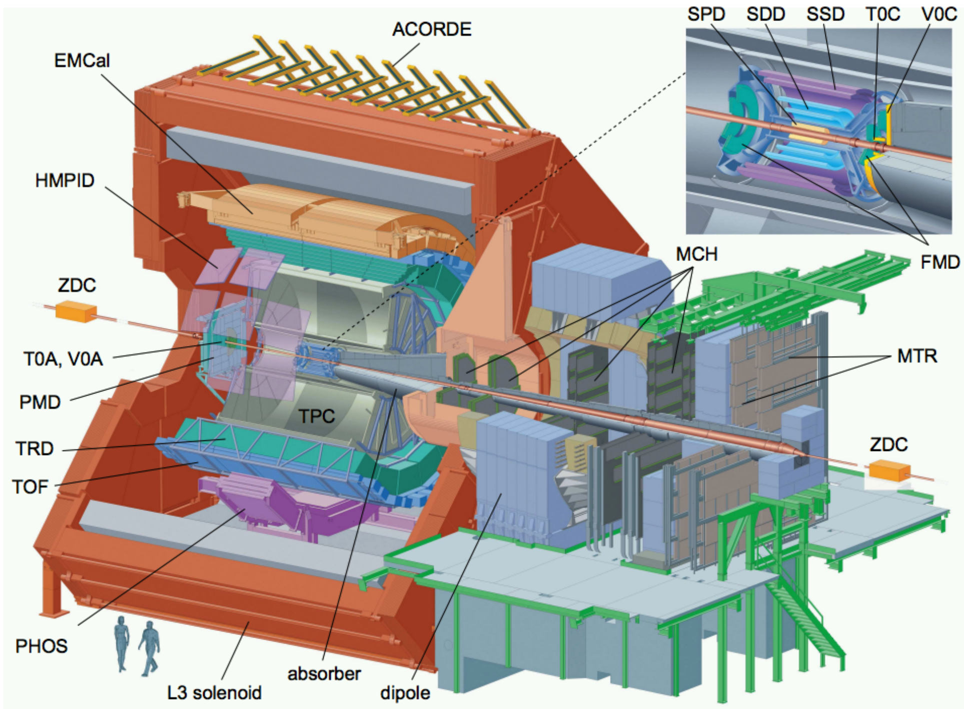

Figure 2.3: ALICE detectors at CERN LHC [47].

in Fig. 2.3. The whole ALICE detector is mainly categorized into two components- (a) the central barrel, contained inside the large L3 magnet and made up of detectors that are devoted mainly to hadron detection. This component covers the pseudorapidity range of $-0.9 < \eta < 0.9$ over the full azimuth, (b) the forward muon spectrometer, dedicated to studying the muon pairs produced in the interactions. It covers the angular acceptance of $2^{\circ} < \Theta < 9^{\circ}$, i.e., a pseudorapidity range of $2.5 < \eta < 4.0$. It makes use of the usual techniques for muon identification at small angles [48].

In the central barrel, the Time Projection Chamber (TPC) detector surrounds the Inner Tracking System (ITS) as shown in Fig. 2.3. The TPC and ITS detectors are mainly dedicated to the determination of primary and secondary vertices and tracking of low-momentum particles. Outside the TPC, the Transition Radiation Detector (TRD) is used to identify various particles like pion, kaon, proton, etc. Further, there are two single armed detectors-the Photon Spectrometer (PHOS) and High Momentum Particle Identification (HMPID). At very forward angles, the Zero Degree Calorimeter (ZDC) measures the energy flow. Two additional detectors VZERO-A and VZERO-C are mainly used for event classification and trigger purposes, which are located on both sides of the ALICE central barrel. The detectors used in this analysis are Inner Tracking System (ITS), Time Projection Chamber (TPC), which is used for particle identification, and VZERO detector, which is used for event classification. The following sections are dedicated to these detectors.

2.4 Inner Tracking System (ITS)

ITS is the innermost detector of ALICE, placed closest to the interaction point (IP) [49]. It is mainly used for improvement of impact parameter, and primary vertex determination with a momentum resolution better than 100 μm. The ITS also provides secondary vertex reconstruction of hyperon decays, particle identification and track reconstruction of low-momentum particles. The ITS is composed as a six-layer cylindrical vertex detector with two layers of Silicon Pixel Detector (SPD), Silicon Drift Detector (SDD), and Silicon Strip Detectors (SSD) each as shown in Fig. 2.4. The innermost layer (SPD) is located at radial distance of 3.9 cm and outermost layer (SSD) at 43 cm in the pseudorapidity interval, $\eta < 0.9$.

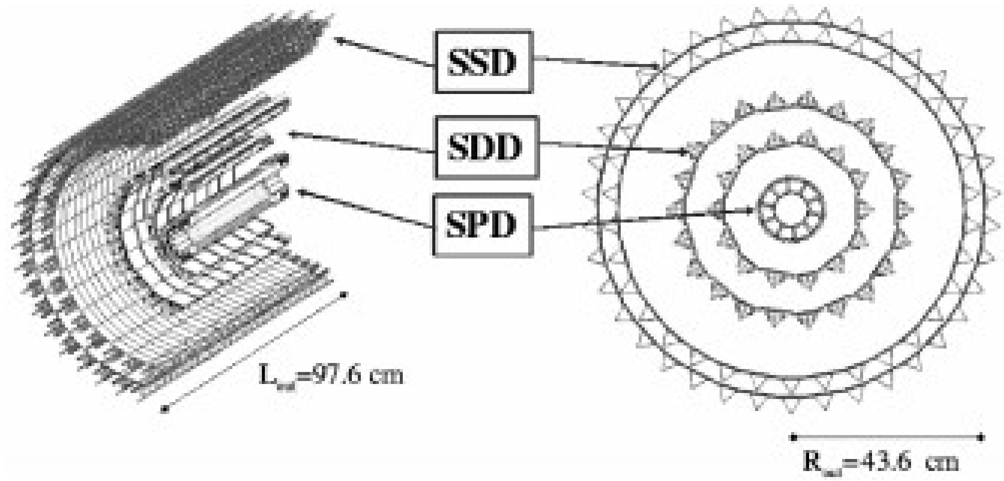

Figure 2.4: A schematic of the ITS detector.

2.4.1 Silicon Pixel Detector (SPD)

The SPD consists of two innermost layers of the ITS, located at a distance of 3.9 cm and 7.6 cm from the beam axis. Its main aim is to determine the primary and secondary vertex as well as the measurement of impact parameter of secondary tracks. SPD operates in a high track density environment of around 50 cm^{-2}. SPD has hybrid silicon pixels of size 50 $\mu m(r\phi) \times 425$ $\mu m(r\phi)$ and contains 9.8×10^6 cells. The extended pseudorapidity coverage of $|\eta| < 1.98$ provides uniform track matching with the Forward Multiplicity Detector (FMD).

2.4.2 Silicon Drift Detector (SDD)

These are two intermediate layers of the ITS positioned at 15 cm and 23.9 cm from the beam axis. In this region, the particle density reaches up to 7 cm^{-2}. SDD's have multi-particle tracking capability and provide energy loss measurements for particle identification.

2.4.3 Silicon Strip Detector (SSD)

SSD's are the outermost layers of the ITS at a distance of 38.0 cm and 43.0 cm from the beam axis. Both layers are equipped with the double-sided Silicon Strip Detectors and cover the pseudorapidity range $|\eta| < 0.9$ with the full azimuthal coverage. The SSD connects the ITS tracks to the tracks in the TPC and also provides dE/dx information.

2.5 ALICE Time Projection Chamber (TPC)

The Time Projection Chamber (TPC) [50] is the main tracking central barrel detector in ALICE. It serves as a primary detector, used for reconstruction of charged particle trajectories providing up to 160 space-points for each individual track. Also, it is capable of determining particle transverse momentum in a wide range of $0.1 < p_T < 100$ GeV/c from the curvature of the corresponding track in the magnetic field.

In addition, it provides particle identification (PID) information based on measurement of the characteristic ionisation energy loss dE/dx. The PID capability in terms of separation between various particle species is illustrated in the measurement of the distribution of energy loss as a function of particle momentum in Pb-Pb collisions at $\sqrt{s_{NN}} = 5.02$ TeV shown in Fig. 2.5. The solid lines represent the expected detector response to the corresponding particle species.

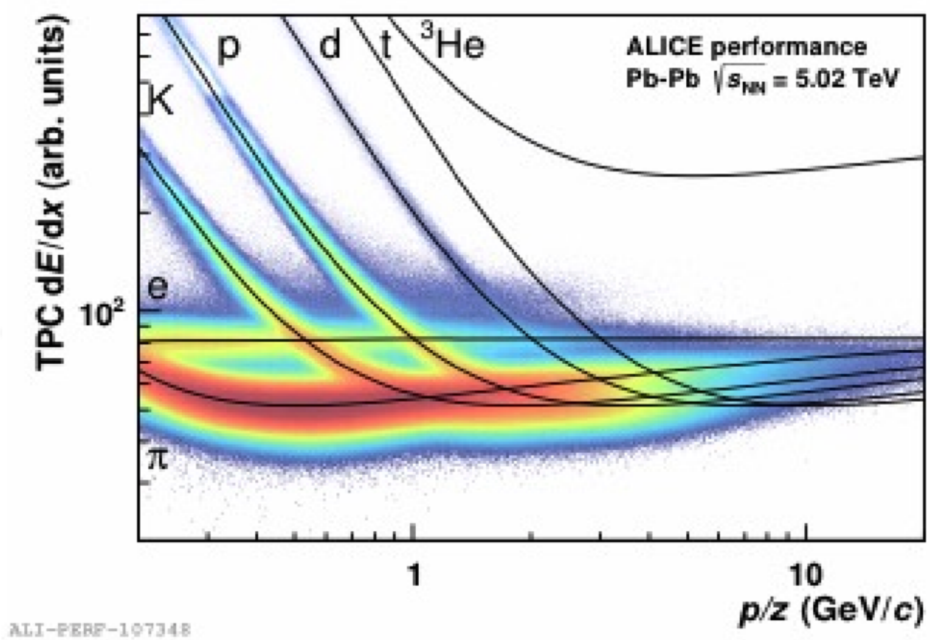

Figure 2.5: Specific energy loss (dE/dx) in the TPC vs. particle momentum in Pb-Pb collisions at $\sqrt{s_{NN}}$=5.02 TeV.

Particle identification (PID) is done using the information based on the theoretical expectation obtained by the famous Bethe-Bloch energy loss formula [51],

$$< \frac{dE}{dx} >= \frac{4\pi N e^4}{m_e c^2}\frac{Z^2}{\beta^2}(\ln\frac{2m_e c^2\beta^2\gamma^2}{I} - \beta^2 - \frac{\delta(\beta)}{2} \tag{2.2}$$

where m_e is the rest mass of the electron, Z is the charge of the particle, N is the number density of electrons in the gas medium, I is the mean excitation energy of the atom and β is the velocity of the charge particle (ALICE uses a parametrized form of Bethe-Bloch formula proposed by the ALEPH experiment [51]). The momentum resolution is $\sim$ 6% below 10 GeV/c and the dE/dx resolution is better than 5% for isolated tracks. The TPC can give a 3-dimensional information of charged particle tracks, which is done by Kalman filtering [52]. Kalman filtering is a statistical estimation and prediction technique, used to estimate the state of a dynamic system. It is used both for track finding and fitting. The Kalman filter algorithm splits the volume of the TPC in 36 trapezoidal sectors. The first phase finds track segments inside the sectors. It starts with the cellular automation that identifies links between hit triplets arranged close to the straight line, followed by the evolution step that concatenates links. This yields short track segments of usually 4 to 10 hits, which are fit with a simplified Kalman filter. The fitted particle trajectory is extrapolated through the TPC volume, adjacent hits are collected without following multiple track hypotheses, and the fit is refined. The second phase merges the track segments found in the individual sectors and performs the final track fit with the full Kalman filter. The TPC only tracking efficiency saturates around 90%. The azimuthal resolution and longitudinal resolution are within 1110 to 1250 μm. The TPC, in conjunction with other detectors, is also used for vertex determination and generation of fast online High-Level Trigger (HLT) for the selection of rare events.

The TPC is a large cylindrical chamber surrounding ITS consisting of a large field cage, and two read-out endplates, each divided into 18 trapezoidal segments as illustrated by its cross-section in Fig. 2.6 [50].

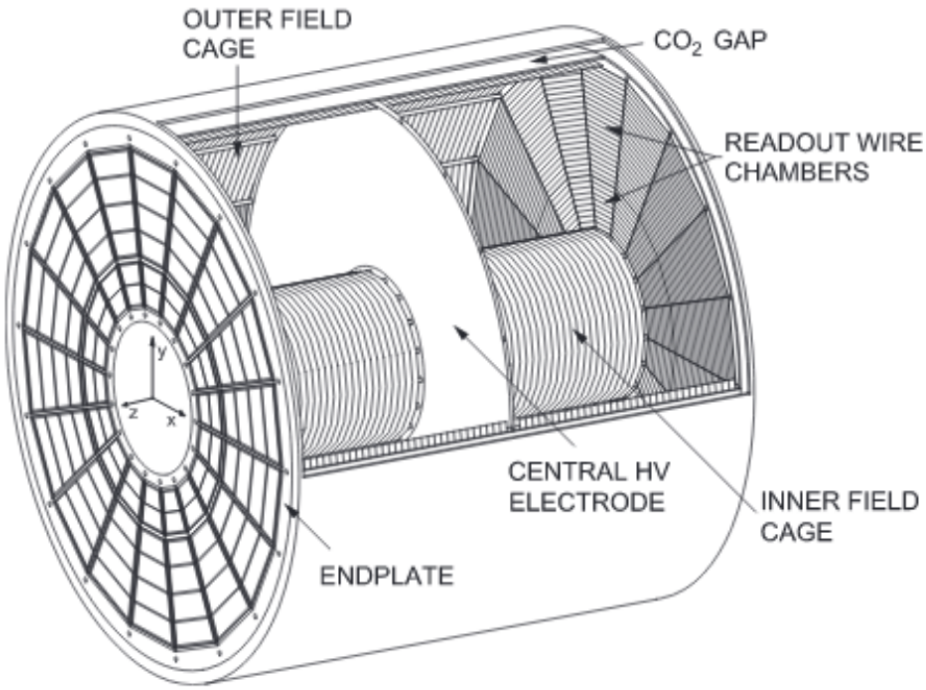

Figure 2.6: 3D view of the TPC field cage. The end plates with 18 sectors and 36 readout chambers on each end are shown [50].

In the middle, i.e., z = 0, the field cage is divided by a central electrode to provide the drift field. Given the overall length of 5 m and the inner and outer radius of 85 cm and 250 cm, respectively, its total active volume is approximately 90 m^3. It is filled with a mixture of Ne, CO_2, and N_2 gas while varying its composition for performance optimization. It covers full azimuth $(0-2\pi)$ and pseudorapidity, $|\eta| < 0.9$ (and $|\eta| < 1.5$ for tracks with reduced length). The end-plates contain 36 Multi-Wire Proportional Chambers (MWPC) with almost 560,000 readout pads.

When a charged particle passes through the sensitive volume of the TPC, it ionises the gas molecules present in the chamber, creating free electrons and ions. These products of ionization then drift towards the electrodes, which generate an electrostatic drift field of 400 V/cm. The central electrode collects the ions while the electrons drift towards the end-plates as illustrated in Fig. 2.7 [53]. When arriving close to the anode plane, a high

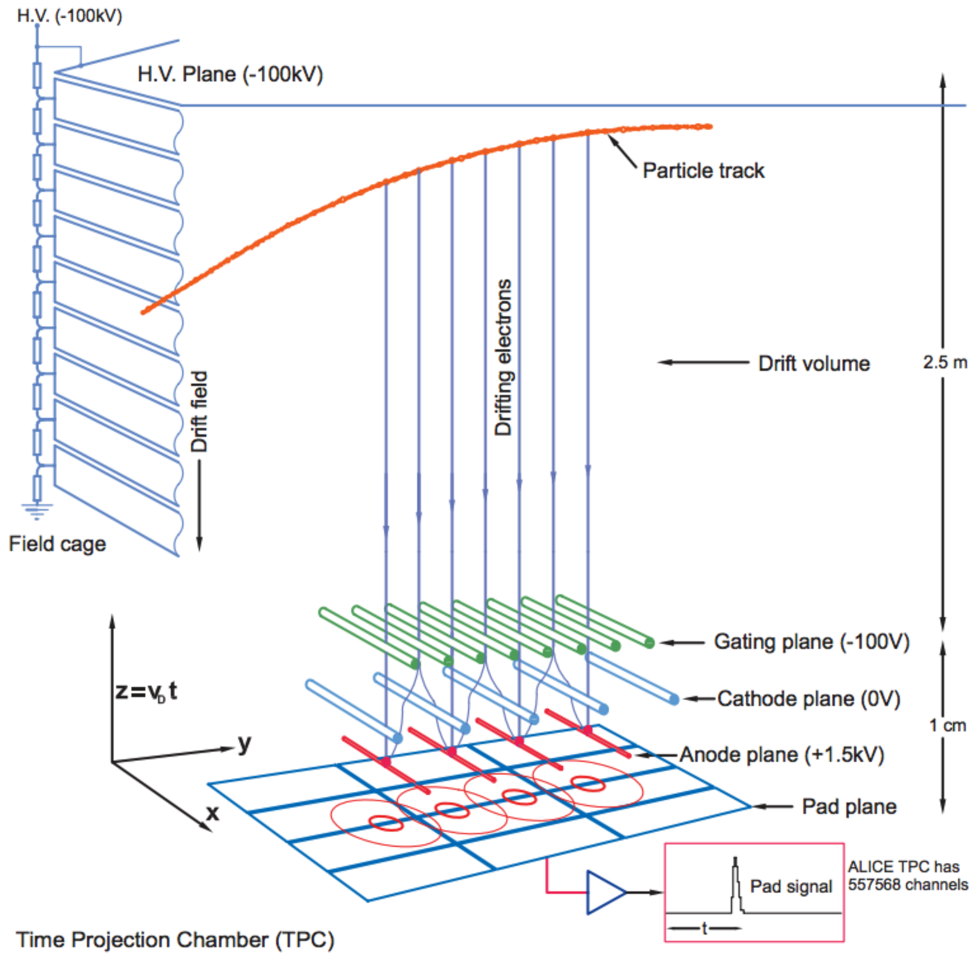

Figure 2.7: An illustration of track reconstruction of charged particle passing through the TPC [53].

electric field gradient creates an avalanche of electrons, resulting in additional production of secondary electrons and ions. Working in the proportional mode, the number of secondary produced electrons carries information about the number of primary-produced electrons and thus the energy loss of the passing particle. On the other hand, the secondary ions induce a signal in the pad rows, giving the information about the position within the transverse xy plane. Moreover, a gating plane is located in front of MWPCs. By alternating its voltage between ± 100 V, it can be either opened or closed. The gate is open for approximately 90 μs intervals, which is a maximal drift time of electrons from the centre towards the endplate.

When closed, primary electrons are collected by the gate wires and do not reach the anodes, while most of the secondary ions are prevented from entering the main body of the TPC, which would result in distortions of the electrostatic field.

Outside of the LHC operation, the TPC is aligned and calibrated by using information about incoming cosmic radiation. Additional calibration is possible with a laser-emitting system [54], even when hadron beams are present. It is capable of shooting coherent laser rays into the TPC volume, providing a set of straight tracks used for precise online monitoring of position reconstruction and potential space-charge distortion.

2.6 VZERO Detector

The VZERO [55] detector consists of two scintillator arrays known as VZERO-A and VZERO-C, one positioned towards ATLAS and the other towards CMS. VZERO-A and VZERO-C are situated at 90 cm and 340 cm on either side of the collision vertex (z = 0) with pseudo-rapidity coverage of $-3.7 < \eta < -1.7$ and $2.8 < \eta < 5.1$ respectively.

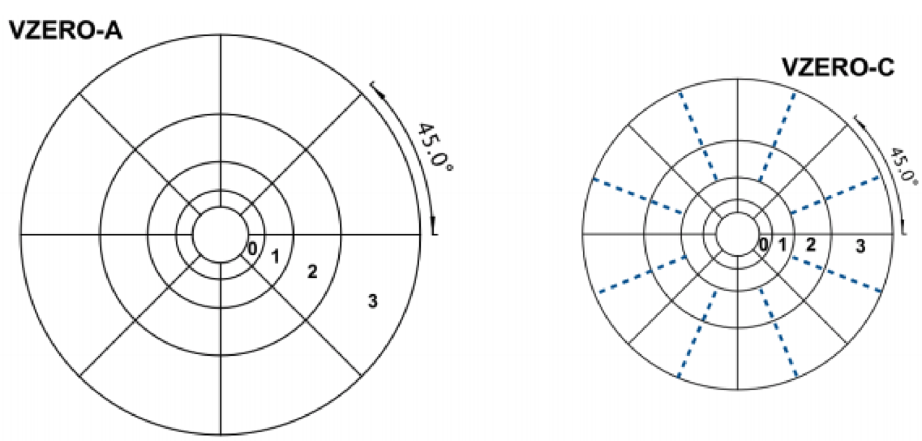

Figure 2.8: Sketches of VZERO-A and VZERO-C arrays showing their segmentation

As shown in Fig. 2.8, each of the VZERO arrays is segmented into four rings in the radial direction and is divided into eight sections in the azimuthal direction. The VZERO detector provides multiple roles such as - a minimum bias trigger for central barrel detectors, a centrality indicator, two centrality triggers for Pb-Pb collisions with control of the luminosity and a validation signal for the muon trigger [55]. The VZERO detector works on the basic principle that all charged particles give the same average response because they travel at the same velocity, $\beta = \frac{v}{c} \approx 1$, which gives a total signal that is correlated with the number of particles in the detector. The VZERO response amplitude is fitted with a Monte-Carlo simulation of the Gaubler model, in order to extract centrality for each Pb-Pb event.

2.7 Centrality Determination

The dynamics of a heavy-ion collision is driven by the initial geometry, given by the overlapping region (and thus interaction volume) of the two colliding nuclei. It seems natural to quantify the level of overlap by an impact parameter b, the distance in transverse xy-plane between the geometrical centers of the two nuclei.

Besides the impact parameter, there are additional quantities related to the geometry of the collision: the number of binary collisions N_{col} between the nucleons of the two projectiles, and the number of participants N_{part}. Participants are those nucleons which undergo at least one nucleon-nucleon collision, while those that avoid other nucleons and endure the collision untouched are call spectators, as shown in Fig. 2.9 [56].

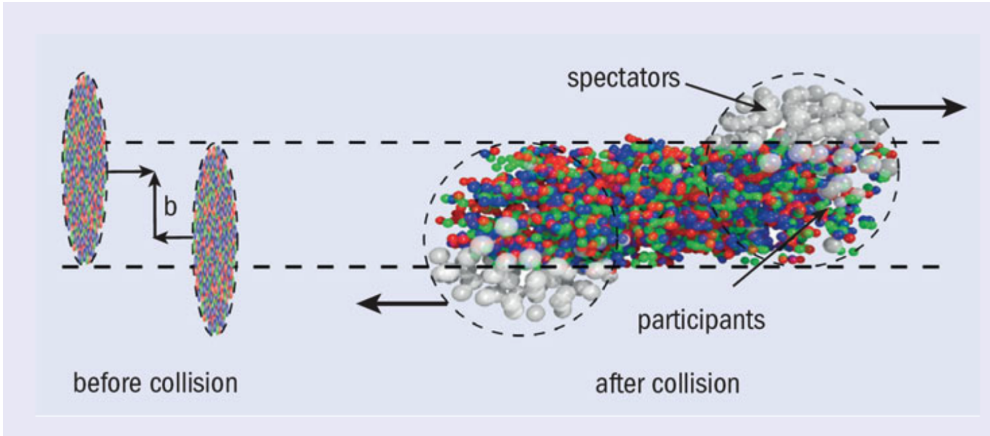

Figure 2.9: A schematic of the two Lorentz contracted ions before and after the collision (b is the impact parameter) [56].

Customarily, collisions are characterised by the centrality (or centrality class) expressed in terms of percentile [56]. For example, a perfectly aligned collision when the two nuclei are fully overlapped, i.e, $b \approx 0$, is referred to as a most central, denoted as 0%. As the overlapping region gets smaller, the impact parameter, b, increases and reach the stage of semi-central collisions. In case the impact parameter approaches the distance between the two nuclei, the collision is referred to as peripheral, and its percentage gets close to 100%. However, neither the impact parameter itself nor the above mentioned geometrical quantities are directly accessible experimentally.

One way to quantify the centrality of a given collision is by looking at the overall signal registered in the forward region. For that purpose, the VZERO detector serves as a suitable centrality estimator due to the proportionality between the magnitude of the measured signal and the number of interacting particles. The distribution of the measured total VZERO amplitude is given by the sum of two VZERO's arrays, VZERO-A and VZERO-C. The distribution can be fitted with a Glauber model [57], as shown in Fig. 2.10 for Pb-Pb collisions at $\sqrt{s_{NN}} = 5.02$ TeV. Measuring the centrality in the forward direction and the anticipated physics signal in the central barrel eliminates the possibility of a bias by avoiding

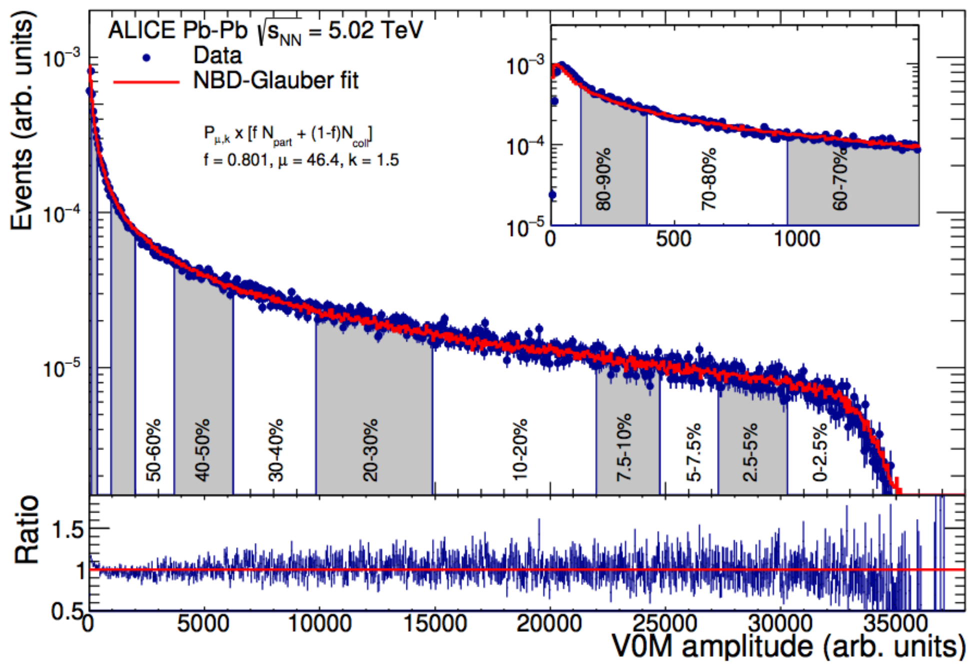

Figure 2.10: Distribution of amplitude measured by the VZERO detector in Pb-Pb collisions at $\sqrt{s_{NN}} = 5.02$ TeV [57]

auto-correlations between two independent measurements.

Chapter 3

Clustering Phenomenon and its Observables

As briefly introduced in Chapter 1, we assume that the formation of strange quark clusters could be initiated by the simultaneous occurrence of strangeness enhancement [43] and sequential freeze-out [37]. In order to probe for clusters of strange quarks (taking Kaons as a proxy for strange quarks) in azimuthal space, we propose to perform an event-by-event analysis of the following parameters which we believe to be good observables for clustering.

3.1 Probability of Event Clustering

We define the probability of event clustering, $P(E)$, as the ratio of the multiplicity of particles produced in a particular azimuthal region to the ratio of the total number of particles produced in the event.

$$P(E) = \frac{N_i}{\sum_{i=1}^{6} N_i} \tag{3.1}$$

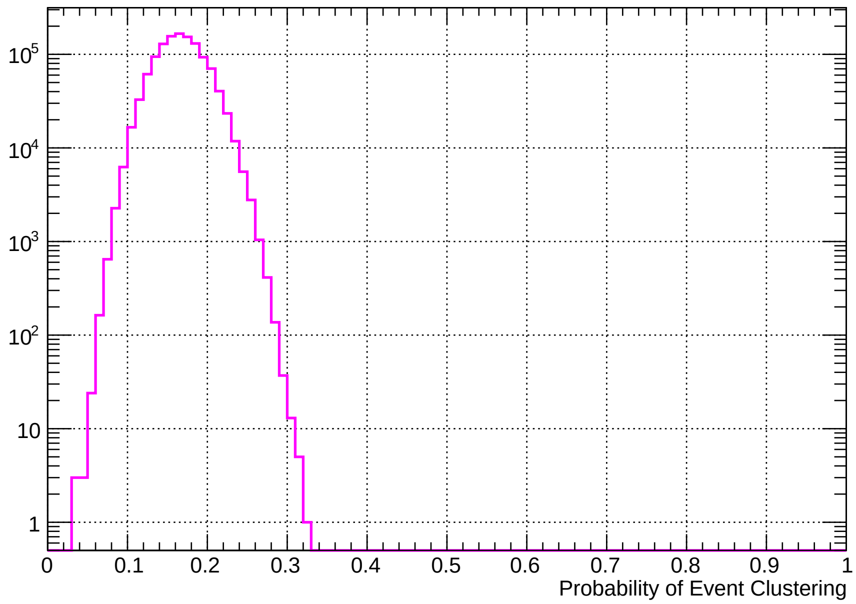

Figure 3.1: Event-by-event distribution of probability of event clustering $P(E)$.

where N_i is the number of Kaons $(K^+ + K^-)$ in the azimuthal region i. Fig. 3.1 shows the distribution of $P(E)$. In this analysis, we divide the azimuthal region into six different bins. The shape of the distribution of P(E) is expected to be Gaussian, hence the higher moments of the distribution of $P(E)$ should carry the possible clustering information. Therefore, the central moments of the event by event distribution of $P(E)$ are defined as our observable.

3.2 Difference and Pull Distributions

The Difference distribution is defined as,

$$Difference_i = N_i - \frac{\sum_{i=1}^{6} N_i}{d} \tag{3.2}$$

where N_i is the number of Kaons $(K^+ + K^-)$ in the azimuthal region i and d is the number of azimuthal divisions.

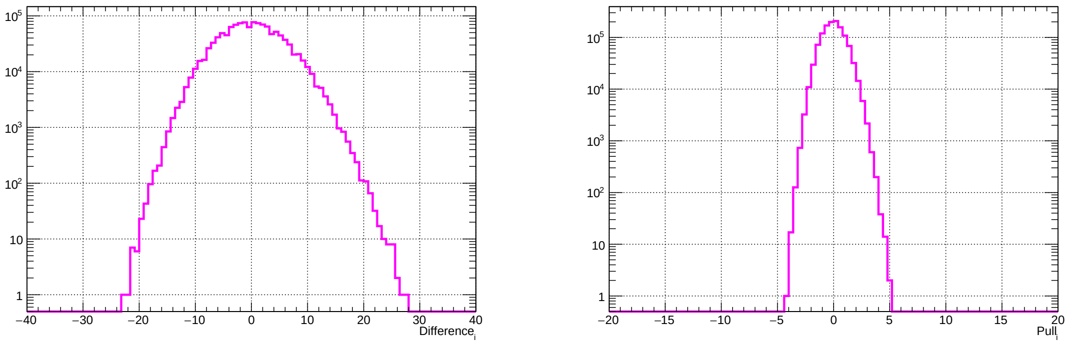

Figure 3.2: (Left): Event-by-event distribution of $Difference_i$ distribution, (Right): Event-by-event distribution of $Pull_i$ distribution.

We get the Pull distribution from the Difference distribution, by dividing by the standard deviation of the difference distributions for corresponding mixed data.

$$Pull_i = \frac{Difference_i}{\sigma_{mixed}} \tag{3.3}$$

We also expect to get the information about clustering from the shape of these distributions. Hence, the central moments of the Pull distribution are considered an additional observable. Fig. 3.2 (left) shows us the Difference distribution and when that distribution is normalized by the standard deviation from mixed event distribution, we get the Pull distribution, as shown in Fig. 3.2 (right). The advantage of the Pull distribution over the distribution of probability of event clustering is that, in the case of the Pull distribution, we normalize the parameter with the mixed event data in order to filter out the clustering information, if there is any.

3.3 Statistical Distributions of the Observables

We assume the multiplicity distribution of positive and negative charged kaons to be Poissonian. The Poisson distribution is a discrete probability distribution that expresses the probability of a given number of occurrences in a fixed interval of time, given that the mean rate of occurrence is known and that the likelihood of occurrence is not dependent on the time since the last occurrence. In particular, the average number of one kind of particle in one event to the next is known, and its occurrence in one event is not affected by the occurrence in the next event.

Within Poisson statistics, if the average number of one kind of particle from one event to the next is λ, then for the number of occurrences: k = 0, 1, 2, ..., its probability function is given by

$$P_{PD}k = \frac{\lambda^k}{k!} \exp\left(-\lambda\right) \tag{3.4}$$

A Poisson distribution can be completely described by its mean (μ). Hence, knowing the mean, one can estimate the standard deviation σ of the distribution from Equation (3.5),

$$\sigma^2 = \mu \tag{3.5}$$

This is not the case for our observables, the moments of $P(E)$ and Pull distributions. Here, the mean for the observables is constant with respect to the change in number of particles generated per event. Hence, the mean is a constant. If we change the number of particles generated per event, other moment values like *standard deviation* (σ), *Skewness* (S), *Kurtosis* (κ) are subject to change. Therefore, the distribution of the observable is assumed to be a Gaussian distribution. The Gaussian probability is defined as

$$P_G = \frac{1}{\sigma\sqrt{2\pi}} \exp\left[-\frac{1}{2}\left(\frac{x-\mu}{\sigma}\right)^2\right] \tag{3.6}$$

where, the parameters μ and σ in Equation (3.6) correspond to the mean and standard deviation of the function, respectively.

3.4 Baseline Studies

After the central moment values and uncertainties for the observables are calculated, their values must be compared to appropriate baseline in order to look for possible signatures of clustering. The baselines used in the analysis are described below.

3.4.1 Central Limit Theorem

According to the theory of probability, the Central Limit theorem (CLT) states that, after a sufficiently large number of iterations of independent random variables, each with the well defined mean value and well defined variance, a normal distributions will emerge regardless of underlying distributions. Here two points have to be emphasized. The random variables must be identically distributed and they are independent. CLT is used to understand the evolution of various order moments with respect to events belonging to a certain centrality class as long as N can be considered as a source of independent emission of particles. With this description, the first four moments of net particle multiplicity distributions can be expressed in terms of N (as described in Ref [58]),

$$Mean(M)\ \alpha\ < N > \tag{3.7}$$

$$StandardDeviation(\sigma)\ \alpha\ \sqrt{< N >} \tag{3.8}$$

$$Skewness(S)\ \alpha\ \frac{1}{\sqrt{< N >}} \tag{3.9}$$

$$Kurtosis(\kappa)\ \alpha\ \frac{1}{< N >} \tag{3.10}$$

3.4.2 Mixed Events

Another baseline can be obtained by generating so called mixed event distributions, by randomly selecting the number of particles in different azimuthal bins from the set of events. In this analysis, Mixed events are created by randomly selecting the number of particles in different azimuthal bins. We have the information about the number of particles in six different azimuthal bins in each event. Consider N_1, N_2, N_3, N_4, N_5, N_6 as the number of particles in six different azimuthal bins in event 1, respectively. To create a mixed event dataset, N_1 is replaced by the number of particles in the same azimuthal bin from five different events. Therefore for each event set containing six different azimuthal bins, six different mixed event datasets are created. Each mixed event dataset has six times the number of events than the original dataset, but all intra-event correlations between different azimuthal bins are removed. The goal of creating mixed events is to eliminate event-by-event effects (clustering) while capturing the global effects (detector efficiency).

3.5 Central Moments

The analysis is based on the event-by-event measurement of the number of Kaons followed by the event-by-event calculations of the observables for clustering described in the last section. Our main interest lies in the calculation of central moments of the distributions of probability of event clustering and pull distributions. In this section, we describe the central moments calculations.

In mathematical statistics, a random variable x is characterised by certain probability density functions (*pdf*), $f(x)$. All characteristic properties of these *pdf* are conveyed in terms of the expectation values, $E[g(x)]$, as follows

$$E[g(x)] = \int g(x)f(x)dx \tag{3.11}$$

where $g(x)$ represents any function of the random variable x and integration is over all values of x, provided the function is integrable under certain limits. The n^{th} order moment of the *pdf* is defined as

$$\mu_n = E[x^n] = \int x^n f(x)dx \tag{3.12}$$

The first order moment is commonly known as mean, μ_1 or only μ. The n^{th} order central moment is defined as,

$$\nu_n = E[(x-\mu)^n] = \int (x-\mu)^n f(x)dx \tag{3.13}$$

Here the term central is due to the integration of the function $g(x)$ around its mean value μ. Central moment is a moment of a probability distribution of a random variable about the random variable's mean. This implies that the 1^{st} order central moment is simply zero as $\int (x-\mu) f(x) dx = \int x f(x) dx - \mu \int f(x) dx = \mu - (\mu \times 1) = 0$. The 2^{nd}, 3^{rd}, and 4^{th} order central moments are defined as,

$$\nu_2 = \int (x-\mu)^2 f(x) dx, \tag{3.14}$$

$$\nu_3 = \int (x-\mu)^3 f(x) dx, \tag{3.15}$$

$$\nu_4 = \int (x-\mu)^4 f(x) dx \tag{3.16}$$

Fig. 3.3 shows the mean and variance of the distribution.

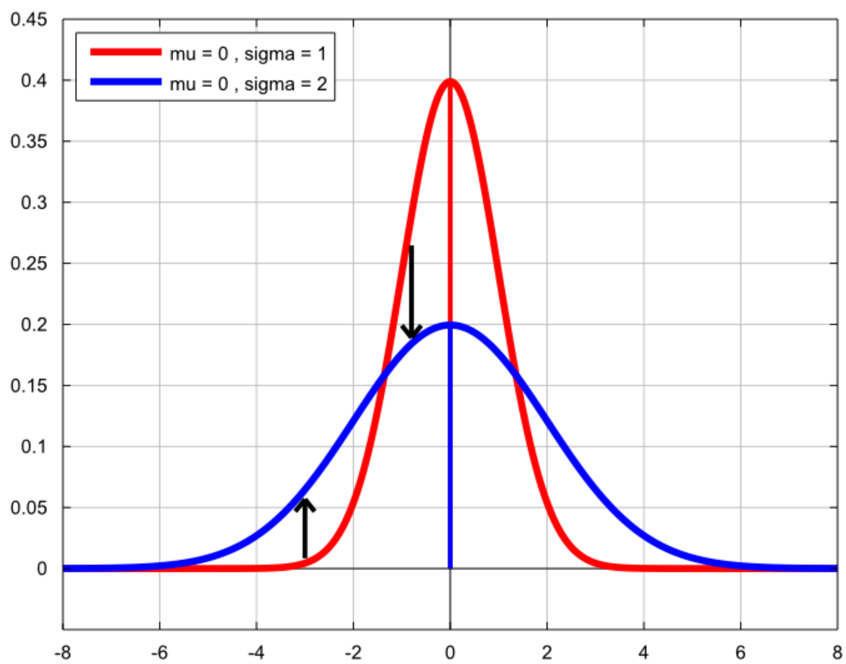

Figure 3.3: Mean and variance of a distribution.

The 2^{nd} order central moment is known as variance, σ^2. It is expressed as follows

$$\sigma^2 = \nu_2 = \mu_2 - \mu^2 \tag{3.17}$$

Similarly, the 3^{rd} central moment can be derived in terms of n^{th} order moments as follows,

$$\begin{aligned} \nu_3 &= E(x-\mu)^3, \\ &= E[x^3 - 3\mu x^2 + 3\mu^2 x - \mu^3], \\ &= \mu_3 - 3\mu\mu_2 + 3\mu^3 - \mu^3, \\ &= \mu_3 - 3\mu\mu_2 + 2\mu^3 \end{aligned} \tag{3.18}$$

These central moments play a significant role in understanding the shape of a *pdf*. The skewness, S, of a *pdf* is defined as,

$$S = \frac{\nu_3}{\nu_2^{3/2}} = \frac{\nu_3}{\sigma^{3/2}} \tag{3.19}$$

The positive and negative values of the skewness qualitatively show the distribution of the random variable x skewed towards right and left of the mean of the distribution as shown in Fig. 3.4. More generally, skewness represents the asymmetry of the distribution.

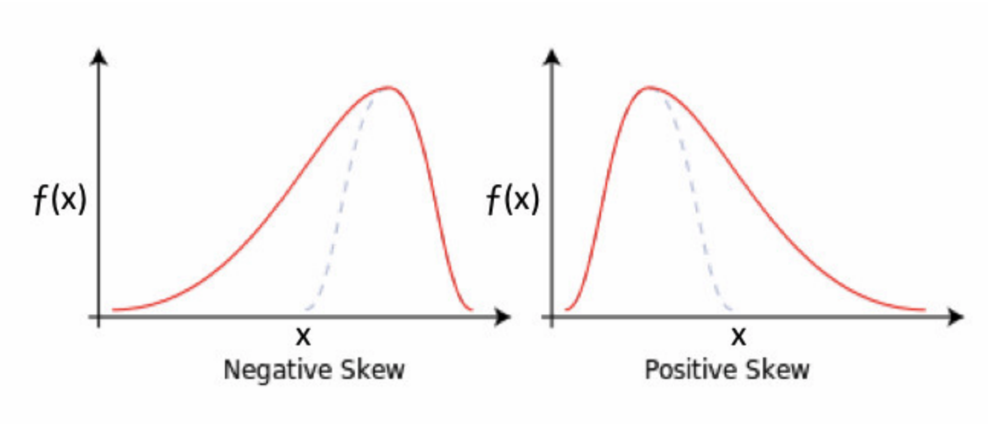

Figure 3.4: Skewness of a distribution.

Similarly, the kurtosis, κ, is associated with the 4^{th} and 2^{nd} order central moments of a *pdf* as follows,

$$\kappa = \frac{\nu_4}{\nu_2^2} = \frac{\nu_4}{\sigma^4} \tag{3.20}$$

The kurtosis of the normal distribution is equal to 3. So, to normalize the kurtosis with respect to a normal or Gaussian distribution, 3 is subtracted and the final expression for the kurtosis is,

$$\kappa = \frac{\nu_4}{\sigma^4} - 3 \tag{3.21}$$

The kurtosis represents the peakedness and the tailedness of the distribution as shown in Fig. 3.5. In this figure, each distribution represents different kurtosis values.

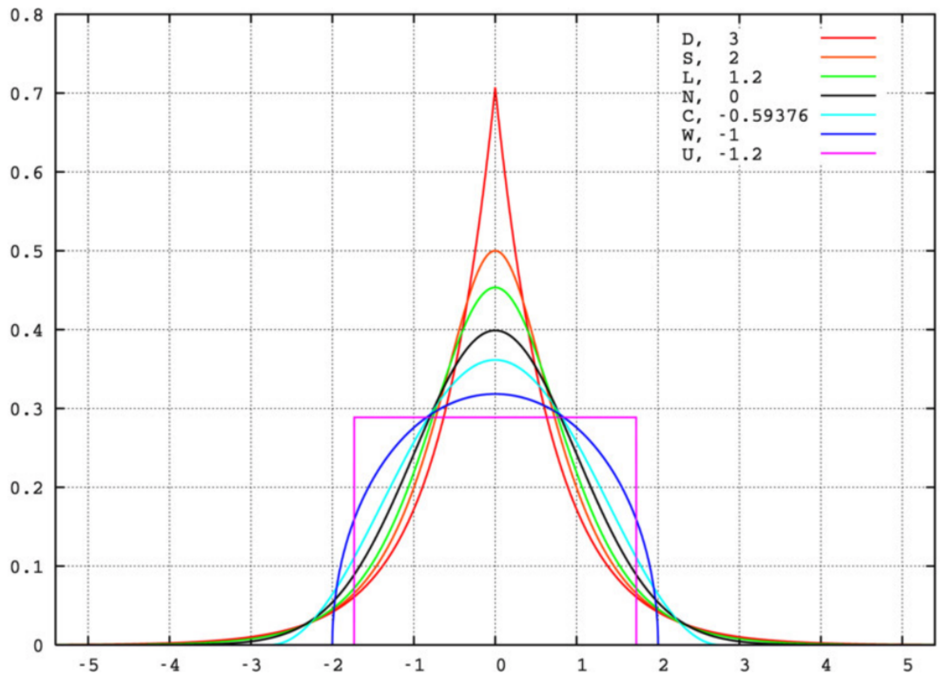

Figure 3.5: Kurtosis of a distribution.

Using the above definition for variance, skewness and kurtosis, in this analysis, the central moments for our observables are calculated. The results are presented as a function of mean numbers of particles generated per event.

3.6 Importance of Event-by-Event Fluctuation Studies

Our analysis is based on the event-by-event measurement of the particle number in different azimuthal bins. We arrive at physics conclusions based on the distributions of the data collected and by comparing how those distributions are deviating from the baseline results.

The importance of event-by-event physics is evident from the following simple analogy [59]. Suppose, we stick a sheet of paper outside on a rainy day. Keeping it outside for a long time, the paper will become uniformly wet and one would conclude that rain is a uniform mist. If, however, one keeps a paper outside for a few seconds only, one will be able to observe the striking droplet structure of rain. The statistics about droplet sizes will be able to give us information about phenomena like fragmentation, surface tension, etc. Analysing many events gives good statistics and may also reveal rare events like snow or hail. If we can vary the initial conditions like timing and orientation of paper, we can also calculate the speed and direction of the rain drops.

We are using a similar analogy for this analysis. Our analysis is based on calculating the number of particles on an event-by-event basis. Now, a phenomenon like clustering may happen in some events but not all. To identify the clustering event, we calculate the central moments for our observables. We then look for the fluctuation in the value of central moments with respect to the baseline.

3.7 Sensitivity of the Observables

To check our observables sensitivity, we make use of the generated sets of particles we get from the MC HIJING events (described in Chapter 4). Here we analyse 2×10^5 events per centrality bin, assuming that the generated MC HIJING event does not contain any clustering information. Clustering is implemented by assigning a certain percentage of total particles in one azimuthal bin keeping the rest of the bin unchanged. If N_1 is the number of particles in one azimuthal bin in an event, then we increase the particle number by 5%, 10%, 20%, 30%, 40%, and 50% of N_1, respectively, keeping the number of particles in all other bins unchanged. We have calculated the central moment values for our observable for different percentages of clustering.

The effect of different percentages of clustering on the central moments of the distribution of $P(E)$ is shown in Fig. 3.6, Fig. 3.8, and Fig. 3.10.

We observe that we do not see much effect when the clustering percentage is low. However, we do see some effect, in particular on higher moments, as the percentage of cluster

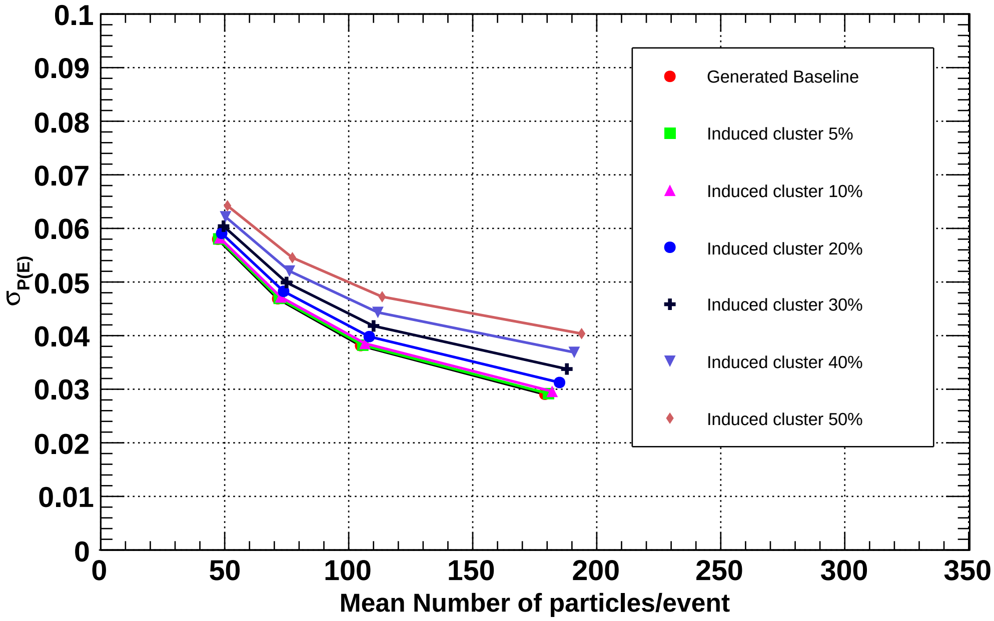

Figure 3.6: Effect of clustering on $\sigma_{P(E)}$.

increases. Further, we also calculated the relative increase in the value of central moments with clustering percentages for the most central bin, in order to gauge which analysis hold the most promise if the clustering probability exceeds a certain value. The relative increase is given by

$$Relative\ increase = \frac{N - O}{O} \tag{3.22}$$

where N and O are neighboring clustering probability values according to Fig. 3.6, 3.8, and 3.10. Fig. 3.7, 3.9, and 3.11 show the relative increase for different percentages of clustering for the most central collisions. Comparing the relative increase in the most central collision for $\sigma_{P(E)}$, $S_{P(E)}$, and $\kappa_{P(E)}$, we observe that the peak relative increase in the sensitivity of the observable increases roughly by an order of magnitude when we move from $\sigma_{P(E)}$ to the higher moments, $S_{P(E)}$ and $\kappa_{P(E)}$. For the higher moments, the 20% clustering mark seems

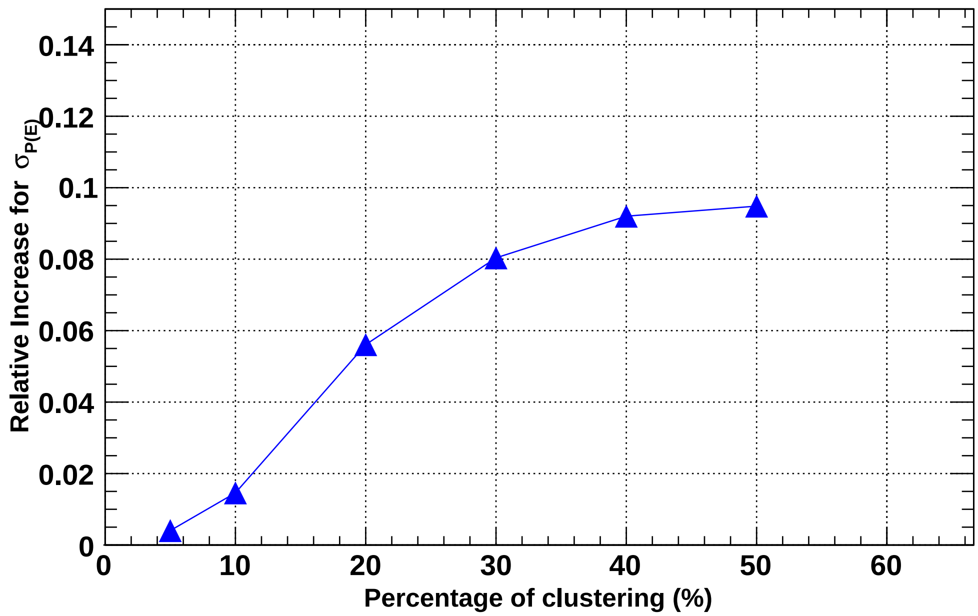

Figure 3.7: Relative increase in the value of $\sigma_{P(E)}$ due to the effect of clustering for the most central bin.

to be a sweet spot, which indicates that the low statistics per azimuthal bin is overcome when one reaches at least 20% clustering. The additional gain beyond that level is moderate.

The effect of different percentages of clustering on the central moments of the Pull distribution is calculated and shown in Fig. 3.12, 3.14, and 3.16. The relative increase plots for respective moments are shown in Fig. 3.13, 3.15, and 3.17 respectively. The σ_{Pull} show the biggest effect for central collisions i.e. the highest mean number of particles per event. The observable sensitivity increases with the higher moment values of the distributions. This is also evident from the relative increase plots as we can see that the relative increase value for S_{Pull}, and κ_{Pull} is an order of magnitude larger than that of σ_{Pull}. The relative increase plots for Pull distribution shows similar behavior as that for $P(E)$ distribution. These sensitivity plots are used to compare results from our corrected data in Chapter 5.

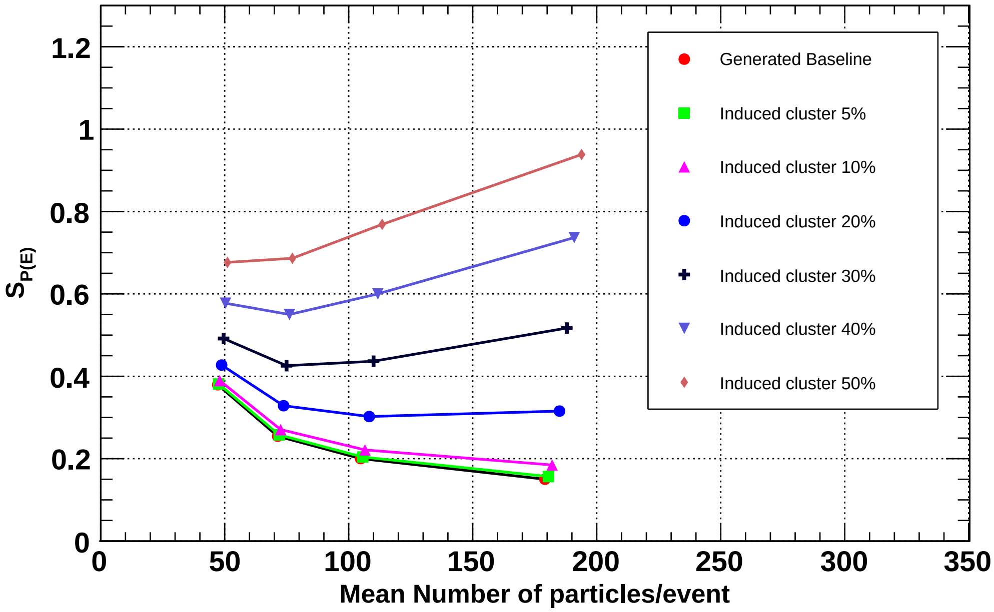

Figure 3.8: Effect of clustering on $S_{P(E)}$.

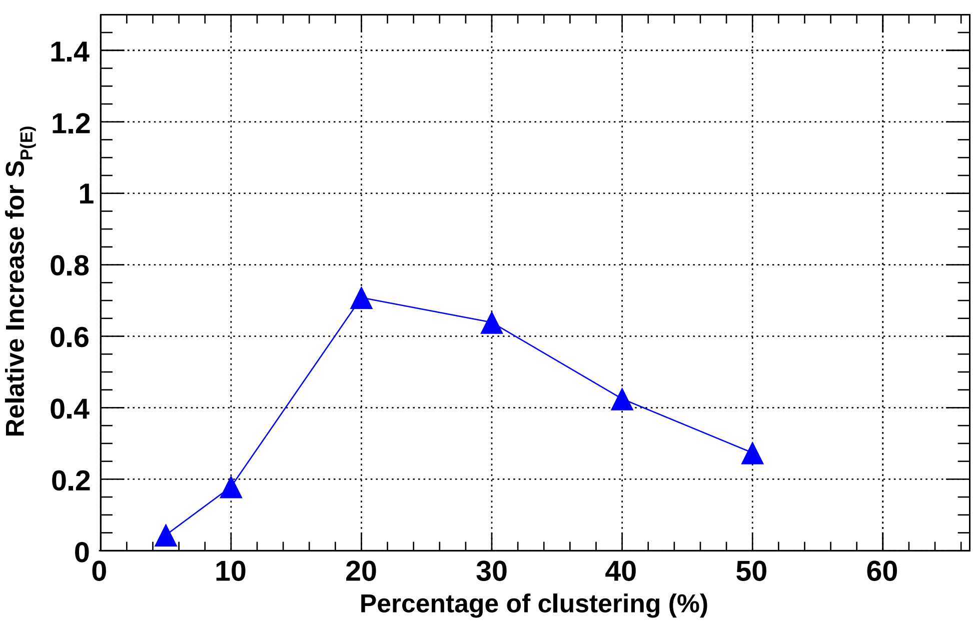

Figure 3.9: Relative increase in the value of $S_{P(E)}$ due to the effect of clustering for the most central bin.

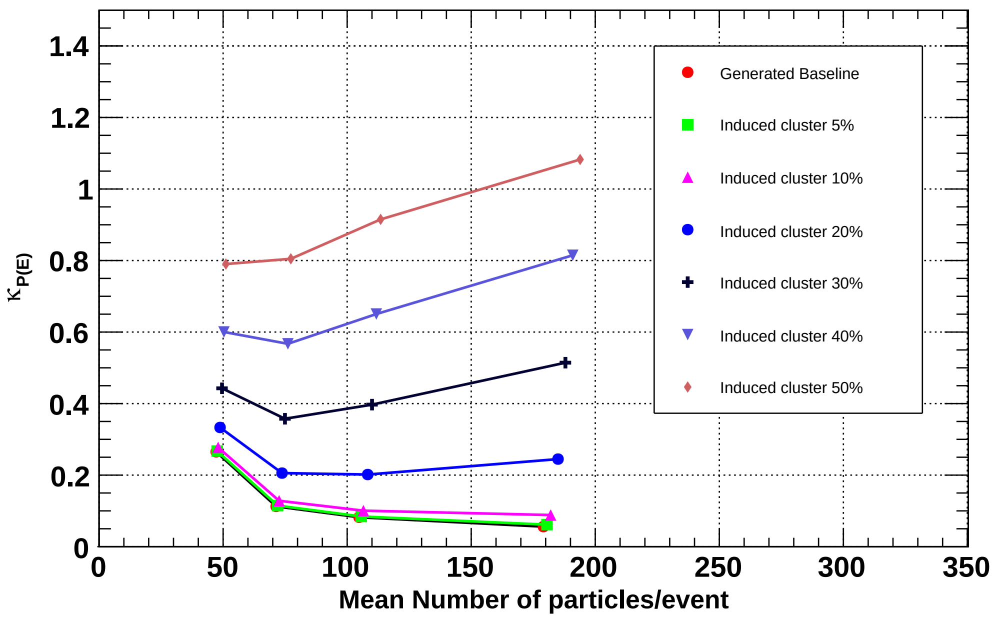

Figure 3.10: Effect of clustering on $\kappa_{P(E)}$.

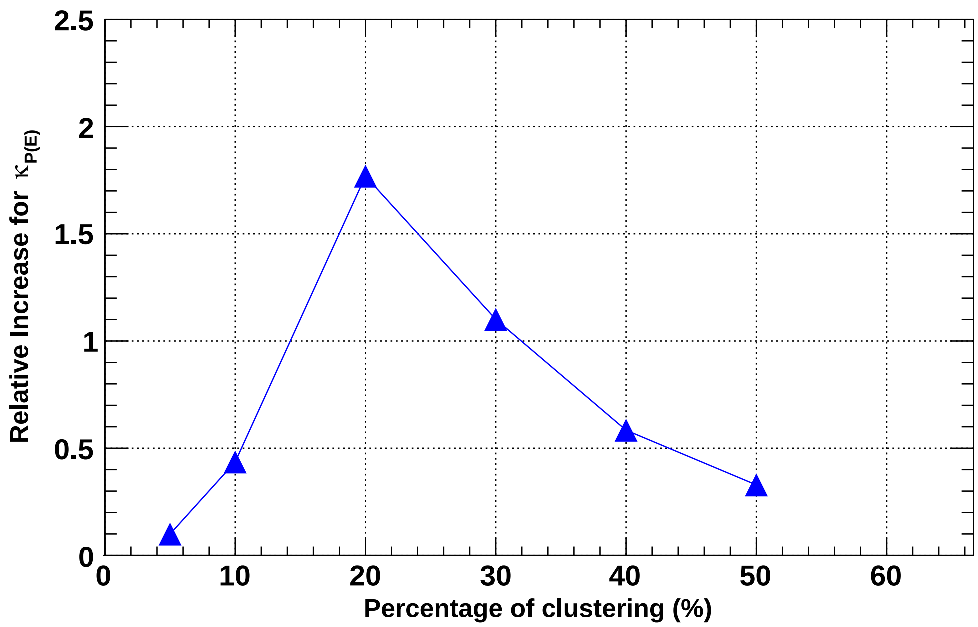

Figure 3.11: Relative increase in the value of $\kappa_{P(E)}$ due to the effect of clustering for the most central bin.

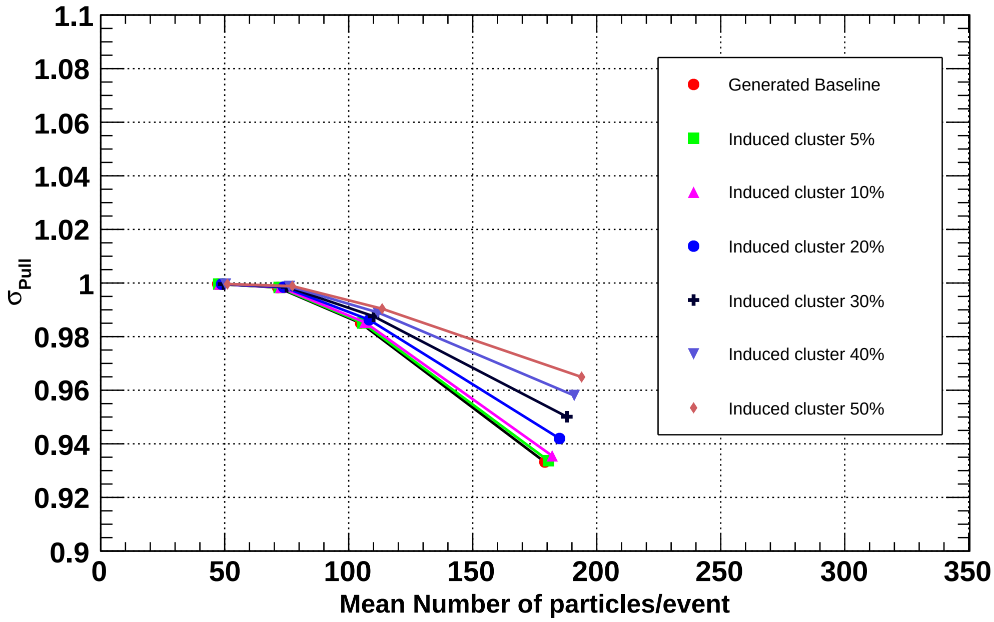

Figure 3.12: Effect of clustering on σ_{Pull}.

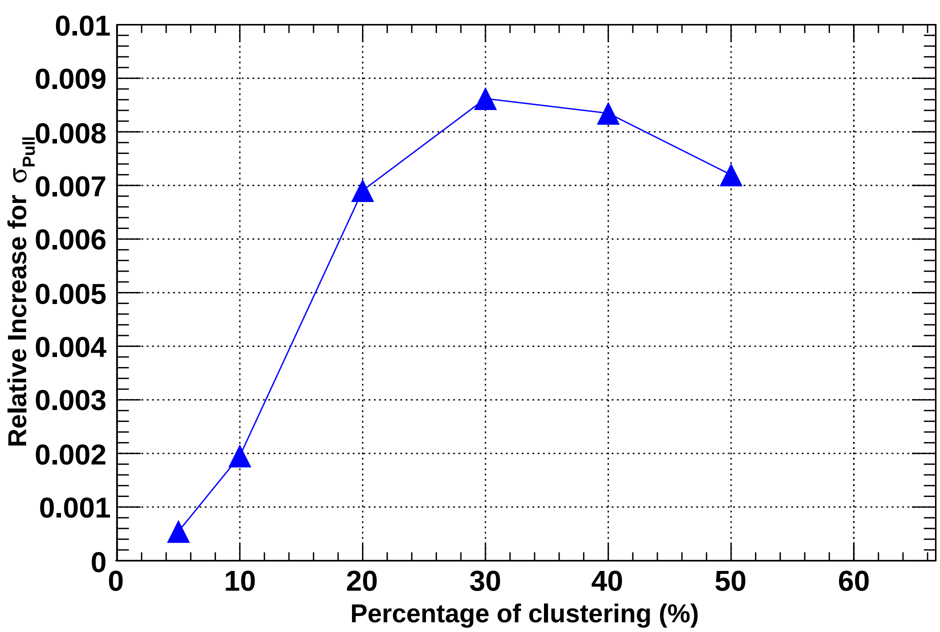

Figure 3.13: Relative increase in the value of σ_{Pull} due to the effect of clustering for the most central bin.

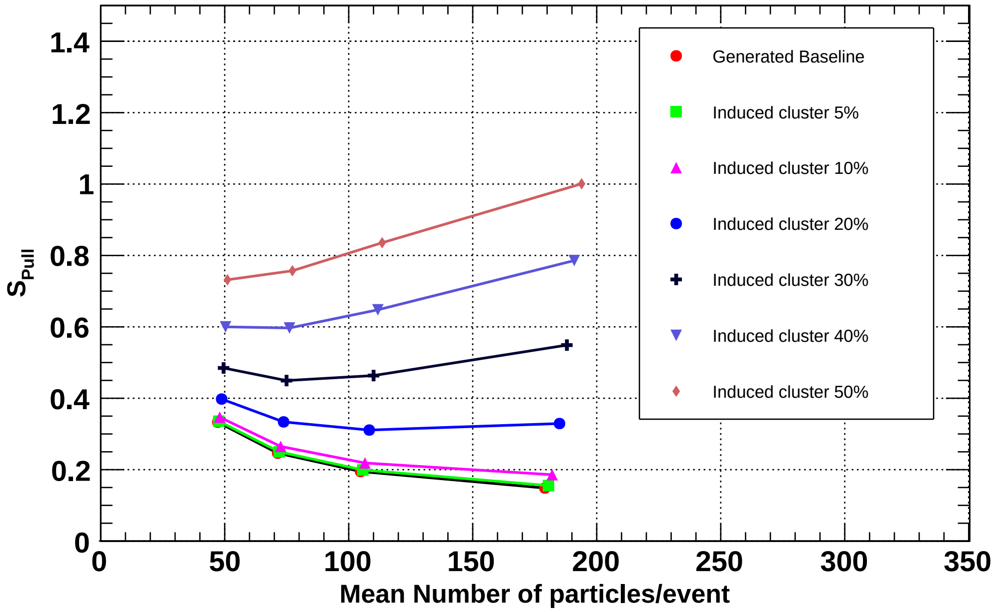

Figure 3.14: Effect of clustering on S_{Pull}.

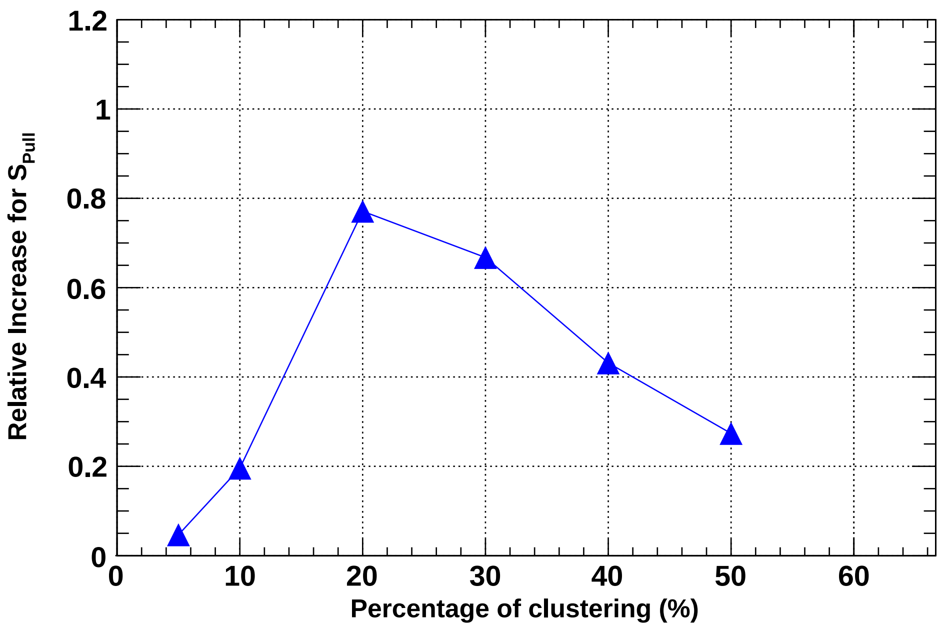

Figure 3.15: Relative increase in the value of S_{Pull} due to the effect of clustering for the most central bin.

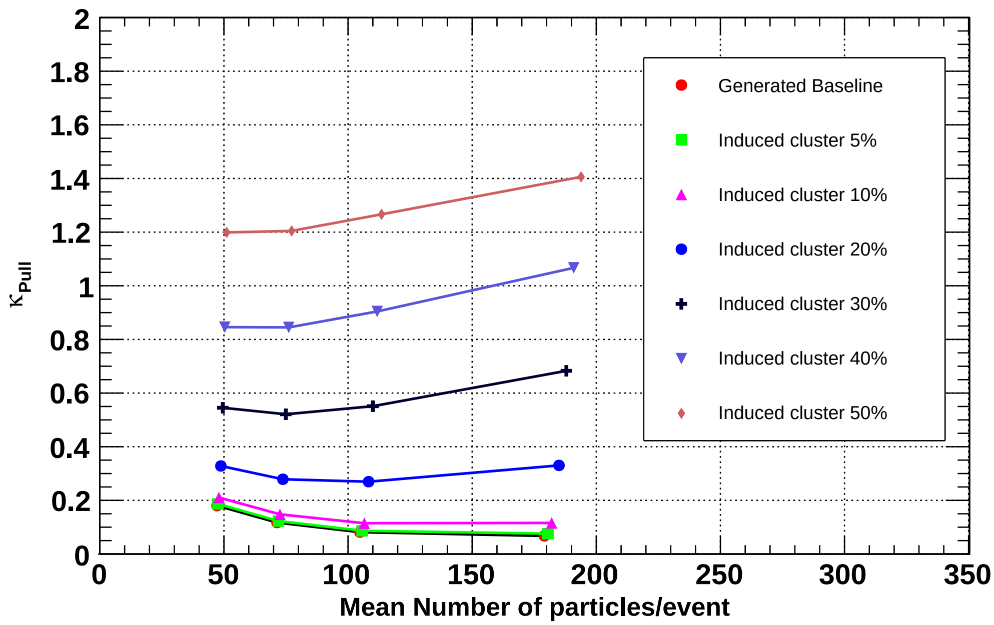

Figure 3.16: Effect of clustering on κ_{Pull}.

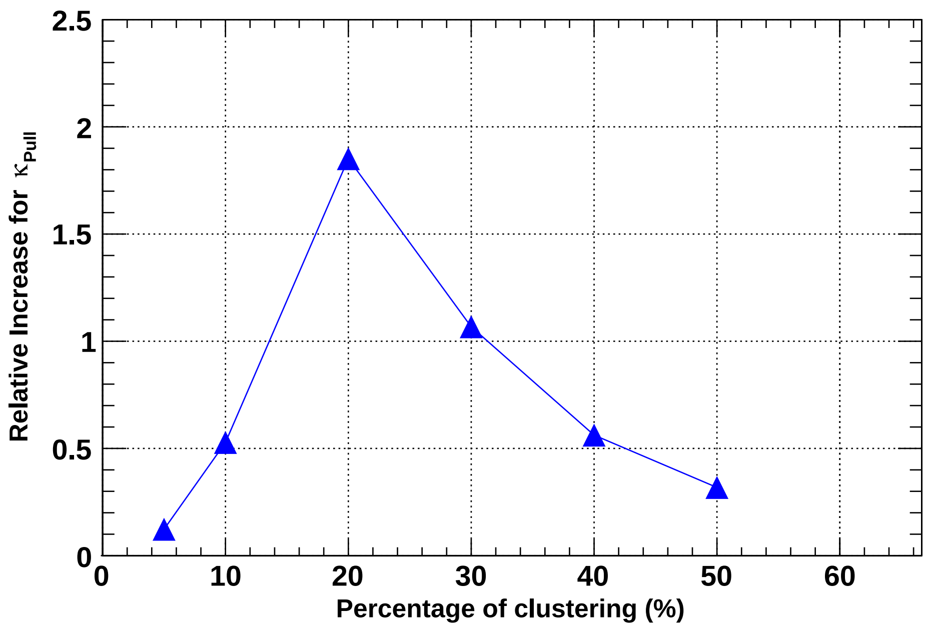

Figure 3.17: Relative increase in the value of κ_{Pull} due to the effect of clustering for the most central bin.

Chapter 4

Analysis Method

In this chapter, we describe the different analysis techniques employed before arriving at the results. They include correcting the data sample for mis-identification, efficiency losses, closure test, and error estimations (both statistical and systematic).

4.1 Data and Event Selection

The analysis is based on the Pb-Pb collision data collected in 2015 at $\sqrt{s_{NN}} = 5.02$ TeV using the ALICE detector at the LHC. To select an event, the minimum bias trigger selection cut is used, which requires minimal event activity in the VZERO detectors. Then to avoid background events and secondary interactions, a primary vertex, V_z, cut of less than 10 cm in z-direction of the centre of the ITS/TPC (centre of the detector) is imposed. This is to make sure that the collision did occur in the centre of the detector, and not outside the expected region of collision. When multiple events occur in the TPC during the drift time of the electrons released by the tracks emitted from a single Pb-Pb collision, so-called pileup is recorded,which leads to an over abundance of false tracks event-by-event. The pileup events are removed using ALICE's default framework, which is based on enhanced primary vertex cuts in space and time for the event in question. For centrality determination, VZERO multiplicity selection is used. VZERO estimator is based on the sum of amplitudes from the VZERO-A and VZERO-C. The centrality classes used for this analysis are: [0-10], [10-20], [20-30], [30-40]. We analyse 8×10^6 events for four centrality classes. Fig. 4.1 depicts the effect of pile-up cuts on V_z.

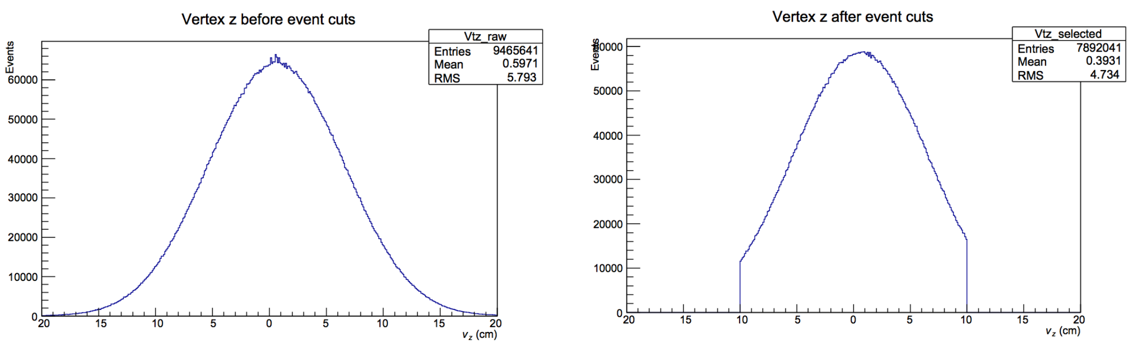

Figure 4.1: V_z position before (left) and after (right) the pile-up cut.

4.2 Track Selections

After the event selection, the next step is to select the good tracks by rejecting the fake tracks. So-called hybrid tracks, containing combined information from trajectories in the ITS and TPC detectors, are used in order to ensure a uniform distribution in the (η, ϕ) plane. Hybrid tracks have some predefined cuts for applying ITS refit for track reconstruction. The p_T cuts used for track selection are $0.4 < p_T < 1.5$ GeV/c in the pseudorapidity range of $-0.8 < \eta < 0.8$. An explanations of the various selections in Table 4.1, is as follows:

- **TPC dE/dx:** The energy loss measurement from the TPC, with $n\sigma < 2$, is used to identify charged tracks. It is discussed further in the next section.

- $\boldsymbol{DCA_z}$**:** DCA_z is the distance of closest approach to the primary vertex. In our analysis, tracks with DCA_z cuts of 2.0 cm are applied in the z direction to ensure that the tracks are from primary vertex.

- ***TPC*** $\boldsymbol{N_{crossedrows}}$: The tracks were required to have at least 80 reconstructed points out of the maximum 160 in the TPC. Tracks with smaller number of space points may result from split tracks i.e. one charge particle was reconstructed as two tracks.

Table 4.1: A summary of track selection for K^+ and K^-.

Default Track Selection	K^+ and K^-
Vertex	$\|V_z\| < 10cm$
Centrality Estimator	V0M
TPC dE/dx Selection	$\|n\sigma\| < 2$
Pseudorapidity (η)	$\|\eta\| < 0.8$
TPC $N_{crossedrows}$	> 80
DCA_z	$< 2.cm$

4.3 Particle Identification

The main objective of this analysis is to obtain the number of charged kaons ($K^{\pm}$) for each centrality, for each azimuthal bin. The $K^{\pm}$ are selected on the basis of TPC information. The particle identification in TPC is based on the measurement of specific energy loss of the particle in the TPC volume.

From Fig. 4.2, it can be observed that the kaons are contaminated by other mis-identified tracks (i.e. protons and pions). The increase in the track momentum increases the contamination of kaon tracks by pions. A high efficiency kaon sample can be obtained by applying $|n\sigma|$ cuts. This is defined as the deviation of measured energy loss to the expected energy loss of a particle species given by

$$n\sigma_{TPC} = \frac{\left|\frac{dE}{dX}\right|_{measured} - \left|\frac{dE}{dX}\right|_{expected}}{\sigma\left(\frac{dE}{dX}\right)} \tag{4.1}$$

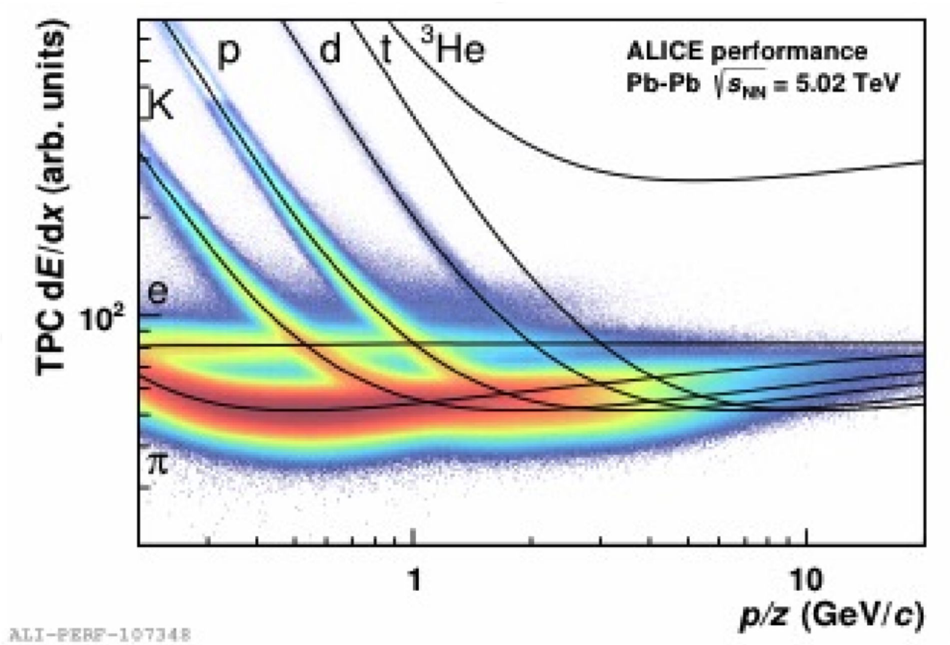

Figure 4.2: The specific energy loss (dE/dX) of tracks as a function of track momentum in Pb-Pb collisions at $\sqrt{s_{NN}} = 5.02$ TeV, as measured by ALICE TPC.

where, $\sigma\left(\frac{dE}{dX}\right)$ is the dE/dX resolution of the TPC detector. $\left|\frac{dE}{dX}\right|_{measured}$ is the energy loss measured in the TPC and $\left|\frac{dE}{dX}\right|_{expected}$ is the energy loss calculated from the Bethe-Bloch equation for a particular particle species [51]. The Bethe-Bloch equation is described in detail in section 2.5 of Chapter 2. The specific energy loss of tracks are obtained as a function of track momentum after applying $|n\sigma|$ cuts.

4.4 Error Estimation

Each experimental measurement is associated with two types of uncertainties: statistical and systematic.

4.4.1 Determination of Statistical Uncertainty

The measurement uncertainties need to be well understood in order to obtain the significance of any results potentially showing the clustering. Some of the known methods of statistical error estimations are discussed below.

Subgroup Method

In the Subgroup method, the whole data sample is divided into a number of sub-samples, k. For each sub-sample, the moments are estimated. Let M_n^i be the n^{th} moment of i^{th} sub-sample. The final value of n^{th} moment (M_n) and its statistical error (δM_n) are estimated as follows,

$$M_n = \frac{\sum_{i=1}^{k} M_n^i}{k} \tag{4.2}$$

$$\sigma M_n = \sqrt{\frac{\sum_{i=1}^{k}(M_n^i - M_n)^2}{k-1}} \tag{4.3}$$

$$\delta M_n = \frac{\sigma M_n}{\sqrt{k}} \tag{4.4}$$

For higher moment analysis, generally, 30 sub-samples are taken for statistical error estimation.

Bootstrap Method

In the bootstrap method, unlike the subgroup method, instead of dividing the parent sample, there will be k number of clone samples created by random selection from the parent sample with same statistics [60]. Moments for each sample were calculated and k values of particular moments will be obtained. The errors of the corresponding moments are obtained by taking the root mean square of those values. This method is computationally expensive.

Delta Theorem Method

The delta theorem approach [61] was chosen as the estimator of the uncertainty of the statistical moments for this analysis. It is based on the delta theorem in statistics that allows the approximation of the distribution of a transformation. It is described below.

Considering a deviation as an event-by-event quantity defined using the value, N, and the average value, $< N >$, over the whole sample,

$$\delta N = N - < N >, \tag{4.5}$$

the central moment, ν_n, of order n is defined using the deviation as

$$\nu_n =< (\delta N)^n >=< (N- < N >)^n > \tag{4.6}$$

The normalized central moment of the order n, x_n, is the central moment, ν_n, divided by the standard deviation, σ, to the power of n,

$$x_n = \nu_n / \sigma^n \tag{4.7}$$

The uncertainty expressions for the individual moments from the Delta Theorem are then given by,

$$Var(\sigma) = (x_4 - 1)\sigma^2/(4n) \tag{4.8}$$

$$Var(S) = [9 - 6x_4 + x_3^3(35 + 9x_4)/4 - 3x_3x_5 + x_6]/n \tag{4.9}$$

$$Var(\kappa) = [4x_4^3 - x_4^2 + 16x_3^2(1 + x_4) - 8x_3x_5 - 4x_4x_6 + x_8]/n \tag{4.10}$$

The analysis is based on the distribution of the number of particles in different azimuthal bins for different events. Hence, we will be calculating two distinct statistical errors. One arises due to the variation in the number of particles in different azimuthal bins. Another one arises due to the variation of the mean number of particles event-by-event, the former being particle based, whereas the latter being the event based contribution to the statistical error. Let $\sigma_{azimuthal}$ be the uncertainty arising due to the variation in the azimuthal bin and σ_{events}, the uncertainty due to the variation of the mean number of particles event-by-event. The total statistical uncertainty is calculated as

$$\sigma_{total} = \sqrt{\sigma^2_{azimuthal} + \sigma^2_{events}} \tag{4.11}$$

4.4.2 Determination of Systematic Uncertainties

There can be systematic uncertainty due to variation in event selection, track selection and experimental procedures. The analysis procedure is performed with the identified systematic sources and the uncertainty is evaluated after comparing to the default measurement. The default values are the set of the selection parameters used for the baseline measurement. A set of systematic sources are identified and the observable values are obtained by varying those sources. The different contributions to the systematic uncertainties that were studied are described below. The deviation from the default value represents the RMS caused by the selection variable. The RMS is calculated as

$$RMS = \sqrt{\frac{1}{N}\sum_{i=1}^{N}(X_i - Y)^2} \tag{4.12}$$

where, N is the total number of variations, Y is the default value, and X_i are the different cut variations. For the total systematic uncertainty, all maximum deviations are combined in quadrature . It is calculated as

$$SYS_{err} = \sqrt{\sum_j RMS_j^2} \tag{4.13}$$

where, j is the number of systematic uncertainty sources.

Various sources of systematic uncertainties, namely, the contribution from PID, and Track and event selection are studied, which are listed in Table 4.2.

Table 4.2: Default cuts variation.

Track cut	Default value	Lower value	Higher value
Min Number of $TPC\ N_{crossedrows}$	80	60	100
Minimum ratio crossed rows over findable TPC clusters	0.8	0.7	0.9
Max. ^{2} per cluster in TPC	4	3	5
DCA_{xy}	7σ	4σ	10σ
DCA_z	2	1	5
$n\sigma_{TPC}$	2	1	3

A summary of different systematic uncertainties for Kaons in shown in Fig. 4.3. It can be seen that the maximum contribution to the systematic error comes from PID. Hence, in this analysis, for systematic check, the $n\sigma$ cuts are varied up (tight) as $|n\sigma| < 1$ and down (loose) as $|n\sigma| < 3$, with respect to the default cuts, $|n\sigma| < 2$.

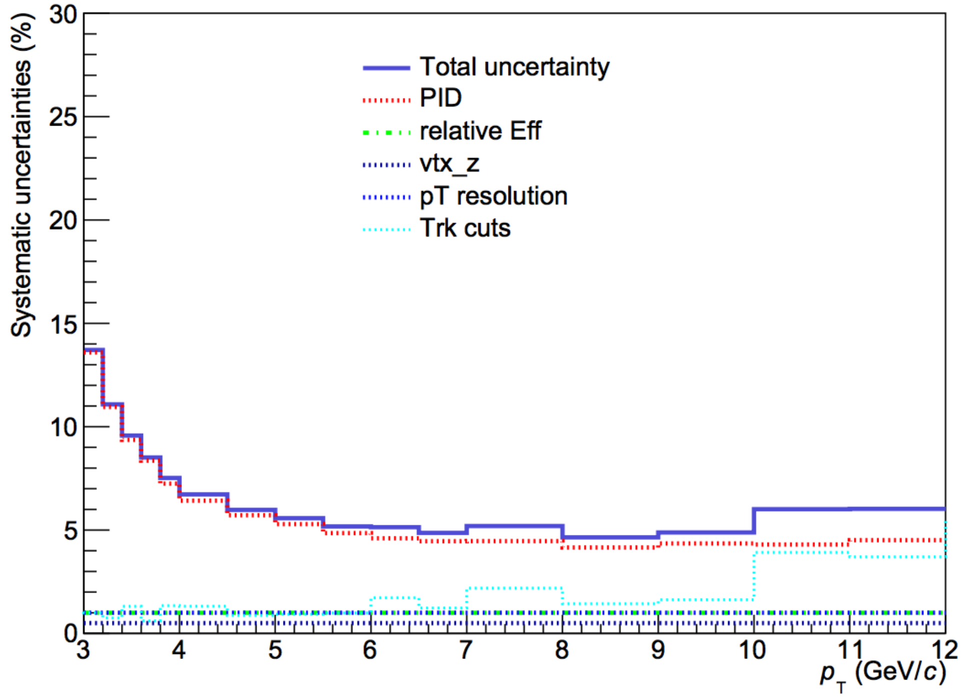

Figure 4.3: Summary of systematic uncertainties for Kaons as a function of transverse momentum.

Table 4.3 shows the relative uncertainties on the moments of the observables due to different $n\sigma$ cuts.

Table 4.3: Relative uncertainties on the moments of the observables due to different $n\sigma$ cuts. Results are for $0 - 10\%$ centrality class.

Observable	Loose cut ($n\sigma < 3$)	Tight cut ($n\sigma < 1$)
$\sigma_{P(E)}$	0.10	0.21
$\mathrm{S}_{P(E)}$	0.28	0.31
$\kappa_{P(E)}$	0.36	0.64
σ_{Pull}	0.012	0.022
S_{Pull}	0.27	0.33
κ_{Pull}	0.36	0.29

To get the sense of magnitude of the derived uncertainties, the respective plots can be seen in Fig. 4.4.

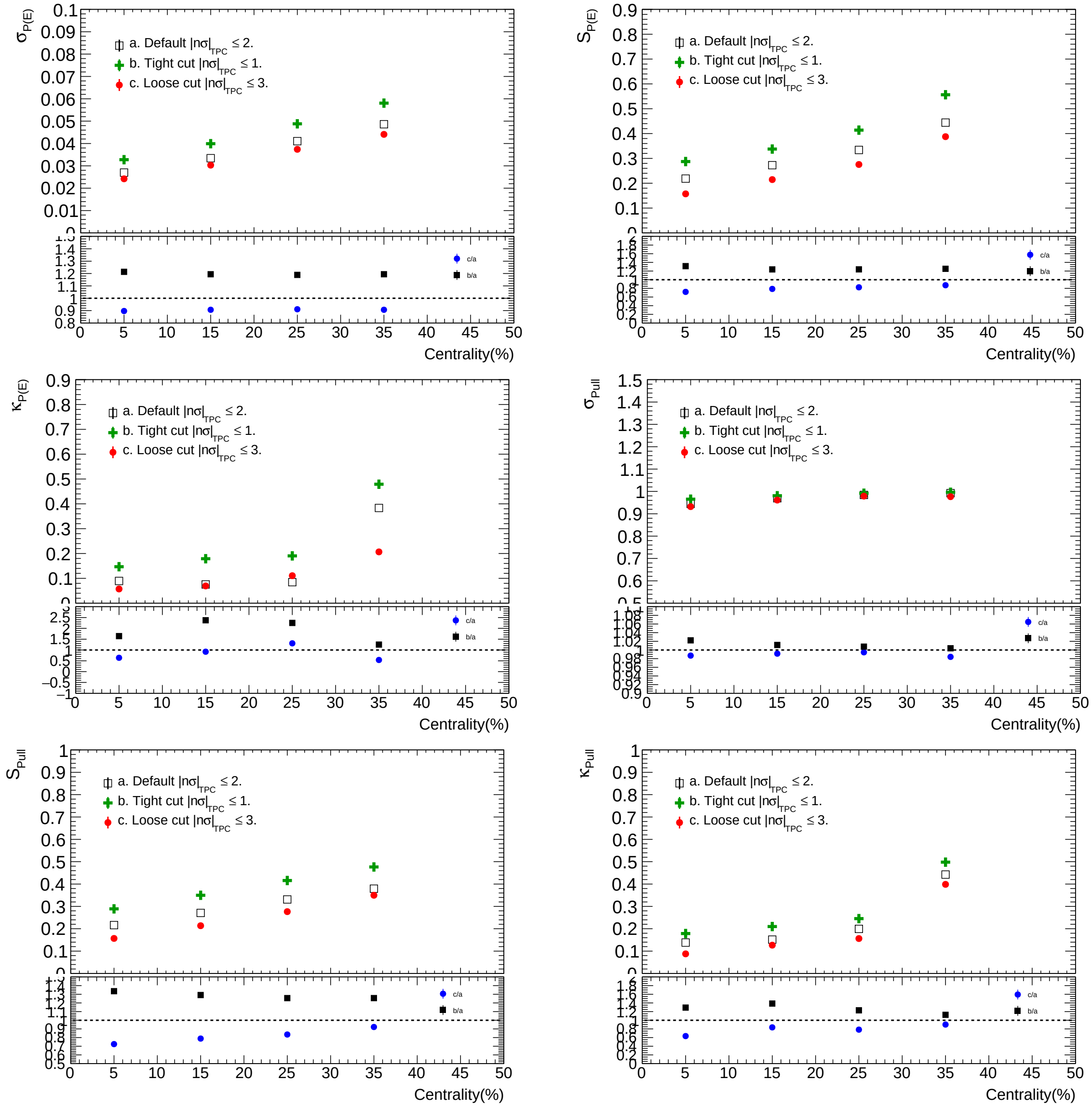

Figure 4.4: Plots of $\sigma_{P(E)}$, $S_{P(E)}$, $\kappa_{P(E)}$, σ_{Pull}, S_{Pull}, κ_{Pull} based on $n\sigma$ cut variation and their comparison to the default value in the lower panel.

These calculated systematic uncertainties, together with the aforementioned statistical error from the delta theorem method, allow us to present our final corrected result in the following chapter.

4.5 Simulation Studies

In heavy ion collision experiments, the collected dataset has limited statistics. In addition, the detectors involved in the data collecting have limited efficiency. That is why we need to have a complete idea of detector efficiencies and how to do the correction for the detector effects. This is addressed through the GEANT MC study.

GEANT is a detector response program developed by our community, which allows the computational definition of the geometry of each detector component and its respective basic detector responses e.g. scattering, energy loss, and extra particle emission. In ALICE, depending on the physics demand, various event generators are used for Monte Carlo (MC) study. For this analysis, HIJING [62] events are used for MC study.

HIJING is a realistic event generator, which generates a complete set of produced particles at the primary vertex including their dynamic properties, such as energy and momentum. HIJING is based on a superposition of elementary parton-parton scattering processes and subsequent fragmentation for particle production. The resulting set of elementary particles can then be propagated through the simulated detector layout via the GEANT packages. The number of HIJING events we analyse is 8×10^5 for the Pb-Pb collision data at $\sqrt{s_{NN}} = 5.02$ TeV.

4.5.1 Detector Efficiency and Contamination

MC HIJING events are used to estimate the efficiency and contamination. The efficiency of the detector is calculated by taking the ratio of the total number of reconstructed primary tracks to the total number of generated primary tracks of Kaons.

$$Efficiency(\epsilon) \ = \frac{N_{rec,primary}}{N_{generated}} \tag{4.14}$$

We are using TPC detector for particle identification. Therefore, the contamination while detecting kaons may come from the secondary kaons ($N_{secondary}$) and from the mis-identification ($N_{mis-identification}$) of pions and electrons. Secondary kaons are actual kaons but are mis-identified as primary kaons although they come from the decay of weak decay particles. For example, $\Omega^- \rightarrow K^- + \Lambda^0$, $\phi \rightarrow K^+ + K^-$ are some decay channels producing secondary kaons.

$$N_{cont} = N_{secondary} + N_{mis-identification} \tag{4.15}$$

The total contamination fraction is defined as,

$$Contamination(\delta) \ = \frac{N_{cont}}{N_{rec}} \tag{4.16}$$

Fig. 4.5 shows the efficiency and contamination plots for Kaons for the most central event. The plots correspond to one typical azimuthal bin.

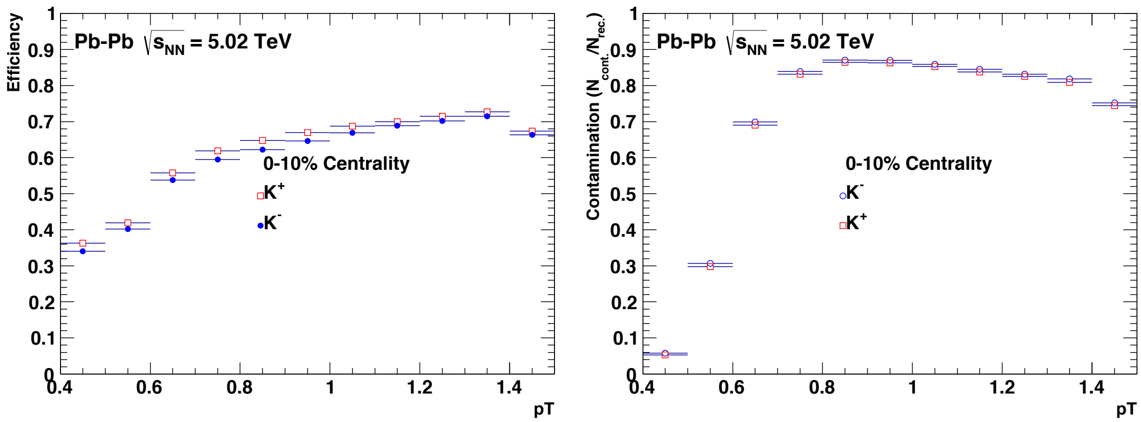

Figure 4.5: Efficiency (left) and Contamination (right) of K^+ and K^- shown as a function of p_T for $(0-10)\%$ centrality obtained using HIJING MC events at 5.02 TeV for one azimuthal bin.

An estimate of $N_{secondary}$ and $N_{mis-identification}$ is shown in Fig. 4.6. We can see there is around 90% contamination for the identification of Kaons. The main source of this contamination are mis-identification. While correcting for the number of particles we treat these mis-identification as a background and subtract it to get the correct number of particles. The correcting rule is described in the next section.

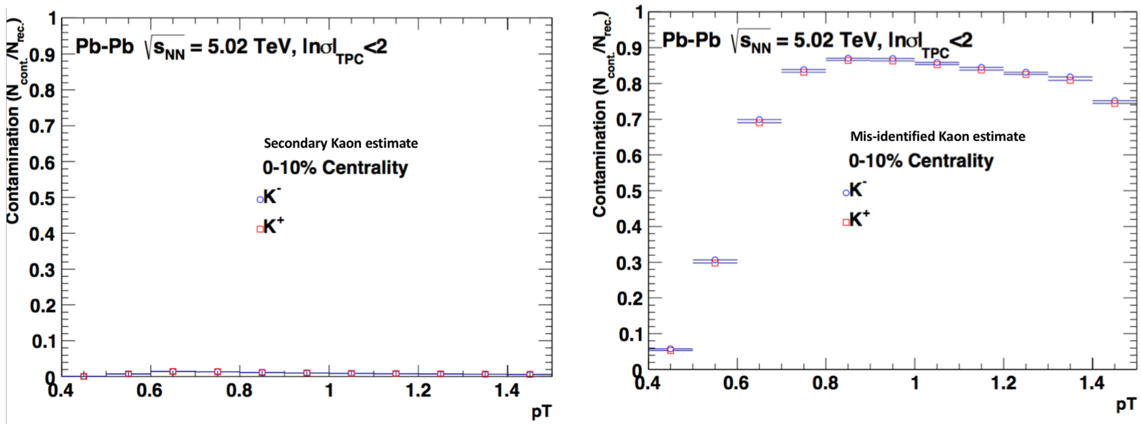

Figure 4.6: An estimate of the secondary (left) and mis-identified (right) kaons on the total contamination for K^+ and K^- shown as a function of p_T for $(0-10)\%$ centrality obtained using HIJING MC events at 5.02 TeV for one azimuthal bin.

4.5.2 MC Closure Tests

To validate the analysis method and particularly the effect of obtained efficiency, and contamination factors, so-called MC closure tests are performed based on the HIJING input.

The numbers of generated primary tracks/particles can be estimated from the reconstructed tracks as follows.

We know, $N_{rec} = N_{rec,primary} + N_{cont}$

Conversely,

$$N_{rec,primary} = N_{rec} - N_{cont} \tag{4.17}$$

As previously defined, efficiency $(\epsilon) = \frac{N_{rec,primary}}{N_{generated}}$. That implies, $\epsilon N_{generated} = N_{rec,primary}$.

And $\delta = \frac{N_{cont}}{N_{rec,primary}}$. Now using the relations in equation (4.17), we have,

$$\epsilon N_{generated} = N_{rec}(1 - \tfrac{N_{cont}}{N_{rec}})$$
$$N_{generated} = N_{rec}\tfrac{(1-\delta)}{\epsilon}$$

$$N_{generated} = \frac{N_{rec}}{\omega} \tag{4.18}$$

where, the correction factor, $\omega = \epsilon/(1-\delta)$. Hence, the generated primary tracks can be obtained by dividing the number of reconstructed tracks with the correction factor. These correction factors are obtained for each p_T bin for each 10% centrality bin-widths.

The MC closure test, the total mean number of particles per event, $(K^+ + K^-)$, is estimated at the generated level and the reconstructed level from HIJING events. Using the correction factor, ω, obtained previously for different p_T bins and for different centrality bins, the local efficiency correction method is applied to the reconstructed values on an event-by-event basis and corrected number of particles are obtained. With these numbers, we can then calculate the central moments of our observables, i.e, $\sigma_{P(E)}$, $S_{P(E)}$, $\kappa_{P(E)}$, σ_{Pull}, S_{Pull}, and κ_{Pull}. For comparison, the generated, reconstructed and efficiency corrected values of $< K^+ + K^- >$, $\sigma_{P(E)}$, $S_{P(E)}$, $\kappa_{P(E)}$, σ_{Pull}, S_{Pull}, and κ_{Pull} are shown as a function of centrality in Fig. 4.7, Fig. 4.8, and Fig. 4.9. For closure test, the ratios of the values at the generated to the efficiency corrected level are shown on the lower panel of each figures. Closure is achieved if the ratio is consistent with unity within uncertainties.

Fig. 4.7 depicts the closure test for the total number of particles. The error bars shown are statistical only. The ratios of the generated value to the efficiency corrected value is consistent with 1. That means that our correction factor is working properly for the number of particles. Lets take the case of first central bin $(0-10)\%$. The reconstructed number of particles, shown by the green points, is around 425. The generated number of particles, shown by square points, is around 175. Our reconstructed number is greater than the generated one because of the mis-identification of Kaons with pions and electrons during particle identification. Hence, while correcting, we do the background subtraction on reconstructed number and produce the efficiency corrected value, which in our case, shown by the red points, is the same as the generated one. This completes the closure test.

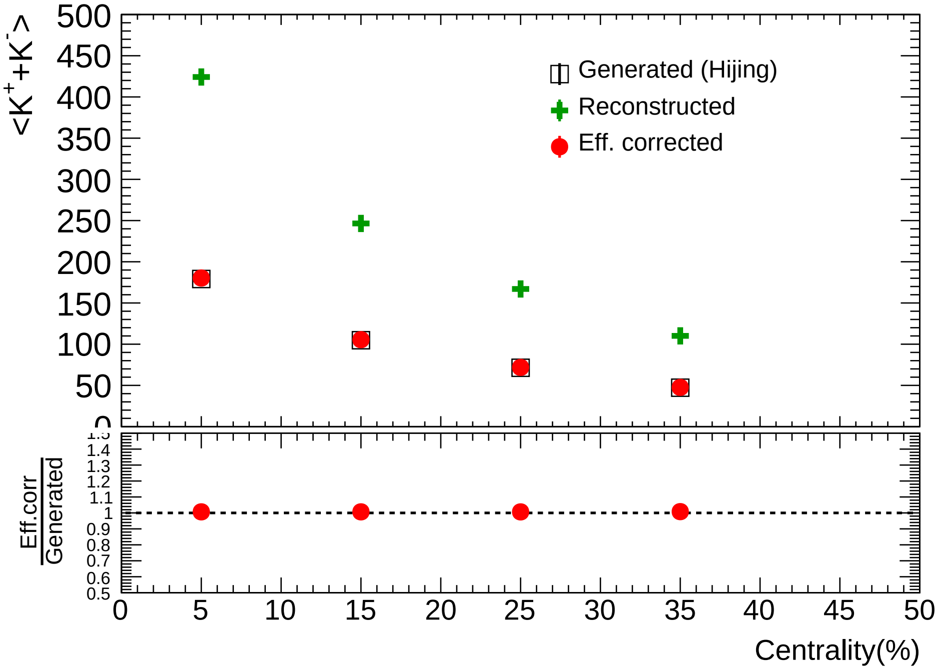

Figure 4.7: $< K^{+}+K^{-} >$ measured at generated level, reconstructed level and after efficiency correction, shown as a function of centrality for Pb-Pb 5.02 TeV MC events.

Fig. 4.8 shows the closure test for the central moments of the distribution of probability of event clustering. The main difference with the closure test done for the total number of particles, shown in Fig. 4.7, is that the correction factor is not applied directly on the observables. We apply the correction factor only to the total number of particles and get the corrected number of particles. Once we produce the corrected number of particles, we then calculate the central moment of the observables. Hence, the observables for the generated HIJING are calculated from the generated number of particles, observables for the reconstructed HIJING are calculated from the reconstructed number of particles and similarly the corrected observable is calculated from the corrected number of particles. The statistical uncertainties are shown on the plots. Statistical uncertainties are highly dependent on the number of particles per azimuthal bin and the total number of events (see section 4.4). A higher number of particles in a large event sample results in low statistical uncertainty.

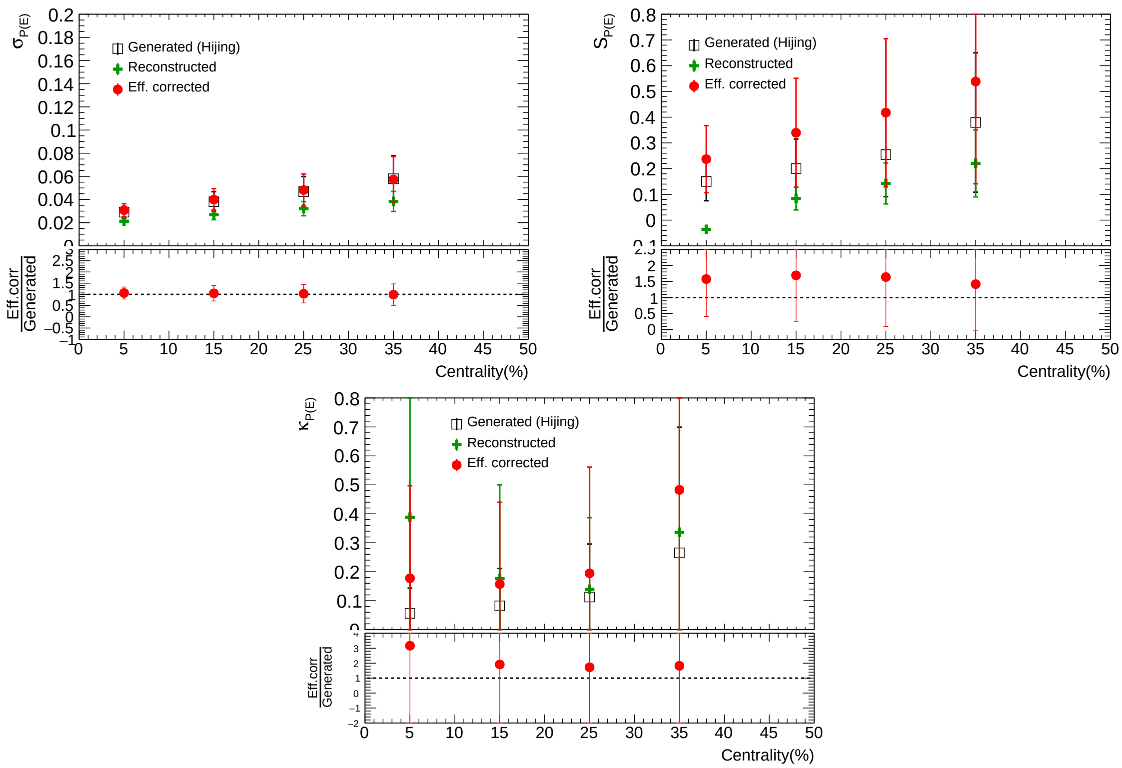

Figure 4.8: $\sigma_{P(E)}$ (left), $S_{P(E)}$ (right), and $\kappa_{P(E)}$ (center) measured at generated level, reconstructed level and after efficiency correction, shown as a function of centrality for Pb-Pb 5.02 TeV MC events.

We do observe that our corrected point closes with the generated one within the error bars for all clustering parameters.

Fig. 4.9 shows the closure test for the Pull distributions. The method of calculating the central moments for this observable is similar to that of the distribution of probability of event clustering. The uncertainties shown on the plots are statistical only. In this case, we again observe that the values for the σ_{Pull}, S_{Pull}, and κ_{Pull} closes within the uncertainties.

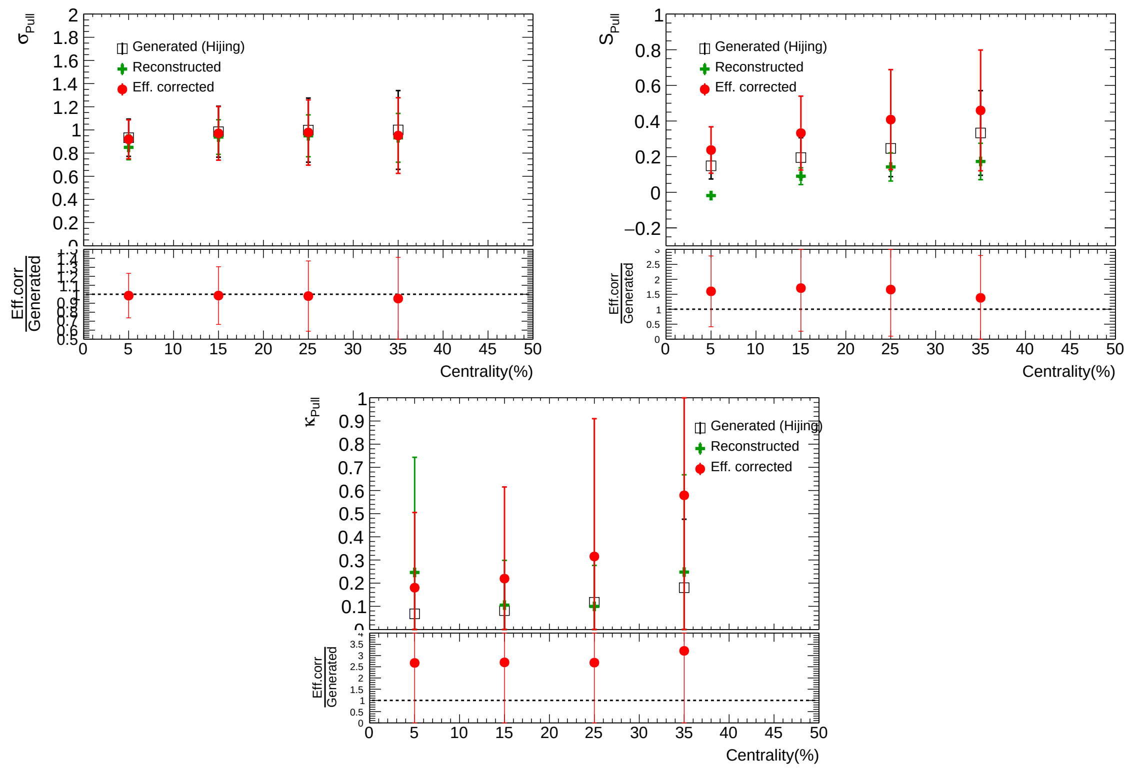

Figure 4.9: σ_{Pull} (left), S_{Pull} (right), and κ_{Pull} (center) measured at generated level, reconstructed level and after efficiency correction, shown as a function of centrality for Pb-Pb 5.02 TeV MC events.

Chapter 5

Results and discussions

The motivation to investigate the central moments of probability of event clustering and Pull distributions is to search for clusters of strange quarks in azimuthal space. For this purpose, taking Kaons ($K^+ + K^-$) as a proxy for the strange quarks, we first divide the azimuthal phase space into six different bins. For each azimuthal bin, we did the particle identification (PID) event by event. After the PID, we will have the information about the number of particles produced per event in a particular centrality and particular azimuthal bin. A simulation study is done in order to check the sensitivity of the observables and also to correct for the detector efficiency and particle contamination. After correcting for the number of particles, we calculated the central moments of our observable. In this chapter, we present the final results and compared them with the sensitivity plots we generated from simulation. Generally speaking a deviation form the Gaussian baseline distribution should scale with the moment of the distribution, i.e, small clustering effects would be only visible in the higher moments whereas large cluster formation could already be noticeable in the variance of the distribution. On the other hand, the statistical uncertainty grows with the power of the moment, and therefore reliable measurements of kurtosis are exceedingly difficult and require very large datasets.

5.1 Second Central Moment of Probability of Event Clustering ($\sigma_{P(E)}$)

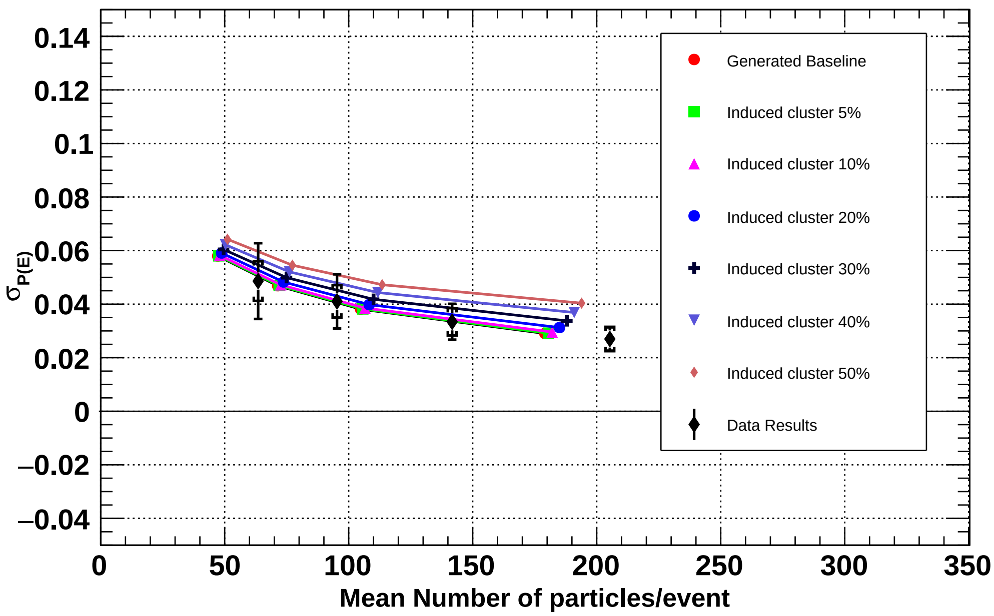

Figure 5.1: Final results for, variance of $P(E)$, $\sigma_{P(E)}$, at Pb-Pb 5.02 TeV. The most central point corresponds to the point on the right (close to 200 on the horizontal axis).

Fig. 5.1 shows the plot of $\sigma_{P(E)}$ with respect to the mean number of particles generated per event. The second central moment is generally related to the width of the distribution. If there exists a clustering phenomenon, then that could result in the increase in width of the distribution. This kind of deviation then needs to be compared with the sensitivity plots from Chapter 3. In Fig. 5.1, the most central event corresponds to the rightmost point and peripheral events correspond to the leftmost points. The statistical error is shown by the dark lines. The systematic uncertainty is shown by the bracket. This labelling is followed in all the subsequent plots. When we compare our data corrected values with the sensitivity plots, the corrected data points are in agreement with the generated baseline given by HIJING.

The result does not show any signs of clustering.

5.2 Third Central Moment of Probability of Event Clustering ($S_{P(E)}$)

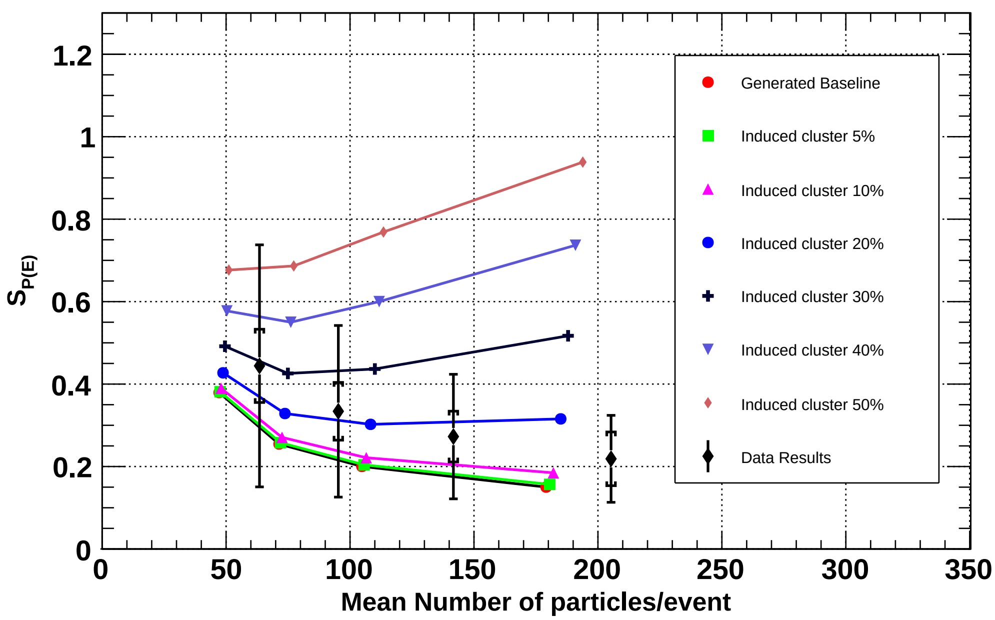

Figure 5.2: Final results for skewness, $S_{P(E)}$, at Pb-Pb 5.02 TeV. The most central point corresponds to the point on the right (close to 200 on the horizontal axis).

The third moment of probability of event clustering, also know as skewness, is more sensitive than the second moment. Skewness generally represents the asymmetry in the distributions. If we consider the distribution of probability of event clustering, the percentage of cluster should increase the skewness or, in other words, clustering should make the distribution more asymmetric. Fig. 5.2 shows the corrected data results with respect to mean number of particles per event. When we compare our corrected data results with our sensitivity plots, corrected data values lie within the sensitivity plots. We do not see any deviation from the generated baseline. Based on anticipated sensitivity and our measured uncertainty, we can exclude a clustering probability of more than 20% in central Pb-Pb events.

5.3 Fourth Central Moment of Probability of Event Clustering ($\kappa_{P(E)}$)

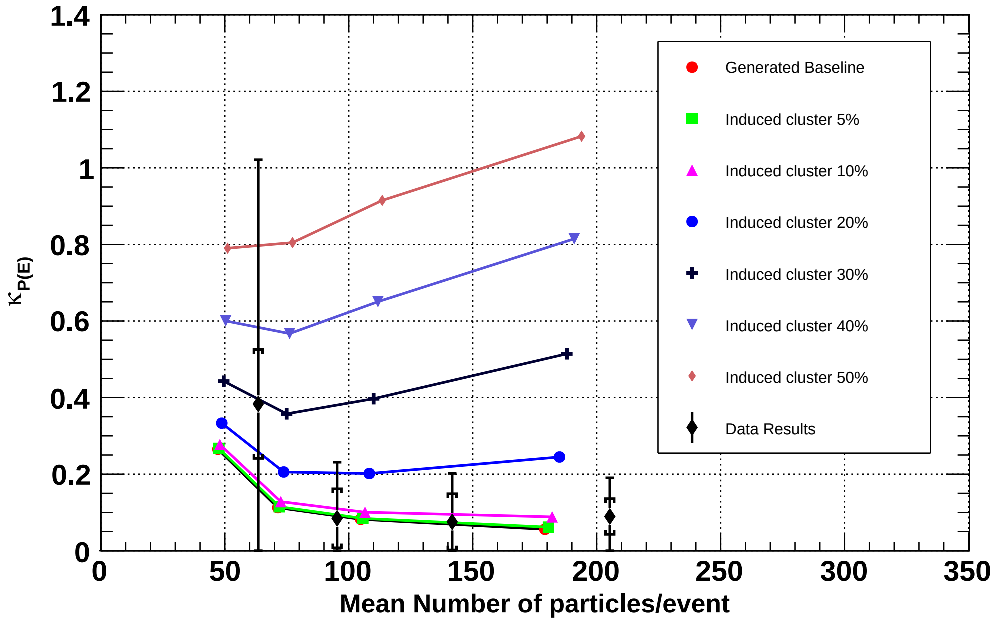

Figure 5.3: Final results for kurtosis, $\kappa_{P(E)}$, at Pb-Pb 5.02 TeV. The most central point corresponds to the point on the right (close to 200 on the horizontal axis).

The fourth moment, i.e, kurtosis, represents the peakedness and the tailedness of the distribution. This moment is more sensitive than Skewness. However, the data corrected results lie along the points given by the generated baselines. The result is consistent with the clustering estimate obtained from the skewness measurement in Fig. 5.2.

In summary, the central moment values for the distribution of probability of event clustering, when being compared with the sensitivity plots, show no sign of clustering in any of the four centrality bins above the 20% level.

5.4 Second Central Moment of Probability of Event Clustering (σ_{Pull})

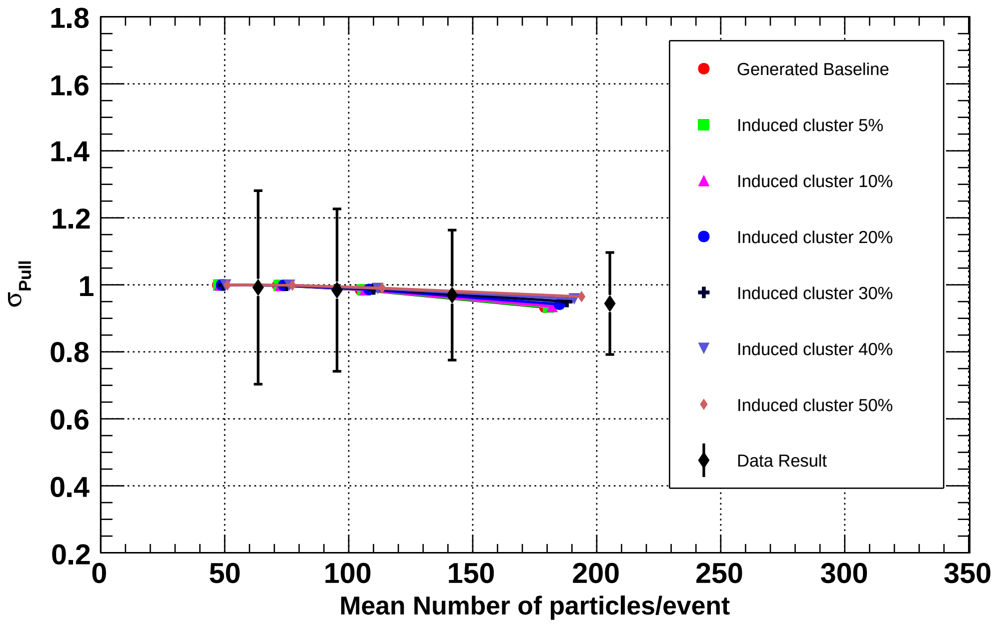

Figure 5.4: Final results for second moment, σ_{Pull}, at Pb-Pb 5.02 TeV. The most central point corresponds to the point on the right (close to 200 on the horizontal axis).

The idea behind considering Pull distributions for calculating the clustering phenomenon is that we normalize the distribution by the mixed event baseline and therefore potentially achieve a higher sensitivity, since the baseline is now data-driven. When the Difference distribution is divided by the standard deviation of the mixed event, we get the Pull distribution. In Fig. 5.4, we plot the second moment of Pull distribution with respect to mean number of particles generated per event. We see that the corrected data values match the trendline given by the generated baseline, confirming no clustering. We also note that the second moment of pull distribution show zero sensitivity to the level of clustering.

5.5 Third Central Moment of Probability of Event Clustering (S_{Pull})

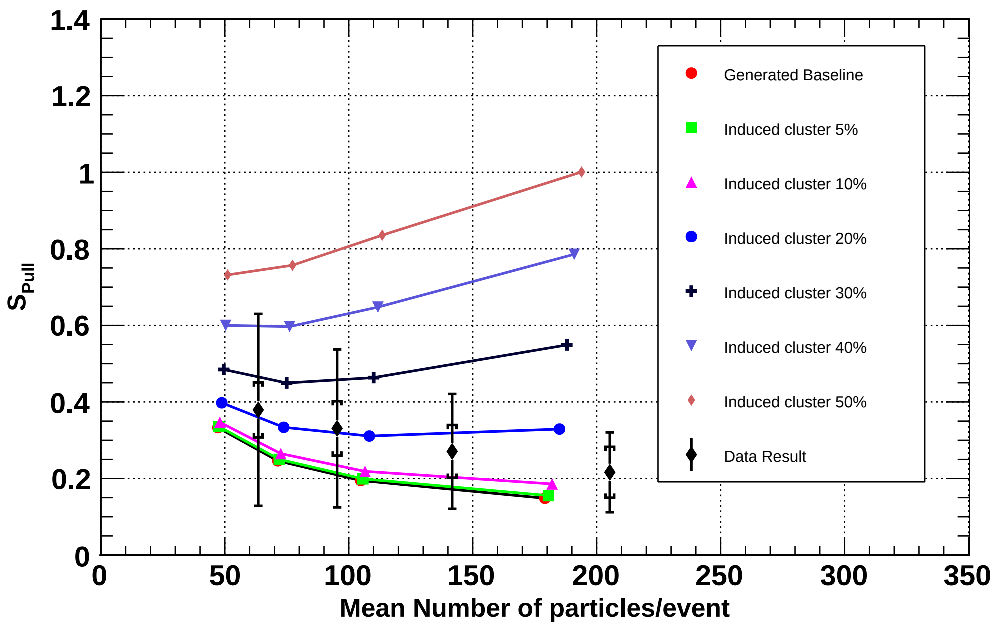

Figure 5.5: Final results for skewness, S_{Pull}, at Pb-Pb 5.02 TeV. The most central point corresponds to the point on the right (close to 200 on the horizontal axis).

The skewness of the Pull distributions is shown in Fig. 5.5. Owing to the large error bars, the corrected data values are on top of the generated baseline, given by MC HIJING. The less than 20% clustering probability level is also confirmed through the measurement.

5.6 Fourth Central Moment of Probability of Event Clustering (κ_{Pull})

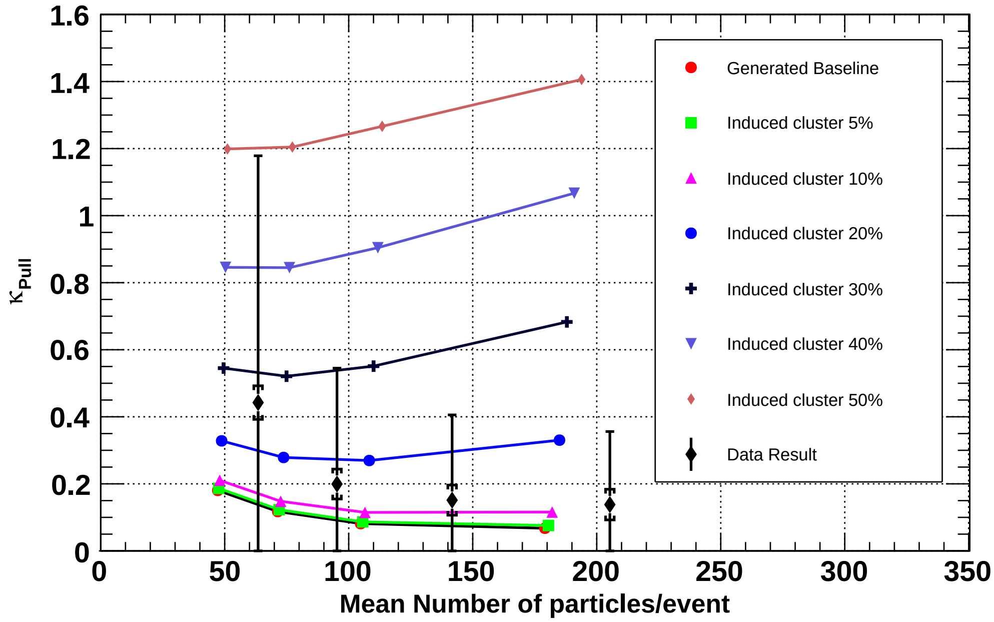

Figure 5.6: Final results for kurtosis, κ_{Pull}, at Pb-Pb 5.02 TeV. The most central point corresponds to the point on the right (close to 200 on the horizontal axis).

Finally, the kurtosis of the Pull distributions is shown in Fig. 5.6. It also falls along the baseline given by the generated HIJING events. Overall the Pull distributions do not show additional sensitivity to clustering when compared to the initial probability distributions. This indicates that the Gaussian assumptions of azimuthal distribution is well justified and confirmed by mixed event data.

Chapter 6

Conclusions

Any discovery experiment in the environment created by relativistic heavy ion collisions requires a dedicated discussion of the anticipated and achievable results. Most of these measurements end up with a null result, which nevertheless carries significance based on setting a production threshold for the effect in question. In our case, we tried to investigate whether flavor hierarchy in the QCD transition crossover region could lead to clustering of strangeness and thus preferred strange particle emission. The hadronization of particles is then motivated not by energy conversion to the lowest mass mesons, but by the desire to form states with preferred flavor. Putting these two conditions together will ultimately lead to over-production of Kaons in a certain region of phase space, as soon as the pure strange state is prohibitively heavy or the state is formed and then decays into a number of the lowest mass strange mesons, i.e., the Kaons. So either direct strange quark clustering or subsequent strange meson clustering could be captured by this analysis. Clustering is defined gemoetrically in this context, i.e., no requirements on the dynamics of the particles are required. This effect can be viewed as similar to jet production in hard elementary collisions, except here we expect the emitted jet of particles to be high momentum, whereas in the case of bulk clustering the particles will exhibit a typical momentum distribution, but a very focussed spatial distribution. Generally heavy ion collisions have a distinct distribution in polar angle, i.e., pseudorapidity, which is very energy dependent. In the azimuthal direction, though, the distribution is flat over the full 2π coverage. Thus our signatures were based on variations or fluctuations in azimuthal direction. One should note that the underlying physics does not necessarily lead to clustering in every event. A centrality dependence is certainly expected, i.e., the probability of clustering should go up in more violent collisions. On the other hand the multiplicity of produced particles as a whole will go up too, and thus the central limit theorem has to be taken into account when interpreting the data. In addition, not every central collision will cluster with the same strength. Therefore this analysis is based on statistically averaged parameter distributions.

The baseline, i.e., expectation of no clustering, can be achieved either through simple statistical considerations of Poissonian particle production, leading to Gaussian distributed signatures, or through analysis of realistic MC event generators, such as HIJING, that do not carry any mechanism to generate particle clusters or even flavor hierarchy in the particle freeze-out. In this dissertation we have employed both methods to normalize our results.

The signature parameters were deduced based on typical clustering analyses that used geometrical multiplictiy distributions rather than distributions in momentum space. The two parameters, introduced in Chapter 3, namely the probability of event clustering and the Pull distribution, were both analyzed in order to determine whether for this specific application one of them would exhibit a higher sensitivity level. The expectation was that the Pull distribution, which is normalized to a data based mixed event sample, might be more precise.

The sensitivity levels calculated based on a detailed MC simulation shown in Section 3.6 of Chapter 3, reveal that the lowest moments of the clustering parameter distributions, i.e., the variance, show very little promise to detect even a significant amount of clustering.

The higher moments, skewness and kurtosis, though, seemed promising. This has to be balanced with a significant increase in required statistics to achieve errors of the same order of magnitude for the higher moments.

The analysis was significantly impacted by the rather high contamination level that one experiences when reconstructing Kaons, using energy loss in the main tracking detector, the TPC. The problem is that both pions and protons are produced with higher or comparable yields to the kaons, and cross the Bethe-Bloch curve of the kaons in momentum ranges where the kaon yields peak. Therefore, contamination levels up to 90% had to be subtracted, and although the background yield is well determined, the systematic uncertainty on the subtracted signal yield is considerable and dominates, together with the low event-by-event statistics of reconstructed kaons in the chosen azimuthal binning, the error of the clustering parameters. In order to improve the event-by-event statistics in our analysis, we use the sum of charged Kaons as our initial observable for the number of particles produced per event. This is different from most moment analyses which use the difference, i.e., net-kaons as their basis. Overall the statistical uncertainty in this analysis is a complex convolution of the number of collisions recorded (event statistics) and the number of kaons reconstructed in any given event (particle statistics). The details are broken down in Chapter 4.

The results we obtained were surprising in several aspects. First, the probability and pull distributions showed almost the same sensitivity level to the signal. Second the centrality dependence was less pronounced than expected. Overall the analysis suffered from large uncertainties due to the high particle contamination level and the small event by event statistics of reconstructed charged kaons, even at the highest collision energy. Nevertheless, although no evidence for clustering was found, the threshold level of less than 20% clustering, which was consistent over all skewness and kurtosis measurements, significantly limits the idea of preferential emission of strange particles at these energies in central heavy ion collisions.

There is definitely room for improvement in this analysis as soon as larger datasets from LHC Run-2 and 3, using an upgraded TPC, become available. The reconstruction efficiency for Kaons can be improved with tighter dE/dx cuts in a better resolution TPC, which will also reduce the contamination level considerably. Improvements in the Kalman filter based reconstruction approach are anticipated, based on machine learning algorithms. And finally the event statistics, i.e., the number of recorded collisions, is expected to improve by an order of magnitude in the next three years. With these advances we can expect to find either a positive signal or a threshold that definitively excludes strangeness clustering during the QCD crossover.

Bibliography

[1] F. Zwicky. On the Masses of Nebulae and of Clusters of Nebulae. *The Astrophysical Journal*, 86:217, 1937.

[2] C. J. Gaudet. *A General Approach to the Direct Detection of Dark Matter.* University of Louisiana at Lafayette, 7–12, 2013.

[3] E. J. Lofgren. Experiences with the Bevatron. Technical report, Ernest Orlando Lawrence Berkeley National Laboratory, Berkeley, CA (US), 1956.

[4] J. L. Nagle, I. G. Bearden, and W. A. Zajc. Quark-Gluon Plasma at the RHIC and the LHC: Perfect Fluid Too Perfect? *New Journal of Physics*, 13(7):075004, 2011.

[5] D. Griffiths. *Introduction to Elementary Particles.* John Wiley & Sons, 49–52, 2020.

[6] S. Bethke. Experimental Tests of Asymptotic Freedom. *Progress in Particle and Nuclear Physics*, 58(2):351–386, 2007.

[7] K. G. Wilson. Confinement of Quarks. *Physical Review D*, 10(8):2445, 1974.

[8] A. Chodos, R. Jaffe, K. Johnson, C. B. Thorn, and V. F. Weisskopf. New Extended Model of Hadrons. *Physical Review D*, 9(12):3471, 1974.

[9] C. E. DeTar and J. F. Donoghue. Bag Models of Hadrons. *Annual Review of Nuclear and Particle Science*, 33(1):235–264, 1983.

[10] D. J. Gross and F. Wilczek. Asymptotically Free Gauge Theories. I. *Physical Review D*, 8(10):3633, 1973.

[11] D. J. Gross and F. Wilczek. Asymptotically Free Gauge Theories. II. *Physical Review D*, 9(4):980, 1974.

[12] H. D. Politzer. Reliable Perturbative Results for Strong Interactions? *Physical Review Letters*, 30(26):1346, 1973.

[13] T. D. Lee and G. C. Wick. Vacuum Stability and Vacuum Excitation in a Spin-0 Field Theory. *Physical Review D*, 9(8):2291, 1974.

[14] G. Baym. RHIC: From Dreams to Beams in Two Decades. *arXiv preprint hep-ph/0104138*, 2001.

[15] F. Karsch and K. Redlich. Has Tc Been Measured by Heavy-ion Experiments? *Physical Review D*, 84(5):051504, 2011.

[16] F. Karsch. Lattice Results on QCD Thermodynamics. *arXiv preprint hep-ph/0103314*, 2001.

[17] B. Mohanty. Exploring the Quantum Chromodynamics Landscape with High-energy Nuclear Collisions. *New Journal of Physics*, 13(6):065031, 2011.

[18] F. R. Brown, F. P. Butler, H. Chen, N. H. Christ, Z. Dong, W. Schaffer, L. I. Unger, and A. Vaccarino. On the Existence of a Phase Transition for QCD with Three Light Quarks. *Physical Review Letters*, 65(20):2491, 1990.

[19] Y. Hatta and T. Ikeda. Universality, the QCD Critical and Tricritical Point, and the Quark Number Susceptibility. *Physical Review D*, 67(1):014028, 2003.

[20] R. S. Bhalerao. Relativistic Heavy-ion Collisions. *arXiv preprint arXiv:1404.3294*, 2014.

[21] P. Kalinak. Strangeness Production in Pb-Pb Collisions with ALICE at the LHC. *PoS*, page 168, 2018.

[22] M. C. Abreu, B. Alessandro, C. Alexa, R. Arnaldi, J. Astruc, M. Atayan, C. Baglin, A. Baldit, M. Bedjidian, F. Bellaiche, et al. Observation of a Threshold Effect in the Anomalous J/ψ Suppression. *Physics Letters B*, 450(4):456–466, 1999.

[23] K. Adcox, S. S. Adler, N. N. Ajitanand, Y. Akiba, J. Alexander, L. Aphecetche, Y. Arai, S. H. Aronson, R. Averbeck, T. C. Awes, et al. Suppression of Hadrons with Large Transverse Momentum in Central Au+ Au Collisions at $\sqrt{S_{NN}} = 130$ GeV. *Physical Review Letters*, 88(2):022301, 2001.

[24] K. Ackermann, N. Adams, C. Adler, Z. Ahammed, S. Ahmad, C. Allgower, J. Amsbaugh, M. Anderson, E. Anderssen, H. Arnesen, et al. Elliptic Flow in Au+ Au Collisions at $\sqrt{S_{NN}} = 130$ GeV. *Physical Review Letters*, 86(3):402, 2001.

[25] B. Betz. Jet Propagation and Mach-cone Formation in (3 + 1) - Dimensional Ideal Hydrodynamics. *arXiv preprint arXiv:0910.4114*, 2009.

[26] E. Iancu. QCD in Heavy-ion Collisions. *arXiv preprint arXiv:1205.0579*, 2012.

[27] J. Bartke. *Introduction to Relativistic Heavy-ion Physics*. World Scientific, 2008.

[28] P. B. Munzinger, J. Stachel, J. P. Wessels, and N. Xu. Thermal Equilibration and Expansion in Nucleus-Nucleus Collisions at the AGS. *Physics Letters B*, 344(1-4):43–48, 1995.

[29] P. B. Munzinger, J. Stachel, and C. Wetterich. Chemical Freeze-out and the QCD Phase Transition Temperature. *Physics Letters B*, 596(1-2):61–69, 2004.

[30] A. Andronic. An Overview of the Experimental Study of Quark-Gluon Matter in High-energy Nucleus-Nucleus Collisions. *International Journal of Modern Physics A*, 29(22):1430047, 2014.

[31] B. I. Abelev, M. M. Aggarwal, Z. Ahammed, A. V. Alakhverdyants, B. D. Anderson, D. Arkhipkin, G. S. Averichev, J. Balewski, O. Barannikova, L. S. Barnby, et al. Identified Particle Production, Azimuthal Anisotropy, and Interferometry Measurements in Au + Au Collisions at $\sqrt{S_{NN}} = 9.2$ GeV. *Physical Review C*, 81(2):024911, 2010.

[32] J. Cleymans, H. Oeschler, and K. Redlich. Influence of Impact Parameter on Thermal Description of Relativistic Heavy-ion Collisions at (1–2)A GeV. *Physical Review C*, 59(3):1663, 1999.

[33] M. M. Aggarwal, Z. Ahammed, A. V. Alakhverdyants, I. Alekseev, J. Alford, B. D. Anderson, C. D. Anson, D. Arkhipkin, G. S. Averichev, J. Balewski, et al. Scaling Properties at Freeze-out in Relativistic Heavy-ion Collisions. *Physical Review C*, 83(3):034910, 2011.

[34] F. Karsch. Determination of Freeze-out Conditions from Lattice QCD Calculations. *Central European Journal of Physics*, 10(6):1234–1237, 2012.

[35] S. Borsanyi, Z. Fodor, S. D. Katz, S. Krieg, C. Ratti, and K. Szabó. Fluctuations of Conserved Charges at Finite Temperature from Lattice QCD. *Journal of High Energy Physics*, 2012(1):1–15, 2012.

[36] R. Bellwied, S. Borsányi, Z. Fodor, S. D. Katz, A. Pasztor, C. Ratti, and K. K. Szabo. Fluctuations and Correlations in High Temperature QCD. *Physical Review D*, 92(11):114505, 2015.

[37] F. A. Flor, G. Olinger, and R. Bellwied. Flavour and Energy Dependence of Chemical Freeze-out Temperatures in Relativistic Heavy-ion Collisions from RHIC-BES to LHC Energies. *Physics Letters B*, page 136098, 2021.

[38] J. Rafelski and B. Müller. Erratum: Strangeness Production in the Quark-Gluon Plasma [phys. rev. lett. 48, 1066 (1982)]. *Physical Review Letters*, 56(21):2334, 1986.

[39] P. Koch, B. Müller, and J. Rafelski. Strangeness in Relativistic Heavy-ion Collisions. *Physics Reports*, 142(4):167–262, 1986.

[40] B. Abelev, J. Adam, D. Adamová, A. M. Adare, M. M. Aggarwal, G. A. Rinella, M. Agnello, A. G. Agocs, A. Agostinelli, Z. Ahammed, et al. Multi-strange Baryon Production at Mid-rapidity in Pb-Pb Collisions at $\sqrt{S_{NN}} = 2.76$ TeV. *Physics Letters B*, 728:216–227, 2014.

[41] S. Hamieh, K. Redlich, and A. Tounsi. Canonical Description of Strangeness Enhancement from p-A to Pb-Pb Collisions. *Physics Letters B*, 486(1-2):61–66, 2000.

[42] A. G. Knospe. Sissa: New Results on Soft Particle Production in Heavy-ion Collisions with ALICE. *PoS*, page 217, 2018.

[43] ALICE Collaboration et al. Enhanced Production of Multi-strange Hadrons in High-multiplicity Proton-Proton Collisions. *Nature Physics*, 13(6):535–539, 2017.

[44] N. K. Glendenning and J. S. Bielich. Neutron Star Constraints on the H dibaryon. *Physical Review C*, 58(2):1298, 1998.

[45] L. Evans and P. Bryant. LHC machine. *Journal of Instrumentation*, 3(08):S08001, 2008.

[46] L. Betev and P. Chochula. Definition of the ALICE Coordinate System and Basic Rules for Sub-detector Components Numbering. *ALICE Internal Note (ALICE-INT-2003-038)*, 2003.

[47] Performance of the ALICE Experiment at the CERN LHC. *International Journal of Modern Physics A*, 29(24):1430044, Sep 2014.

[48] P. Crochet. The ALICE Forward Muon Spectrometer. *Pramana-J. Phys.*, 60(CERN-ALI-2001-058):1051–1054, 2001.

[49] Collaboration ALICE. ALICE: Technical Design Report of Inner Tracking System (ITS). CERN Report, Vol. Technical report, CERN/LHCC/99–012, 1999.

[50] J. Alme, Y. Andres, H. Appelshäuser, S. Bablok, N. Bialas, R. Bolgen, U. Bonnes, R. Bramm, P. B. Munzinger, R. Campagnolo, et al. The ALICE TPC, a Large 3-Dimensional Tracking Device with Fast Readout for Ultra-high Multiplicity Events. *Nuclear Instruments and Methods in Physics Research Section A: Accelerators, Spectrometers, Detectors and Associated Equipment*, 622(1):316–367, 2010.

[51] W. Blum, W. Riegler, and L. Rolandi. *Particle Detection with Drift Chambers*. Springer Science & Business Media, 29–407, 2008.

[52] Y. Belikov, K. Safarík, and B. Batyunya. Kalman Filtering Application for Track Recognition and Reconstruction in ALICE Tracking System. Technical report, 1–12,1997.

[53] A. Kalweit. Production of Light Flavor Hadrons and Anti-nuclei at the LHC. 2012.

[54] ALICE Collaboration, G. Renault, B. S. Nielsen, J. Westergaard, and J. J. Gaardhje. The Laser of the ALICE Time Projection Chamber. *International Journal of Modern Physics E*, 16(07n08):2413–2418, 2007.

[55] E. Abbas. Performance of the ALICE VZERO System. *Journal of Instrumentation*, 8, 2013.

[56] A. Toia. Participants and Spectators at the Heavy-ion Fireball. *CERN Courier*, page 4, 2013.

[57] ALICE Collaboration. Centrality Determination in Heavy-ion Collisions.

[58] X. Luo, B. Mohanty, H. G. Ritter, and N. Xu. Energy Dependence of High Moments for Net-Proton Distributions. *Journal of Physics G: Nuclear and Particle Physics*, 37(9):094061, 2010.

[59] H. Heiselberg. Event-by-event Physics in Relativistic Heavy-ion Collisions. *Physics Reports*, 351(3):161–194, Sep 2001.

[60] R. J. Tibshirani and B. Efron. An Introduction to the Bootstrap. *Monographs on Statistics and Applied Probability*, 57:1–436, 1993.

[61] X. Luo. Error Estimation for Moment Analysis in Heavy-ion Collision Experiment. *Journal of Physics G: Nuclear and Particle Physics*, 39(2):025008, 2012.

[62] M. Gyulassy and X. Wang. Hijing 1.0: a Monte Carlo Program for Parton and Particle Production in High Energy Hadronic and Nuclear Collisions. *Computer Physics Communications*, 83(2–3):307–331, 1994.